1980

Transport Properties of Antimony in a Rod and Corbino Geometries at Low Temperatures.

Mahmood Baratikhajooie
Louisiana State University and Agricultural & Mechanical College

BARATIKHAJOOIE, MAHMOOD

TRANSPORT PROPERTIES OF ANTIMONY IN A ROD AND CORBINO GEOMETRIES AT LOW TEMPERATURES

The Louisiana State University and Agricultural and Mechanical Col. PH.D. 1980

TRANSPORT PROPERTIES OF ANTIMONY IN A ROD AND CORBINO GEOMETRIES AT LOW TEMPERATURES

A Dissertation

Submitted to the Graduate Faculty of the
Louisiana State University and
Agricultural and Mechanical College
in partial fulfillment of the
requirements for the degree of
Doctor of Philosophy

in

The Department of Physics and Astronomy

by
Mahmood Baratikhajooie
M.S., Shiraz University, Iran, 1969
May 1980

ACKNOWLEDGEMENTS

The author wishes to express his deep gratitude to Professor Claude G. Grenier for his constant guidance and assistance throughout the course of the present work. The author is especially indebted to Dr. David L. Waldorf for his assistance and advice in the laboratory, and to Dr. Ching L. Tsai for many helpful suggestions.

The author also gratefully acknowledges the contributions from members of the dissertation committee and members of the low temperature group. Thanks are also due to Ms. Jackie Tamas who typed this manuscript. In addition, the financial assistance received from the Dr. Charles E. Coates Memorial Fund of the L.S.U. Foundation donated by George H. Coates for preparation of this manuscript is gratefully acknowledged.

TABLE OF CONTENTS

Page

LIST OF TABLES

Table — Page

LIST OF FIGURES

LIST OF FIGURES (continued)

CAPTIONS OF FIGURES

Figure

1. The ratio of TEP, $\varepsilon(0)$, to T versus T^2. The measured values of this study are shown by (0). ε_{c1}/T (the carrier diffusive term), ε_{g1}/T (the simple drag term) and $(\varepsilon_{c2}+\varepsilon_{g2})/T$ (the mutual drag term) are shown by dash lines.

2. The apparent density of electronic states at Fermi surface of antimony, Z_{eff}, versus T^2. The data shown by (+ Δ □ o) are determined from $\langle\varepsilon''_{21}\rangle = \langle\sigma_{11}\rangle \lambda_g \langle\varepsilon'_{21}\rangle$. The points shown by (□) and (Δ) are taken from Long, et al., and Blewer, respectively, (+) and (o) are the experimental results on Tsai's samples A and C. The data shown by (x) is the $(\langle\rho_{11}\rangle/\rho_{11b})Z_{eff}(\varepsilon')$ on sample C. The points shown by (⊙) and (•) are determined from $\langle\pi''_{21}\rangle = \langle\sigma_{11}\rangle \lambda_g \langle\pi'_{21}\rangle$ on sample C and D.

3. A schematic diagram of the rod sample with the heater arrangements.

4. A schematic diagram of the disk sample with the heater arrangements.

5&6. The measured magnetoresistance of the disk sample No. 3 as a function of temperature at H = 8 KG and H = 20 KG. The data shown by (o) are the magnetoresistance of the sample where the vacuum chamber was filled with liquid helium, and the data shown by (Δ) are the measured magnetoresistance of the sample in vacuum.

7. The measured magnetoresistivity of the disk sample No. 1 with a thickness of about 8 mm with different surface treatment as a function of temperature at H = 20 KG. The data shown by o , □ , x and Δ are the magnetoresistivity of the sample where the surfaces were lapped, cleaved, chemically etched, and electropolished, respectively.

8. The measured magnetoresistivity of the disk sample No. 1 with different surface treatment as a function of magnetic field at T = 4.2°K. The data shown by o , □ , x and Δ are the magnetoresistivity of the sample where the surfaces were lapped, cleaved, chemically etched and electropolished, respectively.

CAPTIONS OF FIGURES (continued)

Figure

9. The apparent conductivities ($1/\rho_{11}$) of the different electropolished disk samples versus the reciprocal of their thickness (1/t) at T = 1.1°K and H = 20 KG. The large uncertainty in the geometric factor measurement would yield to such a large (15%) error (shown by error bar) in the magnetoconductivity determination. The dash lines represent the size effect in a rod geometry (Tsai I, Fig. 4).

10. "Isothermal" magnetoresistance (sample in contact with a liquid helium bath) of the disk sample No. 2 with a radial slot in the sample, as a function of temperature at H = 20 KG where the broken circular symmetry in the sample causes a jump at λ point.

11. The magnetoresistance of the disk sample No. 2 with a radial slot in the sample as a function of magnetic field at T = 4.22°K. The data shown by (●) and (o) were obtained by using two pairs of potential probes at both sides of the sample.

12. The measured magnetoresistance of Tsai's rod sample as a function of temperature at H = 20 KG. The sample was cut such that the surfaces make an angle of about 7° with the basal plane to reduce any possible peeling effect.

13. Magnetoresistivity of Tsai's rod sample No. 5 versus magnetic field at T = 1.8 and T = 4.22°K. The sample was cut such that the surfaces make an angle of about 7° with the basal plane to reduce any possible peeling effect.

14. "Isothermal" and "adiabatic" magnetoresistivities of the rod sample (D) as a function of temperature at H = 20 KG. The data shown by (o) are the magnetoresistivities of the sample in vacuum and (Δ) the magnetoresistivities measured when the vacuum chamber was filled with helium gas at liquid nitrogen temperature with 1.1 cm Hg. The sample was electropolished and a value of $\alpha = 1.92$ for the exponent was measured.

15. The measured Ettingshausen coefficient π'_{21} in the rod sample (D) as a function of temperature at H = 20 KG. The sample was electropolished and a value of 1.92 for the exponent, α, was measured.

CAPTIONS OF FIGURES (continued)

Figure

16. The measured Nernst-Ettingshausen coefficient ε'_{12} in the rod sample (D) versus temperature at H = 20 KG. The sample was electroplished and a value of 1.92 for the exponent, α, was measured.

17. Lattice thermal conductivity in the rod sample (D) versus temperature at H = 8 KG. The data shown by (O) are measured in this sample and (□) are taken from Long, et al. Because of the relatively large discrepancy between the two results, the experiment was repeated (Fig. 22).

18. "Adiabatic" and "isothermal" magnetoresistivities of the rod sample (D) as a function of temperature at H = 20 KG. The data shown by (O) are the measurements in vacuum and (Δ) are the measurements when the vacuum cahmber was filled with helium gas at nitrogen temperature with about 1.1 cm Hg. The sample was electropolished and a value of 1.96 was measured for the exponent, α, but the magnetoresistance decreased by about 50% from the last measurement. Detail has been given in the text.

19. The measured Nernst-Ettingshausen coefficient ε'_{21} in the rod sample (D) as a function of temperature at H = 20 KG. The sample was electropolished and a value of 1.96 measured for the exponent, α.

20. The measured Ettingshausen coefficient, π'_{21}, in the rod sample (D) as a function of temperature at H = 20 KG. The sample was electropolished and a value of 1.96 measured for the exponent, α.

21. Shadow effect in a disk geometry for two different current feedings. The first diagram shows this effect where the current lead is soldered to the center of the disk or to the boss which was cut by a spark cutter. The second diagram shows the effect where the current is fed by a copper wire which is soldered in a hole at the center of the disk. This effect yields to an error in the geometric factor, magnetoresistance, and thermal conductivity measurements.

22. Lattice thermal conduction Λ''_{11} over T^2 as a function of temperature in the disk sample No. 3 at H = 8 KG. The sample was electropolished and a value of α = 1.96 was obtained. The geometric factor was measured by a traveling microscope and also determined by matching this result with the result in the rod sample at

CAPTIONS OF FIGURES (continued)

Figure

$T = 1.1°K$. Values of 2.15 cm and 1.75 cm were obtained by the direct measurement and matching, respectively.

23. Lattice thermal conduction Λ_{11} over T^2 versus temperature in the rod sample (D) at H = 8 KG. The geometric factor measured by a traveling microscope is 0.109 cm. The data shown by (O), (Δ), and (□) were obtained by the potentiometric method, bridge method and plotting method, respectively. Detail for these methods are given in Appendix A.

24. λ_{11}/T^2 and λ''_{11}/T^2 as a function of temperature at H = 8 KG. The data shown by (o) are the lattice thermal conductivity over T^2 as measured in the rod sample (D) and the data shown by (Δ) are the result in the disk sample No. 3 where it has been matched with the thermal conductivity in the rod sample at $T = 1.1°K$. The calculated λ_{11}/T^2 (λ_{cal}/T^2), was obtained by using Eq. (61b) and the experimental data on the disk. λ_{cal}/T^2 is shown by dash lines in this graph.

25. The radial temperature change in the disk sample No. 3, due to the selfheating of the sample, as a function of I^2 at H = 20 KG. The data shown by (x) and (o) are the measured values at $T = 2.06°K$ and $T = 1.58°K$, respectively. The solid lines represent the theoretical results given by Eq. (93) at $T = 1.58°K$ and $2.06°K$.

A1. The temperature distribution in the sample when the main heater or the auxiliary heater is on. x_1 and x_2 are the positions of two resistance thermometers.

A2. A schematic diagram of Wheatstone bridge used to measure temperature difference as in thermal conduction and Ettingshausen measurements.

ABSTRACT

An investigation of the roles of carrier diffusion and carrier-phonon drag in the thermoelectric power, the Ettingshausen and Nernst-Ettingshausen effects was carried out on single crystals of antimony at low temperatures. Previous investigations have shown that the ideal resistivity and the high field resistivity are characterized by strong mutual drag. Here the Ettingshausen and Nernst-Ettingshausen effects were characterized by a strong simple drag. In contrast to these two extreme cases the thermoelectric power exhibited a clear admixture of the two drag conditions. Interpretation of Ettingshausen and Nernst-Ettingshausen data indicates that these two measurements are less reliable for the determination of the density of states than had been previously assumed because of the presence of surface conduction and size effects.

The transport properties of an antimony single crystal in a Corbino geometry at low temperature (1.1-4.2°K) and high magnetic field (4-20 KG) were studied. In this geometry the sample is in the form of a circular disk in which the current entered along the axis, flowed radially to the circumference where it left the sample. In this situation the circular symmetry does not permit the existence of either azimuthal temperature gradients or electric field. Therefore, the geometry could be used for the isothermal

magnetoconductivity and isopotential thermal magnetoconductivity measurements.

The effect of surface current on the magnetoresistance, ρ_{11}, in the Corbino geometry was investigated. This effect can be observed by studying the magnetic field and thickness dependence of the magnetoresistance of the sample. The experimental results did not reveal a quadratic field dependence of magnetoresistance, ρ_{11}, as predicted by Lifshitz, Azbel, Kaganou theory. In general $\rho_{11} \propto H^{\alpha}$, where α is always smaller than two and depends on the surface treatment of the sample. The largest values for α and ρ were obtained with the electropolished sample. These results are consistent with those obtained in a rod geometry.

The results of the thickness effect study in a Corbino geometry revealed that the effect was smaller than in a rod geometry, and apparently, for thickness greater than about 3 mm, the measured magnetoresistivity was almost independent of the thickness of the sample.

An experimental investigation of the lattice thermal conductivity in the rod and Corbino geometries indicates that the boundary scattering in the Corbino geometry is much smaller than in the rod geometry. This parameter is responsible for a large difference between the measured lattice thermal conductivity in these geometries.

Theoretical study of the phonon fan effect, which is a result of phonon drag in the Corbino geometry, showed that

the radial temperature gradient due to this effect is not only much smaller than that caused by the selfheating, but also it had the same current dependence (quadratic) as the selfheating.

INTRODUCTION

Antimony, like bismuth, is pentavalent with two atoms per unit cell and corresponds to five filled Brillouin zones. Because of overlapping of the bands which occur at the fifth zone boundary, transport properties and other related phenomena of this metal can be described in terms of the two-band model (holes and electrons).

Transport properties of antimony have been studied by de Haas-van Alphen effect, Shubnikov-de Haas effect, ultrasonic attenuation, cyclotron resonance, radio frequency size effect, magnetoreflection, microwave resonance, Raman scattering, infrared and galvanomagnetic as well as thermomagnetic effects at high and low temperature.

It was shown that the transport properties of antimony, like other semimetals, are highly affected by the condition of the surfaces as is some of the current carried by the surface damaged layer and surface diffusion layer. In contrast to a rod sample where both surface layers participate in that effect in the Corbino geometry, the recombination diffusion layer is eliminated and does not contribute to the transport property measurements.

Using the transport equations, one finds that the difference between isothermal and adiabatic magnetoresistance, which resulted from the existence of the transverse Ettingshausen temperature gradient in the adiabatic case, can be written as $\epsilon'_{21}\ \lambda_g\ \pi'_{21}$, where ϵ'_{21}, π'_{21} and λ_g are

Nernst-Ettingshausen, Ettingshausen, and lattice thermal conductivity, respectively. Adiabatic magnetoresistance could be measured in a rod sample by using the same system which is used for thermal measurement, i.e., sample in a vacuum. But when the sample is immersed in liquid helium(I) bath in order to measure the isothermal magnetoresistance, the poor heat conduction of the bath does not allow the isothermal condition to be achieved. It is also found that even in the temperature range where the liquid helium becomes superfluid existence of the Kapitza resistance between the sample and the bath prevents the complete achievement of the isothermal condition. Experimental work by C. L. Tsai, et al., on the magnetoresistance has shown this effect. In particular, the occurrence of a jump of the order of 2% in magnetoresistance has been observed at the λ point where the liquid helium becomes superfluid. In contrast to the rod geometry in the Corbino geometry, where circular symmetry does not allow the existence of azimuthal temperature gradients, neither a jump at λ point nor a difference in the magnetoresistance in any case (sample in vacuum or in liquid helium) is expected. This geometry yields a perfect condition for the isothermal measurement.

Similarly, one can show how the thermal conductivity measurement in the Corbino geometry would result in λ''_{11}, the isopotential thermal conductivity. The difference between λ''_{11} and λ_{11}, thermal conductivity measured in the rod sample,

can be used in order to calculate λ_{11} from the experimental result in the Corbino geometry. Using the theoretical formula for λ_{11} in antimony, we can derive the phonon boundary scattering relaxation frequency in the Corbino geometry.

CHAPTER I

STUDY OF TRANSPORT COEFFICIENTS OF ANTIMONY IN STRONG DRAG LIMIT

A - Introduction

Recent studies of the transport properties of antimony by Tsai, et al.,[1,2,3] (henceforth referred to as Tsai I, Tsai II and Tsai III, respectively) revealed the importance of both superficial currents and electron-phonon drag. In Tsai I, it was shown that the presence of superficial currents will strongly affect some properties (e.g., electrical magnetoresistivity) while yielding a negligible effect on others (e.g., thermal magnetoresistivity). Methods for dealing approximately with superficial conduction were also developed. Certain bulk properties were analyzed in Tsai II and Tsai III, wherein it was found on the one hand that electrical magnetoresistivity and zero field ideal resistivity are strongly affected by mutual drag, while on the other hand, carrier thermomagnetoresistivity and zero field ideal thermoresistivity are negligibly affected.

As a part of the continuing investigation of the transport properties of antimony, this chapter presents analyses of the influence of drag on the zero field thermoelectric effect and the high field Ettingshausen and Nernst-Ettingshausen effects. Further, the necessity for determining the influence of superficial conduction on the measurements of the Ettingshausen and Nernst-Ettingshausen effects will be demonstrated. The transport coefficients studied in this

paper, given in the notation of Jan,[4] are $\varepsilon''_{11}(0)$, $\varepsilon''_{12}(H)$, and $\pi''_{12}(H)$, respectively. The general transport equations are given by

$$\vec{J} = \hat{\sigma}\cdot\vec{E}^* + \hat{\varepsilon}''\cdot\vec{\nabla T} \qquad \vec{w}^* = -\hat{\pi}''\cdot\vec{E}^* - \hat{\lambda}''\cdot\vec{\nabla T} \tag{1}$$

or $$\vec{E}^* = \hat{\rho}\cdot\vec{J} - \varepsilon\cdot\vec{\nabla T} \qquad \vec{w}^* = -\hat{\pi}\cdot\vec{J} - \hat{\lambda}\cdot\vec{\nabla T} \tag{2}$$

or $$\vec{E}^* = \hat{\rho}^a\cdot\vec{J}^* + \hat{\varepsilon}'\cdot\vec{w}^* \qquad \vec{\nabla T} = -\hat{\pi}'\cdot\vec{J} - \hat{\gamma}\cdot\vec{w}^*. \tag{3}$$

The application of these equations to the case of antimony is described in detail in Tsai I, wherein the terms are defined; relationships between the coefficients are stated; simplifications arising from crystallographic symmetry and the disparate relative magnitudes of various elements of the transport tensors are described; and influence of superficial conduction upon the transport coefficients analyzed.

In all of the previous work (Tsai I, II, and III), the applied magnetic field is along the trigonal axis (the 3- or z-direction). In this way the isotropy of the basal plane in high magnetic field is maintained and thereby Umkehreffects are eliminated. For samples with rod geometry, $\vec{J}$ and $\vec{w}^*$ are along the bisectrix axis (1- or x-direction) and the transverse gradients are measured along the binary axis (2- or y-direction). The Corbino disks are formed with the cylindrical axis along the trigonal axis (also the direction of the applied magnetic field) so that the current directions are in the isotropic basal plane.

In zero field the transport tensors are all diagonal. Now the tensors of (1) are of theoretical interest, while the relationships between measured currents and gradients are given by (2) and (3). That is, $\sigma_{11}(0) = J_1/E_1^*$ (with $\vec{H} = 0$, $\nabla T = 0$ and $J_2 = J_3 = 0$) and $\epsilon_{11}(0) = -E_1^*/(\nabla T)_1$ (with $H = 0$, $\vec{J} = 0$ and $(\nabla T)_2 = (\nabla T)_3 = 0$). Then $\epsilon''_{11}(0)$, the quantity of theoretical interest, is given by $\epsilon''_{11} = \sigma_{11}(0) \times \epsilon_{11}(0)$, and Onsager principle requires $\epsilon''(0) = \pi''(0)/T$.

In the limit of high magnetic field, the electrical and thermal conductivity tensors are diagonal but the thermoelectric and Peltier tensors are antisymmetric with the diagonal elements of negligibly small magnitude (Tsai I). Under these conditions the measured quantities are $\epsilon'_{21} = E_2/w_1^*$ (with $\vec{J} = 0$ and $w_2^* = w_3^* = 0$) and $\pi'_{21} = -(\nabla T)_2/J_1$ (when $\vec{w}^* = 0$ and $J_2 = J_3 = 0$). The quantities of theoretical interest are then $\epsilon''_{21} = \epsilon'_{21}/\rho_{22}\gamma_{11}$ and $\pi''_{21} = \pi'_{21}/\rho_{11}\gamma_{22}$. The above relations, of course, are between the bulk properties. The presence of surface currents will yield measured values of the transport properties which are different from the bulk values. Empirical methods were developed in Tsai I for relating the measured values (designated by $\langle\ \rangle$) to the bulk values (designated by the subscript b). In the limit of high magnetic field the corrections are

$$\frac{\langle\epsilon'_{21}\rangle}{\epsilon'_{21b}} \approx \frac{\langle\pi'_{12}\rangle}{\pi'_{12b}} \approx \frac{\langle\rho_{22}\rangle}{\rho_{22b}} = \frac{1}{p_2}$$
$$\frac{\langle\epsilon'_{12}\rangle}{\epsilon_{12b}} \approx \frac{\langle\pi'_{21}\rangle}{\pi_{21b}} \approx \frac{\langle\rho_{11}\rangle}{\rho_{11b}} = \frac{1}{p_1} \qquad (4)$$

$$\langle \gamma_{11} \rangle = \langle \gamma_{22} \rangle = \frac{1}{\lambda_g} \text{ and } \rho_{11b} = \rho_{22b},$$

where the parameters p_1 and p_2 depend upon the details of the current distribution, λ_g is the lattice thermal conductivity.

In section B, theoretical expressions for the transport coefficients are developed which take into account the effects of electron-phonon drag. The treatment is aimed specifically at the case of antimony so that the expressions obtained for the limiting cases of zero and very high field can be feasibly compared with experiment.

In section C, the experimental determinations of the thermoelectric coefficients are described and analyzed in terms of the treatment given in section B. This analysis incorporates the results of transport measurements on antimony single crystals shaped into Corbino disks.

B - Transport Effects in the Limit of Strong Electron-Phonon Drag

In order to adequately describe the transport properties of antimony at low temperatures it is necessary to take into account the deviations of the charge carrier and phonon distribution functions from their equilibrium states. A number of authors have already considered the problem of the coupled electron and phonon Boltzmann equations.[5] Following Tsai II and III we have followed a scheme derived from the solution of Gurevitch and Korenblit[6] which has been extended

to cover cases where significant fractions of phonon population possess wave vectors larger than the Fermi wave vectors of the carriers (that is, a cut-off in the electron-phonon interaction must be introduced, which in the case at hand involves an effective Debye temperature).

The solutions, by this scheme, for the drift velocities of the carriers, $\vec{V}^{\pm}(\varepsilon)$ and the phonons $\vec{U}(\hbar\omega)$ are given in terms of the mean free paths of the carriers and phonons (Eqs. (3) and (4) of Tsai II) by

$$\vec{V}^{\pm}(\varepsilon) + \frac{e^{\pm}\ell^{\pm}}{p^{\pm}c}[\vec{H}\times\vec{V}^{\pm}(\varepsilon)] - \frac{\ell^{\pm}}{\ell_f^{\pm}}\langle U(x)\rangle_{\varepsilon}^{\pm} = \frac{\ell^{\pm}}{p^{\pm}}\left\{e^{\pm}\vec{E} - \frac{(\varepsilon-\zeta^{\pm})}{T}\vec{\nabla}T\right\} \tag{5}$$

$$\vec{U}(\hbar\omega) = -\sum_{\pm}\frac{L}{L^{\pm}}\int_{\varepsilon^{\pm}(q/2)}^{\infty} V^{\pm}(\varepsilon)\frac{\partial f_k^{\pm}}{\partial\varepsilon}d\varepsilon - \frac{L\,s_g}{T}\vec{\nabla}T \tag{6}$$

where

$\ell^{\pm}$ is the total mean free path (mfp) of the holes (electrons);

$\ell_f^{\pm}$ is the mfp of holes (electrons) due to scattering by phonons;

$\varepsilon = \varepsilon(k)$ is the energy of a carrier with momentum given by $\vec{p}^{\pm} = \hbar\vec{k}^{\pm}$;

$\zeta^{\pm}$ is the Fermi energy of the holes (electrons);

L is the total mfp of the phonons;

$L^{\pm}$ is the mfp due to scattering by holes (electrons);

$e^{\pm} = \pm 1.609 \times 10^{-19}$ Coul, the electronic charge;

s_g is the velocity of sound;

$\vec{q}$ is the phonon wave vector, hence $\hbar\omega = \hbar q\, s_g$.

$\langle\vec{U}(x)\rangle_{\varepsilon}^{\pm}$ is the phonon drift velocity averaged of q

between zero and $2k^{\pm}$ and is given approximately by

$$\langle \vec{U}(x) \rangle_{\varepsilon}^{\pm} = \int_{o}^{x^{\pm}(\varepsilon)} \frac{\vec{U}(x) x^5 e^x}{(e^x-1)^2} dx \Big/ \int_{o}^{x^{\pm}(\varepsilon)} \frac{e^x x^5 dx}{(e^x-1)^2}, \qquad (7)$$

where $x = \hbar s_g q/k_B T$ and $x^{\pm}(\varepsilon) = \hbar s_g (2k^{\pm})/k_B T$. Henceforth, the superscripts (+,-) and subscripts (h,e) refer to hole and electron pockets respectively. The integral in the denominator is just $\mathcal{J}_5(x)$, the Debye integral of order 5. Of particular interest are the limits of integration in (7), which are set by the cut off of the electron-phonon interaction. Thus, an upper limit q_i yields a limit $x_i = \hbar s_g q_i/k_B T$ which we may further simplify this ratio by writing $x_i = \theta_i^*/T$. In particular, if $q_i = 2k_F^{\pm}$ (where $k_F^{\pm}$ are the Fermi wave vectors) then $\theta_i^* = \theta_{\pm}^*$ (or alternatively $\theta_{h,e}^*$). Then $\theta_{\pm}^*$ can be regarded as the effective Debye temperature for the interaction of holes (electrons) with phonons. Henceforth, the subscript F designates quantities at the Fermi surface while the subscript f refers to phonons.

Let us first develop solutions to (5) and (6) assuming isothermal conditions ($\vec{\nabla T} = 0$). For this we will use the concept of the "4 regions" in q-space, introduced in Tsai II and III wherein the phonon drift velocities are ((15) of Tsai III):

$$\vec{U}(\hbar\omega) = \frac{L_1}{L^+} \vec{V}_F^+ + \frac{L_1}{L^-} \vec{V}_F^-, \quad \frac{1}{L_1} = \frac{1}{L^+} + \frac{1}{L^-} + \frac{1}{L_r}, \quad q \in \text{region I};$$

$$\vec{U}(\hbar\omega) = \frac{L_2}{L^+} \vec{V}_F^+, \qquad \frac{1}{L_2} = \frac{1}{L^+} + \frac{1}{L_r}, \qquad q \in \text{region II};$$

$$\vec{U}(\hbar\omega) = \frac{L_3}{L^+}\vec{V}_F^-, \qquad \frac{1}{L_3} = \frac{1}{L^-} + \frac{1}{L_r}, \qquad q \in \text{region III};$$

$$\vec{U}(\hbar\omega) = 0 \qquad\qquad q \in \text{region IV};$$

where L_r is the mfp due to scattering by mechanisms other than by holes or electrons.

In phonon q-space the four regions are:

Region I: phonons scattered by both holes and electrons;

Region II: phonons scattered only by holes;

Region III: phonons scattered only by electrons;

Region IV: no carrier-phonon scattering can occur.

In order to perform the calculations, the regions I, I + II and I + III will be approximated by spheres of radii q_l, q_h and q_e or by effective Debye temperatures θ_l^*, θ_h^* and θ_e^*, respectively. Region I corresponds essentially to the case treated by Gurevitch and Korenblit who as well assumed $\theta^*/T << 1$.

The substitution of $\vec{U}(\hbar\omega)$ (from Eqs. (8)) into (7) yields the averaged phonon drift velocities, $\langle\vec{U}(x)\rangle_\varepsilon^\pm$ which when substituted into (5) will lead to the determination of the carrier drift velocities $\vec{V}_F^\pm$. The iteration is usually terminated at this stage.

Even though general expressions for $\vec{V}_F^\pm$ may be obtained, we will consider only the cases of zero field large magnetic field and very large magnetic field.

The solution for zero field can be written

$$\vec{V}_F^{\pm} = \frac{1}{\Delta(0)} (\mu^{\pm} A^{\mp} - \mu^{\mp} B^{\pm}) \vec{E} \tag{9}$$

where $\mu^{\pm} = \frac{e^{\pm} \ell_F^{\pm}}{P_F^{\pm}}$ and $\Delta(0) = A^+A^- - B^+B^-$.

$$\frac{A^{\pm}}{\mu^{\pm}} = \frac{1}{\mu_r^{\pm}} - \frac{1}{\mu_f^{\pm}} \left[\left\langle \frac{L_{2,3}}{L^{\pm}} \right\rangle_{(\theta^*_{h,e}/T)} - 1 + \left\{ \left\langle \frac{L_1}{L^{\pm}} \right\rangle_{(\theta_1^*/T)} - \left\langle \frac{L_{2,3}}{L^{\pm}} \right\rangle_{(\theta_1^*/T)} \right\} \frac{\mathcal{J}_5(\theta_1^*/T)}{\mathcal{J}_5(\theta^*_{h,e}/T)} \right] \tag{10}$$

$$\frac{B^{\pm}}{\mu^{\pm}} = - \frac{1}{\mu_f^{\pm}} \left\langle \frac{L_1}{L^{\mp}} \right\rangle_{(\theta_1^*/T)} \frac{\mathcal{J}_5(\theta_1^*/T)}{\mathcal{J}_5(\theta^*_{h,e}/T)} \tag{11}$$

where $\mu_i^{\pm} = \frac{e^{\pm} \ell_i^{\pm}}{P_F^{\pm}}$ and i denotes r,f or no symbol. We will assume

$$\frac{1}{\ell^{\pm}} = \frac{1}{\ell_r^{\pm}} + \frac{1}{\ell_f^{\pm}},$$

where $\ell^{\pm}$ is the total mean free path of carriers, $\ell_f^{\pm}$ is the mfp due to scattering by phonons and $\ell_r^{\pm}$ is the mfp due to scattering by all other mechanisms.

In the presence of a magnetic field the drift velocities become, under isothermal conditions,

$$V_{F_x}^{\pm} = \frac{\Delta(0)}{\Delta(H)} \frac{E_x}{\mathcal{H}^+ \mathcal{H}^-} (\mu^{\pm} A^{\mp} - \mu^{\mp} B^{\pm}) + \frac{E_x}{\Delta(H)} \mu^{\mp} (A^{\pm} + B^{\pm}) \tag{12}$$

$$V_{F_y}^{\pm} = \frac{E_x}{\Delta(H)} \left[\mu^{\pm} \left(- \frac{(A^{\mp})^2}{\mathcal{H}^{\mp}} - \mathcal{H}^{\mp} + \frac{B^+B^-}{\mathcal{H}^{\pm}} \right) - \mu^{\mp} B^{\pm} \left(\frac{A^{\pm}}{\mathcal{H}^{\pm}} + \frac{A^{\mp}}{\mathcal{H}^{\mp}} \right) \right] \tag{13}$$

where $\Delta(H) = \frac{(\Delta(0))^2}{\mathcal{H}^+ \mathcal{H}^-} + \frac{(A^+\mathcal{H}^-)^2 + (A^-\mathcal{H}^+)^2 + 2B^+B^-\mathcal{H}^+\mathcal{H}^- + (\mathcal{H}^+\mathcal{H}^-)}{\mathcal{H}^+ \mathcal{H}^-}$

and $\mathcal{H}^{\pm} = \frac{\mu^{\pm} H}{c}$, which may be regarded as the ratio $(\omega_c \tau)$. Now $A^{\pm}$ and $B^{\pm}$ are in magnitude always less than unity, so that the high field limit is reached when $(\mathcal{H}^{\pm}) >> 1$. In this case $\Delta(H) \approx \mathcal{H}^{+}\mathcal{H}^{-}$ and then

$$V_{F_x}^{\pm} = \frac{E_x}{(\mathcal{H}^{+}\mathcal{H}^{-})} \mu^{\mp}(A^{\pm}+B^{\pm}) = \frac{(A^{\pm}+B^{\pm})E_x}{(H/c)^2 \mu^{\pm}} \tag{14}$$

$$V_{F_y}^{\pm} = - \frac{\mu^{\pm} \mathcal{H}^{\mp} E_x}{\mathcal{H}^{+}\mathcal{H}^{-}} = - \frac{E}{(H/c)}. \tag{15}$$

Under isothermal conditions (1) becomes

$\vec{J} = \hat{\sigma}\vec{E}^*$ and $\vec{w}^* = -\hat{\pi}''\vec{E}^*$. The conductivity tensor, $\hat{\sigma}$, may be found from the kinetic formula

$$\vec{J} = n[e^{+}\vec{v}_F^{+} + e^{-}\vec{v}_F^{-}] \tag{16}$$

where the $\vec{v}_F^{\pm}$ are substituted from (9) or (14) and (15). On the other hand, the heat current, $\vec{w}^*$, arises from two currents: $\vec{w}_c$ which is heat transported by carriers with drift velocities $\vec{v}_F^{\pm}$, and $\vec{w}_g^*$ which is heat transported by phonons whose drift velocity arises from the carrier-phonon interaction. The heat current, $\vec{w}_c$ can be found for carriers in standard energy bands characterized by effective masses $m^{\pm}$ and Fermi energies ζ^{+}.

$$\vec{w}_c = \sum_{\pm} \frac{2\sqrt{2}(m^{\pm})^{3/2}\nu^{\pm}}{3\pi^2\hbar^3} \int (\varepsilon-\zeta^{\pm})\varepsilon^{3/2}(-\frac{\partial f^{\circ}}{\partial \varepsilon})\vec{v}^{\pm} d\varepsilon \tag{17}$$

$$= \frac{\pi^2(k_B T)^2}{3}\left\{ Z^{+}\vec{v}_F^{+} + Z^{-}\vec{v}_F^{-} + 2n\left[\frac{\partial \vec{v}^{+}}{\partial \varepsilon}\bigg|_{\zeta^{+}} + \frac{\partial v^{-}}{\partial \varepsilon}\bigg|_{\zeta^{-}} \right] \right\} \tag{18}$$

where $Z^{\pm}$ is the density states at the Fermi surface and $\nu^{\pm}$ is the number of distinct hole (electron) pockets.

The phonon contribution, for a single polarization branch, to the heat current is

$$\vec{w}_g^* = -\frac{1}{(2\pi)^3} \int \hbar\omega \vec{s}_g (\vec{U}\cdot\hbar\vec{q}) \frac{\partial N^o}{\partial(\hbar\omega)} d^3q. \tag{19}$$

This integral may be evaluated directly by substitution of (9) or (14) and (15) into (6) and then the resulting $\vec{U}$ into (19) yielding

$$\vec{w}_g = 3NkT\left(\frac{T}{\theta_D}\right)^3 \left[\left\{ \left[\frac{L_1}{L^+}\right]_{\theta_1^*/T} \vec{V}_F^+ + \left[\frac{L_1}{L^-}\right]_{\theta_1^*/T} \vec{V}_F^- \right\} \mathcal{J}_4\left(\frac{\theta_1^*}{T}\right) \right.$$

$$+ \left[\frac{L_2}{L^+}\right]_{\theta_h^*/T} \vec{V}_F^+ \left(\mathcal{J}_4\left(\frac{\theta_h^*}{T}\right) - \mathcal{J}_4\left(\frac{\theta_1^*}{T}\right) \right)$$

$$\left. + \left[\frac{L_3}{L^-}\right]_{\theta_e^*/T} \vec{V}_F^- \left(\mathcal{J}_4\left(\frac{\theta_e^*}{T}\right) - \mathcal{J}_4\left(\frac{\theta_1^*}{T}\right) \right) \right], \tag{20}$$

where

$$[X]_{x_i} = \frac{1}{\mathcal{J}_4(x_i)} \int_0^{x_i} \frac{X\, e^x x^4\, dx}{(e^x-1)^2}.$$

The problem of dealing with these complicated averages is considerably simplified because of the following characteristics. First, the expected values x_i differ by less than a factor of 2. Secondly, the ratios $L_i/L^{\pm}$ are slowly varying functions of q, because by far, the strongest source of phonon scattering is the carrier-phonon interaction. That is to say, $L_i << L_r$. Thus, the averages $[X]_{x_i}$ and $\langle X\rangle_{x_i}$ are practically equal and nearly independent of x_i.

In the following analyses two drag approximations will be employed. They are first, full drag which is characterized

by $L_r \to \infty$. Thus

$$\left\langle \frac{L_1}{L^{\pm}} \right\rangle_{x_i} \approx \left[\frac{L_1}{L^{\pm}} \right]_{x_i} = \Gamma_o^{\pm}$$

where $\Gamma_o^+ + \Gamma_o^- = 1$ and

$$\left\langle \frac{L_{2,3}}{L^{\pm}} \right\rangle_{x_i} = \left[\frac{L_{2,3}}{L^{\pm}} \right]_{x_i} = 1.$$

That is to say, the phonons are scattered only by carriers. Second, strong drag, which is characterized by $L^{\pm} \ll L_r$, that is to say, phonon scattering by residual mechanisms is minor but not negligible in its contribution. Thus,

$$\left\langle \frac{L_1}{L^{\pm}} \right\rangle_{x_i} \approx \left[\frac{L_1}{L^{\pm}} \right]_{x_i} = \Gamma^{\pm}$$

where $\Gamma^+ + \Gamma^- = 1 - \gamma_1$ and

$$\left\langle \frac{L_{2,3}}{L^{\pm}} \right\rangle_{x_i} \approx \left[\frac{L_{2,3}}{L^{\pm}} \right]_{x_i} = 1 - \gamma_{2,3}$$

where γ_i are all small compared to unity.

a. Electrical conductivity in zero magnetic field.

Equations (9) and (16) yield

$$\sigma_{11}(0) = \sigma = \frac{n}{\Delta(0)} \left[e^+\mu^+(A^-+B^-) + e^-\mu^-(A^++B^+) \right] . \qquad (21)$$

The evaluation of this expression is most easily carried out by using the full drag approximation which when applied to (10) and (11) gives

$$A^{\pm} = \frac{\ell^{\pm}}{\ell_r^{\pm}} - B^{\pm}; \quad B^{\pm} = -\Gamma^{\mp} \frac{\ell^{\pm}}{\ell_f^{\pm}} \frac{\mathcal{J}_5(\theta_1^*/T)}{\mathcal{J}_5(\theta_{h,e}/T)} .$$

These expressions when substituted into (21) lead to [7]

$\rho = \frac{1}{\sigma} = \rho_r + \rho_{id}$ where

$$\rho_r = \frac{1}{ne^2}\left[\frac{\ell_{Fr}^{+}}{P_F^{+}} + \frac{\ell_{Fr}^{-}}{P_F^{-}}\right]^{-1} \tag{22}$$

and

$$\rho_{id} = \rho_r\left\{\frac{\ell_{Fr}^{+}\ \Gamma^{-}}{\ell_{Ff}^{+}\ \mathcal{J}_5(\theta_h^*/T)} + \frac{\ell_{Fr}^{-}\ \Gamma^{-}}{\ell_{Ff}^{-}\ \mathcal{J}_5(\theta_e^*/T)}\right\}\mathcal{J}_5\left(\frac{\theta_1^*}{T}\right). \tag{23}$$

There is no advantage in this calculation in employing the more cumbersome strong drag approximation since the final results are not significantly different from (22) and (23). This can be understood physically by recourse to (8). The carrier-phonon scattering in regions II and III contributes very little to the ideal resistivity since the phonons in the respective regions attain very nearly the drift velocities of the carriers even in the strong drag condition. However, the phonons of region I are subjected to the pressure of both hole and electron drift and this feature is inherent in the form of (23). Scattering of phonons by residual mechanisms is negligible in comparison with carrier-phonon scattering if the phonon drift is markedly different from the carrier drifts.

b. Thermoelectric effect in zero magnetic field.

The thermoelectric power $\varepsilon_{11}(0) = \varepsilon$ will be formally determined from

$$\varepsilon = -\frac{\rho\pi_{11}''(0)}{T} = \frac{\rho}{T}\frac{w^*}{E^*} = \frac{\rho(w_c^* + w_g^*)}{TE^*} = \varepsilon_c + \varepsilon_g.$$

The carrier diffusion term, ε_c, is calculated from (18) neglecting the energy derivative of the drift velocities.[8]

For this term the full drag approximation will be employed since we are here calculating the heat current carried by the drifting carriers and the attenuation of these velocities by phonon-residual scattering is very slight. Thus, for full drag

$$V_F^{\pm} = E^* \frac{\rho_r}{\rho}\left\{ \mu_r^{\pm}\left(1+ \frac{\ell_r^{\mp}\Gamma^{\pm}}{\ell_f^{\mp}} \frac{\mathcal{J}_5(\theta_1^*/T)}{\mathcal{J}_5(\theta_{\mp}^*/T)}\right) + \mu_r^{\mp} \frac{\ell_r^{\pm}\Gamma^{\mp}\mathcal{J}_5(\theta_1^*/T)}{\ell_f^{\pm}\mathcal{J}_5(\theta_{\pm}^*/T)}\right\} \tag{24}$$

$$\epsilon_c = \frac{\pi^2 kT}{3}\rho_r\left\{\mu_r^+Z^+ + \mu_r^-Z^- + (Z^+ + Z^-)\sum_{\pm}\mu_r^{\pm}\frac{\ell_{Fr}^{\mp}\Gamma^{\pm}\mathcal{J}_5(\theta_1^*/T)}{\ell_{Ff}^{\mp}\mathcal{J}_5(\theta_{\mp}^*/T)}\right\} .$$

The first two terms describe the contribution arising from carrier diffusion in the case carrier-residual scattering and they have the form calculated in the standard relaxation time approximation. The third term also arises from carrier diffusion, but is due to the effects of the interaction between holes and electrons through their respective interactions with the phonons. This is the mutual drag term.

The phonon contribution to ϵ is determined from (20) with the strong drag assumption used for evaluating $\vec{V}_F^{\pm}$. This refinement is necessary because the phonon-residual scattering significantly alters $\vec{w}_g^*$ even though the carrier-phonon scattering is predominant.

$$w_g^* = 3NkT\left(\frac{T}{\Theta_D}\right)^3\left\{\sum_{\pm} V_F^{\pm}[(1-\gamma_{2,3})\mathcal{J}_4(\theta_{\pm}^*/T) - (\Gamma^{\mp}-\gamma_1)\mathcal{J}_4(\theta_1^*)]\right\} \tag{25}$$

$$\epsilon_g = 3Nk\left(\frac{T}{\theta_D}\right)^3(1-\bar{\gamma})\rho_r\left\{\sum_{\pm}\mu_r^{\pm}[\mathcal{J}_4(\frac{\theta_{\pm}^*}{T}) - \Gamma^{\mp}\mathcal{J}_4(\theta_1^*/T)]\right.$$

$$\left. + [\mathcal{J}_4(\frac{\theta_+^*}{T}) + \mathcal{J}_4(\frac{\theta_-^*}{T}) - \mathcal{J}_4(\frac{\theta_1^*}{T})]\sum_{\pm}\mu_r^{\pm}\frac{\ell_{Fr}^{\mp}\Gamma^{\pm}\mathcal{J}_5(\theta_1^*/T)}{\ell_{Ff}^{\mp}\mathcal{J}_5(\theta_{\mp}^*/T)}\right\} . \tag{26}$$

Here the dependence upon phonon-residual scattering has been drastically reduced to a single parameter $\bar{\gamma}$ and the form of ϵ_g further simplified so that comparison with experiment can be made. This is permissible because the γ_i are all less than 0.05. The first term describes the simple drag contribution to w_g^*; that is, drifting holes and electrons set phonons into motion. The second term can be interpreted as the mutual drag contribution wherein the net drift of the phonons reacts on the carriers to alter the total flow of heat w*. The mobility factor,

$$\alpha_m = \sum_{\pm} \frac{\mu_r^{\pm} \ell_{Fr}^{\mp} \Gamma^{\pm} \mathcal{J}_5(\theta_1^*/T)}{\ell_{Ff}^{\mp} \mathcal{J}_5(\theta_{\mp}^*/T)},$$

appears as the second term in both (24) and (26) and can be evaluated explicitly for the case in which the Fermi surfaces are spherical and the phonon distribution is described by the Debye model. Using the expressions of Tsai III, sec. II, we find $\alpha_m = 0$. If the scattering of phonons by both holes and electrons is isotropic in q-space, then the momentum imparted to the phonons of region I by drifting holes is exactly off set by that imparted by drifting electrons. If, as in the case of antimony, the hole and electron pockets are highly ellipsoidal, then the phonon scattering is no longer isotropic in q-space and hence a net phonon drift must be generated so that total momentum is conserved. This aspect of the calculation of α_m will be handled empirically

by introducing the anisotropic constants $a^{\pm}$.[9] Specifically, $\ell^{\pm}_{Ff}$ is replaced by $a^{\pm}\ell^{\pm}_{Ff}$, however, impurity scattering is regarded as isotropic so that no anisotropic correction is applied to $\ell^{\pm}_{Fr}$. Then by noting the similarities between the terms in (23) and those of α_m, we may write[10]

$$\alpha_m = \frac{a^+ - a^-}{\left|\frac{a^-}{\mu_r^-}\right| + \left|\frac{a^+}{\mu_r^+}\right|} \left[\frac{\rho_{id}}{\rho_r}\right]. \tag{27}$$

The thermoelectric power coefficient may be written in an even simpler form by defining

$$R = \left|\frac{\mu_r^-}{\mu_r^+}\right|$$

then

$$\begin{aligned}
\varepsilon = \varepsilon_{c_1} + \varepsilon_{c_2} + \varepsilon_{g_1} + \varepsilon_{g_2} &= \frac{\pi^2 k^2 T}{3en} \frac{Z^+ - RZ^-}{1 + R} \\
&+ \frac{\pi^2 k^2 T}{3}(Z^+ + Z^-)\left\{\frac{a^+ - a^-}{a^- + Ra^+} |\mu_r^-| \rho_{id}\right\} \\
&+ 3Nk\left(\frac{T}{\theta_D}\right)^3 \frac{(1-\bar{\gamma})}{ne(1+R)}\left[\mathcal{J}_4\left(\frac{\theta_+^*}{T}\right) - \mathcal{J}_4\left(\frac{\theta_-^*}{T}\right) - (\Gamma^- - R\Gamma^+)\mathcal{J}_4\left(\frac{\theta_1^*}{T}\right)\right] \\
&+ 3Nk\left(\frac{T}{\theta_D}\right)^3 (1-\bar{\gamma})\left[\mathcal{J}_4\left(\frac{\theta_+^*}{T}\right) + \mathcal{J}_4\left(\frac{\theta_-^*}{T}\right) - \mathcal{J}_4\left(\frac{\theta_1^*}{T}\right)\right] \\
&\times \left\{\frac{a^+ - a^-}{a^- + Ra^+} |\mu_r^-| \rho_{id}\right\} .
\end{aligned} \tag{28}$$

The second and fourth terms can be written $\varepsilon_{c_2} + \varepsilon_{g_2}$ $= [C_c + \frac{1}{3}(1 - \bar{\gamma})C_g^*]\alpha_m \rho_r$ where C_c is the specific heat of the carriers and $(1-\bar{\gamma})C_g^*$ is the specific heat of the phonons

dragged by the carriers. The coefficient α_m can be regarded as a "mutual drag mobility". The factor

$$[\mathcal{J}_4(\frac{\theta_+^*}{T}) + \mathcal{J}_4(\frac{\theta_-^*}{T}) - \mathcal{J}_4(\frac{\theta_1^*}{T})]$$

in the ε_{g_2} term is the result of those phonons with the same drift velocity in all the three regions, and for the analysis of experimental results it may be replaced by $\mathcal{J}_4(\frac{\theta_4^*}{T})$. (It is interesting to note that in the study of Nernst-Ettingshausen coefficient at high field [discussed later] where the phonons being dragged with the same drift velocity by both carriers, the factor $\mathcal{J}_4(\frac{\theta_4^*}{T})$ will appear automatically.) Then,

$$\varepsilon_{c_2} + \varepsilon_{g_2} = [\frac{\pi^2k^2T}{3}(Z^+ + Z^-) + 3Nk(\frac{T}{\theta_D})^3(1-\bar{\gamma})\mathcal{J}_4(\frac{\theta_4^*}{T})]\alpha_m\rho_r \quad (29a)$$

or

$$\varepsilon_{c_2} + \varepsilon_{g_2} = \frac{\pi^2k^2T}{3} Z_{eff}\, \alpha_m\rho_r \quad (29b)$$

where Z_{eff} is the effective density of states and can be written as

$$Z_{eff} = Z^+ + Z^- + \frac{9N}{\pi^2k}\frac{T^2}{\theta_D^3}(1-\bar{\gamma})\mathcal{J}_4(\frac{\theta_4^*}{T}). \quad (30a)$$

The coefficient α_m can also be written in more useful form

$$\alpha_m = \frac{a^+-a^-}{a^-+Ra^+}\frac{R}{1+R}\frac{1}{ne}\frac{\rho_{id}}{\rho_r^2}. \quad (30b)$$

Therefore,

$$\frac{\varepsilon_{c_2}+\varepsilon_{g_2}}{T} = \frac{\pi^2k^2}{3} Z_{eff}\frac{a^+-a^-}{a^-+Ra^+}\frac{R}{1+R}\frac{1}{ne}\frac{\rho_{id}}{\rho_r}. \quad (29c)$$

c. Electrical conductivity in high magnetic field.

In the limit of very high magnetic field we may use (12) in (16) to give for the isothermal conductivity

$$\sigma_{11}(H) = n(\frac{c^2}{H^2})\left\{\frac{p_F^+}{\ell_r^+} + \frac{p_F^-}{\ell_r^-} + \bar{\gamma}\left[\frac{p_F^+}{\ell_f^+} + \frac{p_F^-}{\ell_f^-}\right]\right\}. \quad (31)$$

Here,we have employed the strong drag approximation and lumped the γ_i into a single effective $\bar{\gamma}$. If the drag was full, then $\gamma_i = 0$ and hence,

$$\sigma_{11}(H) = n\left(\frac{c}{H}\right)^2 \left[\frac{p_F^+}{\ell_r^+} + \frac{p_F^-}{\ell_r^-} \right] , \tag{32}$$

which is temperature independent. Thus, the observed weak temperature dependence of the magnetoconductivity arises from the minor phonon-residual scattering (Tsai II).

d. Thermoelectric effects in high magnetic fields.

The analysis of high field thermoelectric effects is greatly simplified with the realization from (12) and (13) that

$$V_{Fx}^{\pm}/V_{Fy}^{\pm} \approx \frac{1}{\mathcal{H}^{\pm}} < 10^{-2},$$

and thereby we may neglect the $U_x(\hbar\omega)$ in comparison with $U_y(\hbar\omega)$ in (8). Thus,

$$\begin{aligned} U_y &= (1 - \gamma_1)\,\frac{cE}{H} && q \in \text{region I} \\ U_y &= (1 - \gamma_2)\,\frac{cE}{H} && q \in \text{region II} \\ U_y &= (1 - \gamma_3)\,\frac{cE}{H} && q \in \text{region III} \\ U_y &= 0 && q \in \text{region IV.} \end{aligned} \tag{33a}$$

The analysis is further simplified because the γ_i are all nearly equal and much smaller than 1, so that we may replace $1 - \gamma_i$ by $1 - \bar{\gamma}$. Furthermore, the total volume composed of regions I + II + III may be regarded as a sphere of radius

q_4 giving the effective Debye temperature θ_4^*. Thus,

$$U_y = (1 - \bar{\gamma})\,\frac{cE}{H} \qquad q \in \text{region IV}$$
$$U_y = 0 \qquad q \ni \text{region IV}. \tag{33b}$$

The thermoelectric coefficient, $\varepsilon_{11}(H)$, was not investigated in detail here because preliminary measurements showed it to be very small. It can be estimated by substituting (12) into (18) and (20). The resulting expression shows that $\varepsilon_{11}(H)$ is field independent and remains close to the zero field value. On the other hand, the Nernst-Ettingshausen coefficient $\varepsilon_{12}(H)$, rises linearly with magnetic field. By substituting (13) into (18) and (20), we find

$$\varepsilon''_{12}(H) = -\frac{c}{H}\left[\frac{\pi^2 kT}{3}(Z^+ + Z^-) + 3Nk\left(\frac{T}{\theta_D}\right)^3(1-\bar{\gamma})\,\mathcal{J}_4\left(\frac{\theta_4^*}{T}\right) + \Delta\right]$$
$$= -\frac{c}{H}\left[C_c + \left(\frac{1-\bar{\gamma}}{3}\right)C_g^* + \Delta\right] \tag{34a}$$

with the correction term given by

$$\Delta = \sum_i 3Nk\left(\frac{T}{\theta_D}\right)^3 \delta\gamma_i\,\mathcal{J}_4\left(\frac{\theta_i^*}{T}\right)$$

where the $\delta\gamma_i$ are $\bar{\gamma} - \gamma_2$, $\bar{\gamma} - \gamma_3$ and $\bar{\gamma} - [\gamma_2 + \gamma_3 - \gamma_1]$ and the θ_i^* are respectively θ_+^*, θ_-^* and θ_1^*. In the case of strong drag the $\delta\gamma_i$ are differences between quantities which are both small and nearly equal so that Δ may be neglected.

Finally, using the concept of effective density of states the Nernst-Ettingshausen coefficient may be written

$$\varepsilon''_{12} = -\frac{c}{H}\,\frac{\pi^2 kT}{3}\,Z_{eff}. \tag{34b}$$

C - Experimental Results and Discussion

Direct measurements of thermoelectric power were carried out on a slab-shaped single crystal sample of antimony (sample C of Tsai III). The heat current, $\vec{w}^*$, was directed along the bisectrix axis (x- or 1-direction) with $w_2^* = \vec{w}_3 = 0$, $J_2 = J_3 = 0$. $(\nabla T)_1$ was measured in a conventional manner. The resulting potential difference was measured with a Keithley 800 picovoltmeter. In this system the measuring circuit consisted only of superconducting wires connected to the sample. Since superconductors do not develop thermoelectric voltages in zero magnetic field, this method obviates the thermoelectric leads correction.

The zero field data are shown in Fig. 1 where ε/T is plotted against T^2. In order to interpret these measurements in terms of the development of the previous section, we write

$$\frac{\varepsilon}{T} = \frac{\varepsilon_{c_1}}{T} + (\varepsilon_{c_2} + \varepsilon_{g_2}) \frac{1}{T} + \frac{\varepsilon_{g_1}}{T} .$$

From (28) we recognize the first term,

$$\frac{\varepsilon_{c_1}}{T} = \frac{\pi k^2}{3en} \left[\frac{Z^+ - RZ^-}{1 + R} \right] ,$$

as the carrier diffusive term, a constant to which the measured ε/T will tend as T goes to zero. The calculated value of this term is $+0.18\ \mu v/k^2$,[11] which is consistent with a reasonable extrapolation of the data to zero temperature.

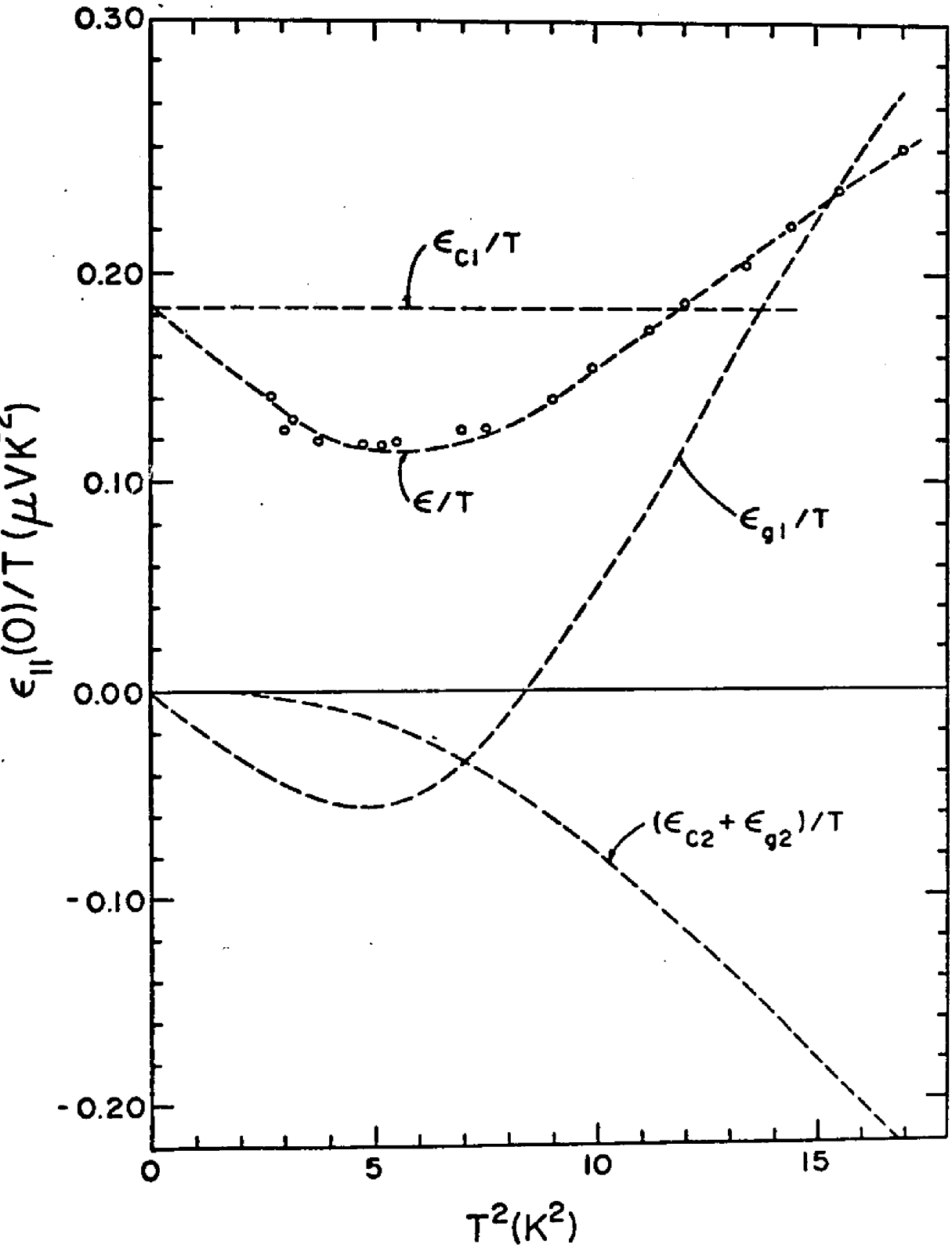
0.30
0.20
0.10
0.00
-0.10
-0.20
0
5
10
15
$\epsilon_{11}(0)/T\ (\mu VK^{-2})$
$T^2(K^2)$
ϵ_{c1}/T
ϵ/T
ϵ_{g1}/T
$(\epsilon_{c2}+\epsilon_{g2})/T$

Fig. 1

The second term, that is, the mutual drag term,

$$\frac{\varepsilon_{c_2} + \varepsilon_{g_2}}{T} = \frac{\pi^2 k^2}{3} Z_{eff} \left(\frac{a^+ - a^-}{a^- + Ra^+}\right)\left(\frac{R}{1+R}\right)\frac{1}{ne}\frac{\rho_{id}}{\rho_r}$$

would be zero if the semimetal were isotropic with spherical Fermi pockets (that is to say, if $a^+ - a^- = 0$). The strong temperature dependence arises from both Z_{eff} and ρ_{id}. The first quantity has been investigated through the Nernst-Ettingshausen and Ettingshasuen effects (see next section) and the latter was measured in Tsai III. The greatest source of uncertainty in this term is the anisotropy factor,

$$\left(\frac{a^+ - a^-}{Ra^+ + a^-}\right)\left(\frac{R}{1+R}\right) ;$$

by taking the previously accepted values $a^+ = 1.5$, $a^- = 2.4$ and $R = 0.24$, we obtained[11] the value -0.063. The closest fit of the theory to the data was made not with this value, but with a value, -0.042. This discrepancy is not surprising in view of the uncertainties in the coefficients $a^{\pm}$ and the approximation made in formulating this term.

The last term, the simple drag term, is

$$\frac{\varepsilon_{g_1}}{T} = 3Nk\frac{T^2}{\theta_D^3}\frac{(1-\bar{\gamma})}{ne(1+R)}\left[\mathcal{J}_4\left(\frac{\theta_+^*}{T}\right) - R\,\mathcal{J}_4\left(\frac{\theta_-^*}{T}\right) - (\Gamma^- - R\Gamma^+)\mathcal{J}_4\left(\frac{\theta_1^*}{T}\right)\right] .$$

Of the three terms so far considered only this last one can be associated with the minimum in the observed temperature dependence because the first two possess monotonic temperature dependences. That is to say, the expression,

involving the Debye integrals, must be negative at very low temperature, then decreasing to a minimum near 2 K and then increasing. The process of fitting the data will then determine $\Gamma^{\pm}$. However, effective scattering temperatures must also be taken into account. Fitting the data by independent adjustment of the θ_i^* is out of the question, since the volumes of the various regions in q-space are in more or less fixed ratios.

A rough estimate of the q-region size leads to the approximate comparative values

$$\frac{\theta_e^*}{1} = \frac{\theta_h^*}{.794} = \frac{\theta_{1r}^*}{.55} = \frac{\theta_{1b}^*}{.80} = \frac{\theta_2^*}{1.03} = \frac{\theta_3^*}{1.34} = \frac{\theta_4^*}{1.46}, \qquad (35)$$

where the value θ_+^* appearing in the ε_{g_1} term could be associated with a single hole pocket (θ_h^*) or with the volume of the composite image in q-space corresponding to the set of three pairs of hole pockets (θ_2^*). Similarly, θ_-^* can either be linked to a single electron pocket (θ_e^*) or to the composite image volume associated with the set of electron pockets (θ_3^*). As for θ_1^*, it may correspond either to the restricted zone common to all pocket images (θ_{1r}^*) or a broader region of the phonon-electron and phonon-hole interaction overlap (θ_{1b}^*). The more likely situation is intermediate between the preceding possibilities and probably very close to the set of θ_2^*, θ_3^*, and θ_{1b}^* values.

Fitting will be done using this θ^* sequence and writing the $\mathcal{J}_4$ term: $\mathcal{J}_4(1.28z) - R\,\mathcal{J}_4(1.672z) - (\Gamma^- - \Gamma^+ R)\,\mathcal{J}_4(z)$.

where $z = \theta^{*}_{1b}/T$. It is found that this function is very sensitive to the θ^{*} sequence, as well as the coefficient R and $\Gamma^{-}-\Gamma^{+}R$. Using R = 0.24, we obtained the best value for $\Gamma^{-}-\Gamma^{+}R \approx 0.82$, that is, $\Gamma^{-} = 0.85$ and $\Gamma^{+}+\bar{\gamma} = 0.15$.

The contribution of the term ε_{g_1}/T shown in Fig. 1 corresponds to $1-\bar{\gamma} = 0.97$ and $1+R = 1.24$. The value used for $\theta_D = 232$ K is that obtained from the π''_{21} data in the next section.

The composite curve for $\varepsilon/T = (\varepsilon_{c_1} + \varepsilon_{c_2} + \varepsilon_{g_2} + \varepsilon_{g_1})/T$ is also shown in the same figure and found remarkably close to the experimental points. It is interesting to note that this almost perfect fit was obtained using in the calculation only recognized values, except for the 33% lowering in the value of the anisotropy term $\frac{a^{-}-a^{+}}{a^{+}-Ra^{+}} \frac{a^{-}-a^{+}}{a^{-}+Ra^{+}} \frac{R}{1+R}$, which is justifiable, in a way, because of the uncertainty in the coefficients a^{+}, a^{-}. This good fit could still be improved by a slight variation over some of the parameters used. Nevertheless, this was not done as theoretical approximations, such as isotropy, phonon branches degenerating, etc., implied greater indetermination than the actual experimental discrepancy.

Let us simply note that the value used for $\theta_D = 232$ K (resulting from the ε''_{12} analysis) is about 10% larger than that obtained from direct specific measurement[13] ($\theta_D \approx 210$ K).

The value used for $\theta^*_{lb} \approx 22.5$ K corresponds to the values $\theta^*_e \approx 28.1$ K and $\theta^*_h \approx 22.5$ K which is in agreement with the Debye temperatures obtained from magnetoconductivity (Tsai II) and zero field thermal conductivity (Tsai III). We may note that the value of θ^*_l is different than that obtained from ideal resistivity measurement with, in this case, θ^*_l in the range 14 to 15 K. As pointed out earlier, the q-region I is poorly defined when the sets of three electron-pockets and six hole-pockets are considered yielding upper and lower limits for θ^*_{lb} and θ^*_{lr}. Apparently the thermoelectric data seem to depend on the upper limit, whereas the compensated drag effect in the ideal resistivity depends on the lower limit.

We may note also that comparative phonon-carrier interaction strength is given by $\Gamma^-/\Gamma^+ = \frac{\nu^-}{\nu^+}\left(\frac{C^- m^*_-}{C^+ m^*_+}\right)^2 \frac{a^+}{a^-}$. A rough estimate of this value was obtained with $\Gamma^-/\Gamma^+ \approx 7$. Such a value would yield the deformation potential ratio $C^-/C^+ \approx 2$, an estimate already obtained from other considerations (Tsai III).

Anisotropy should affect the term, ε_{c_1}, as well as it was shown to affect the other terms. This point was not investigated; it was felt that the overall general conclusion of a satisfactory fit between theory and experiment would not be affected.

D - Nernst-Ettingshausen and Ettingshausen Effects

These two effects are seemingly ideal for investigation because of their relatively simple theoretical expressions (34) and their direct experimental determinations. However, as previously noted (Tsai I), the interpretation is beset by inconsistencies. First of all, the Bridgman relations are not satisfied, that is, $\pi'_{21} \neq \varepsilon'_{21}T$ and therefore $\pi''_{21} \neq \varepsilon''_{21}T$. Secondly, different samples have yielded different values for

$$\varepsilon''_{21} = -\frac{\pi k^2 T}{3}\frac{c}{H}\left[Z^+ + Z^- + \frac{9N}{\pi k}\frac{T^2}{(\theta_D)^3}(1-\bar{\gamma})\mathcal{J}_4\left(\frac{\theta_4^*}{T}\right)\right]$$

which is disturbing since this quantity is independent of the electron and hole mobilities and conceivably the difference between samples would have to be ascribed to variations in $(1-\bar{\gamma})$. However, this quantity shows nowhere near the variation from sample to sample required to account for these discrepancies.

The measured values of Z_{eff}, derived from measurements of π'_{21} and ε'_{21} are plotted against T^2 in Fig. 2.. We see that the results by several investigators fall into two groups - those determined from $\langle\varepsilon'_{12}\rangle$ data (the brackets designate measured quantities) and those from $\langle\pi'_{12}\rangle$ data. The grouping of the $Z_{eff}(\varepsilon')$ values for samples designated A, C and Long may result from the similarities in sample size and preparation. However, it is also to be noted that the points labeled Blewer are nearly 20% smaller than those of the main group, whereas the values obtained from sample D are nearly 30% larger than this group. Thus, it appears that the Nernst-Ettingshausen effect is somewhat more sensitive to the condition of the sample than is apparent in (30a). On the other hand, the $Z_{eff}(\pi')$ for samples C and D are in far better agreement than the $Z_{eff}(\varepsilon')$ data for these samples. Further, it can be seen that data labeled $(\langle\rho_{11}\rangle/\rho_{11b})$ $Z_{eff}(\varepsilon')$ sample C fits to some degree with the $Z_{eff}(\pi')$ data.

By fitting these groups of data to (30a) with $1-\bar{\gamma} = 0.96$, we find for these groups the broken lines in Fig. 2, and the following parameters: $Z_{eff}(\varepsilon')$ data: $Z^+ + Z^- = 1.35 \times 10^{33}$ (erg cm^3), $\theta_D = 202$ K and $\theta_4^* = 32$ K; $Z_{eff}(\pi')$: $Z^+ + Z^- = 0.85 \times 10^3$ (erg cm^3)$^{-1}$, $\theta_D = 232$ K and $\theta_4^* = 35$ K. The measurements of ε'_{21} by Blewer, et al., yielded the intermediate values $Z^+ + Z^- = 1.10 \times 10^{33}$ (erg cm^3)$^{-1}$ $\theta_D = 218$ K, while their specific heat measurements yielded $Z^+ + Z^- = 0.97 \times 10^{33}$ (erg cm^3)$^{-1}$ and $\theta_D = 211$ K.

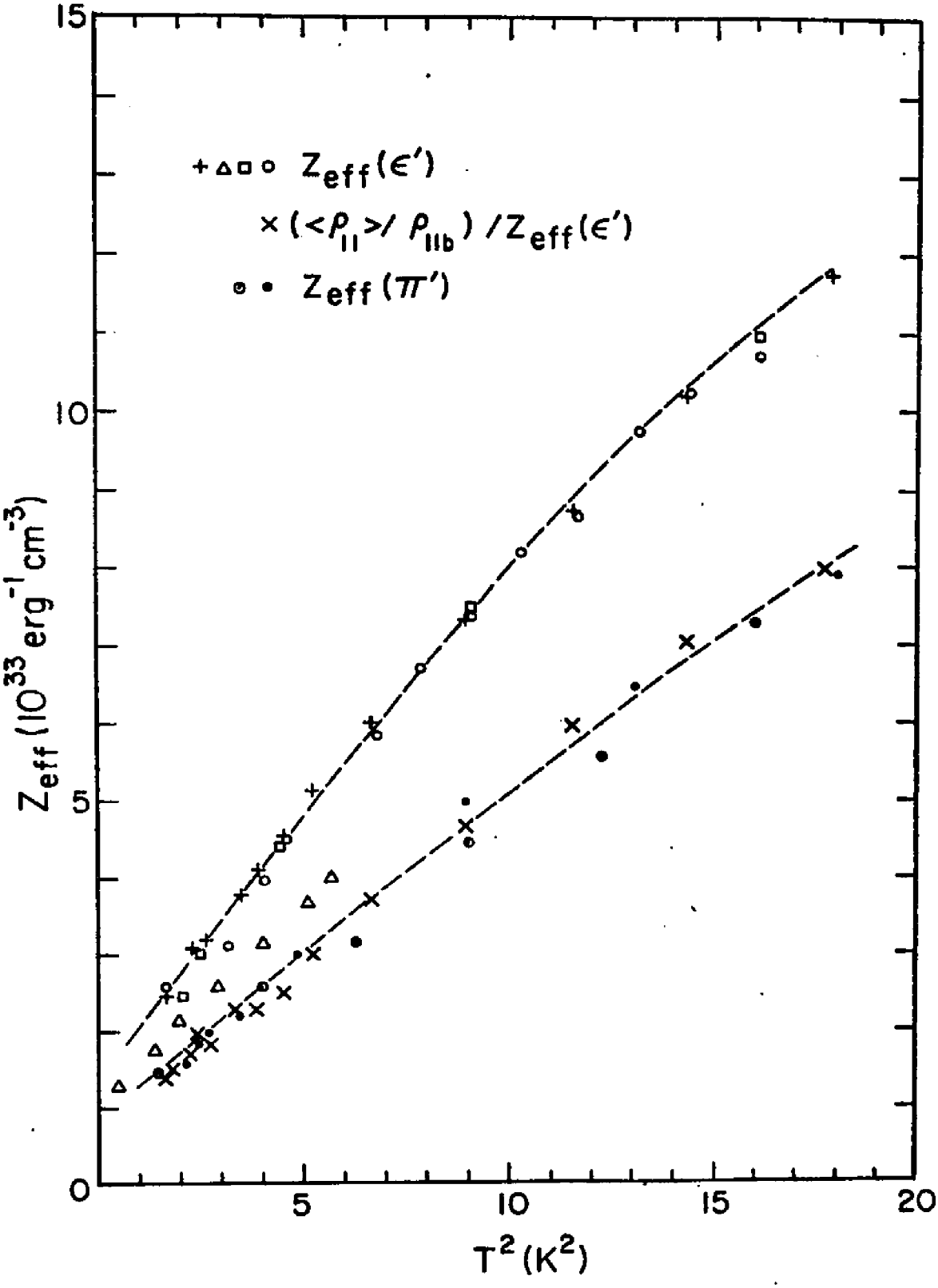
15
10
5
0
5
10
15
20
+ △ □ ○ $Z_{eff}(\epsilon')$
× $(\langle\rho_{11}\rangle / \rho_{11b}) / Z_{eff}(\epsilon')$
⊙ • $Z_{eff}(\pi')$
$Z_{eff}\,(10^{33}\,erg^{-1}cm^{-3})$
$T^2\,(K^2)$

Fig. 2

The spread of the values derived from transport measurements has been ascribed to the presence of surface currents and several empirical models have been developed with the objective of estimating bulk values of the transport coefficients from the measured ones (Tsai I). Even these crude models show that the presence of superficial conduction affects the various transport coefficients differently, particularly the process of obtaining ε''_{21} and π''_{21}.

The relations between bulk quantities are especially simple when the negligible quantities are dropped, that is,

$$\varepsilon''_{21b} = \frac{\varepsilon'_{21b}}{\rho_{22b}\,\gamma_{11b}} \text{ and } \pi''_{21b} = \frac{\pi'_{21b}}{\rho_{11b}\,\gamma_{22b}} .$$

However, the actual quantities employed are derived from the measured values, that is,

$$\varepsilon''_{21} = \frac{\langle\varepsilon'_{21}\rangle}{\langle\rho_{11}\rangle\langle\gamma_{11}\rangle} \text{ and } \pi''_{21} = \frac{\langle\pi'_{21}\rangle}{\langle\rho_{11}\rangle\langle\gamma_{11}\rangle} .$$

As pointed out in Tsai I, one of the salient features of these models is the breaking of the tensor symmetry of the coefficients so that $\langle\rho_{11}\rangle \neq \langle\rho_{22}\rangle$. Then applying (4) we obtain

$$Z_{eff}(\varepsilon') = \frac{P_1}{P_2} Z_{eff} \text{ and } Z_{eff}(\pi') = Z_{eff}. \qquad (36)$$

If we take $P_1^{-1} = \langle\rho_{11}\rangle/\rho_{11b}$ and regard $P_2 \approx 1$, we then find, as shown in Fig. 2, that $\langle\rho_{11}\rangle/\rho_{11b}\, Z_{eff}(\varepsilon')$ for sample C does agree with $Z_{eff}(\pi')$ (Unfortunately, P_1 is

known only for sample C). However, the matter does not end there, as recent investigations of thermal conduction (will be discussed later) cast doubt on the validity of the assumption, $\langle \gamma_{11} \rangle = \langle \gamma_{22} \rangle$. These two quantities are equal for bulk samples, but differences could arise because of the shape and size of the sample. In the case at hand, the cross section for longitudinal heat flow (i.e., γ_{11}) is very much smaller than for transverse heat flow (i.e., γ_{22}). Therefore, even if only the simple Casimir size effect is considered, we could still expect $\gamma_{11} > \gamma_{22}$. Therefore we should revise (36) to

$$Z_{eff}(\pi') = \frac{\langle \gamma_{22} \rangle}{\langle \gamma_{11} \rangle} Z_{eff}.$$

It is not unreasonable to expect that $\langle \gamma_{22} \rangle / \langle \gamma_{11} \rangle \approx 0.9$, which would be necessary to bring all the data - transport as well as specific heat - into rough agreement. However, the precision of the determination of θ_4^* is poor. A value of 35 K is significantly smaller than the value $\theta_4^* = 41$ K which is obtained from (35) if one employs the very reasonable value $\theta_e^* = 28.1$ K for the electron pocket scattering temperature.

E - Conclusion

Antimony has been shown to be an excellent material in which drag phenomena in its varied manifestation may be studied. Strong mutual drag dominates the ideal resistivity

(Tsai III) and the high field magnetoresistivity (Tsai II), while only strong simple drag need be considered in the Ettingshausen and Nernst-Ettingshausen effects. However, the role of drag in the zero field thermoelectric effect must be viewed as a superposition of the two strong drag effects. The total TEP is regarded as arising from three terms of nearly equal importance:

1. The simple carrier diffusion term which varies directly as T with a constant of proportionality closely matching the theoretically expected value.

2. The simple drag term which itself is sum of phonon drag currents in three distinct regions of q-space. That is, there are separately three phonon currents from those phonons: (a) which are dragged only by holes, (b) only by electrons and (c) competitively by holes and electrons. It is only this term which can give rise to the observed minimum in the temperature dependence of the TEP.

3. The mutual drag term arises because of the mutual interaction of carriers and phonons. In the limit of strong drag, this term takes a relatively simple form which can be interpreted with the following picture. The carriers and the phonons which interact with them reach to some mean velocity where the whole system drifts with. The resulting heat current is simply proportional to the specific heat of the whole system times this velocity. Our confidence in this overall picture is heightened when we note that the

values for this velocity term calculated from an admittedly crude model and that determined by fitting the data differ by about 30%, but more importantly, the temperature dependence, which is far more critical to the data fitting, exhibits the form which is appropriate for this fitting.

Because of the complexity of the expression describing $\varepsilon_{11}(0)$, we should not expect to use this measured quantity to precisely determine the relevant parameters. However, when the parameters employed for fitting the $\varepsilon_{11}(0)$ data are obtained from other experiments and theoretical considerations, we find a remarkably close agreement between our model and experiment.

The Ettingshausen and Nernst-Ettingshausen effects exhibited, as expected, evidence for strong carrier drag, wherein the holes and electrons drift together transverse to the directions of the applied electric and magnetic fields and carry with them those phonons with which they interact. The investigation of these effects presents a tool for the determination of the density of states as well as a means for studying such details of the carrier-phonon interaction as the role of different phonon branches and the anisotropy of the interactions. However, the analysis of the data reveals a complication arising from the presence of surface currents as well as anisotropy of lattice thermal conductivity brought about size and shape effects. While, on the one hand, the surface problem complicates the process of

obtaining reliable values for the density of states, on the other hand, these two effects may be used to obtain information on size effect and surface currents. Finally, another matter left unresolved is the rather large value of θ_D obtained from these two transport properties. This could be a consequence of the more prominent role played by longitudinal phonons in the drag phenomena.

CHAPTER II

STUDY OF SURFACE CURRENT AND SIZE EFFECT IN MAGNETORESISTANCE OF ANTIMONY SINGLE CRYSTAL, IN CORBINO GEOMETRY AT LOW TEMPERATURE AND HIGH MAGNETIC FIELD

A - Introduction

Effect of surface current on the transverse magnetoresistance of antimony has been studied by several investigators.[12-16] A wide range of study has been done recently by Tsai, et al., in a rod geometry. This effect has been investigated by studying the behavior of magnetoresistance at different magnetic fields, where the expected quadratic dependence on magnetic field is replaced by an H^{α} dependence where $\alpha < 2$. The effect of a damaged layer in magnetoresistance has been described by regarding the specimen as two parallel conductors with different transport properties. The scattering of the charge carriers at the surface and in the adjacent damaged layer is rather different from the bulk in the amount of intra- and intervalley scattering. Existence of different carrier distribution on the surface from the bulk, builds up another layer, the "diffusion layer," parallel to the surface in which the distribution of the carriers varies from the bulk value to its value on the surface. Thickness of this layer depends on the type of scattering in the bulk and in the damaged layer or at the surface, and specially on the direction of both magnetic and electric fields. In the case that the surface is parallel

to the electric and magnetic fields, both electrons and holes have the same transverse drift velocity (Hall velocity) so that the hole-electron pairs are created on one surface drift across the sample and recombine on the other surface through interband scattering. Such a state of affairs has been recognized as a major factor in "diffusion size effect" observed in bismuth.[17]

Considering a rod sample with a rectangular cross section, one can remove the damaged layers on surfaces almost completely by chemical etching and electropolishing. The removal of these layers will eliminate surface currents on the faces normal to the magnetic field. The damaged layer currents on the other two faces also will disappear, but currents arising from diffusion of carriers within an effective thickness might discernibly alter the measured transport coefficients from their bulk values. In Corbino geometry with the magnetic field perpendicular to the surface of the disk, the lateral surfaces parallel to the field is eliminated so that the current due to the diffusion of carriers will disappear; therefore, in an electropolished sample with circular geometry a larger contribution of the bulk properties in transport coefficient measurement is expected.

It is also interesting to note that, while rod geometry is a perfect geometry for adiabatic magnetoresistance measurement, ρ_{11}^{a}, Corbino geometry is an appropriate geometry for direct isothermal magnetoresistance measurement.

B - Experimental Details

The rod and disk monocrystalline samples were cut by a Servomet spark cutter from the same pure antimony ingot. The rod sample has dimensions 18 x 3 x 3 mm with the long dimension, that is, the current direction, parallel to the bisectrix axis which is denoted as the x direction. The lateral faces are perpendicular to the binary axis, y, and to the trigonal axis, z, which is always the direction of the applied magnetic field. With this choice of crystallographic orientation, the bulk resistivity and thermoelectric, Peltier, and the thermal conductivity tensors are reduced to relatively simple forms.

Disk sample No. 1, with a radius of 6 mm and with the trigonal axis perpendicular to the surface of the disk, was cut by a 1/2" stainless steel tube mounted on the spark cutter. In order to get a uniform current distribution in the sample, a 0.035" hypodermic needle was used to make a hole through the center of the disk within which a copper wire was soldered. This antimony sample, with an original thickness of 8.10 mm, was utilized in the study of the effect of different surface treatments on the magnetoresistance. Because of these treatments, the sample (No. 1) thickness varied from 8.10 to 7.50 mm. To analyze the effect of the thickness on the magnetoresistance, sample No. 1 then was cut into two parts (samples 2 and 3); sample No. 2, was 2 mm thick and sample No. 3 had a thickness of 3.8 mm. For this

analysis sample No. 2 ranged in thickness from 2.0 to 1.15 mm. In the final experiment to study the effect of a broken circular symmetry on the magnetoresistance, a radial slot was made in this sample (No. 2). Sample No. 3 was used to study the thickness effect and lattice thermal conduction in the Corbino geometry.

To examine the "peeling effect", Tsai's rod sample No. 5 was cut such that the surfaces made an angle of about 7° with the basal plane. The dimensions of the sample after cutting were about 1.6 x 3.3 x 25 mm.

For more accuracy in the geometric factor measurement and for a completely circular equipotential in the disk, another sample (No. 4) with a small boss at the center was cut by a 1/2" stainless steel rod with a 6 mm diameter hole at the center soldered inside the cutting tube. After cutting, the sample measured 1.7 mm thick and the boss had a height of 1.5 mm and a diameter of 4 mm.

After spark cutting, all the samples (except the one which was cleaved) were lapped by No. 600 emery paper and chemically etched with aquaregia or HF + $C_3H_5(OH)_3$ + H_2O for about 3 to 5 minutes. The samples were electropolished using a basic solution (KOH + $C_3H_5(OH)_3$ + H_2O) with an electric current about 100 ma for 30 minutes.

In a set of measurements where only magnetoresistance was under investigation, the samples (rod and disk) were simply soldered to a brass sample holder which was screwed

to the copper heat sink. In another set of experiments on the rod sample where the electrical and thermal measurements were performed simultaneously, the sample was soldered on one side to the main heater and on the other side to the auxiliary heater. The sample holder, which was soldered to the auxiliary heater, was screwed tight and then soldered to the heat sink (Fig. 3). In similar experiments in the Corbino geometry, the main heater, a resistance wire, was wound around the sample which then was soldered to the sample holder (Fig. 4). All the leads were soldered with 60/40 Bi-Cd eutectic. The potential difference measurements were made with a Rubicon potentiometer using a 147 Keithley nanovoltmeter as the null detector, and the electric current was measured by a K-3 Universal Potentiometer.

C - Transport Coefficients

In order to obtain the relationships between transport coefficients in the Corbino and rod geometries, one can start with the general transport equations which were given in Chapter I (Eqs. (1), (2) and (3)).

The different transport tensors are the electrical conductivity σ and resistivities $\hat{\rho}$; $\hat{\rho}^a$, the thermoelectric ε, ε', ε''; the Peltier π, π', π''; the thermal conductivities λ'', λ, and resistivity, γ. With the field H applied in the direction of the trigonal axis, z, these tensors are expected, by crystal symmetry, to have the form

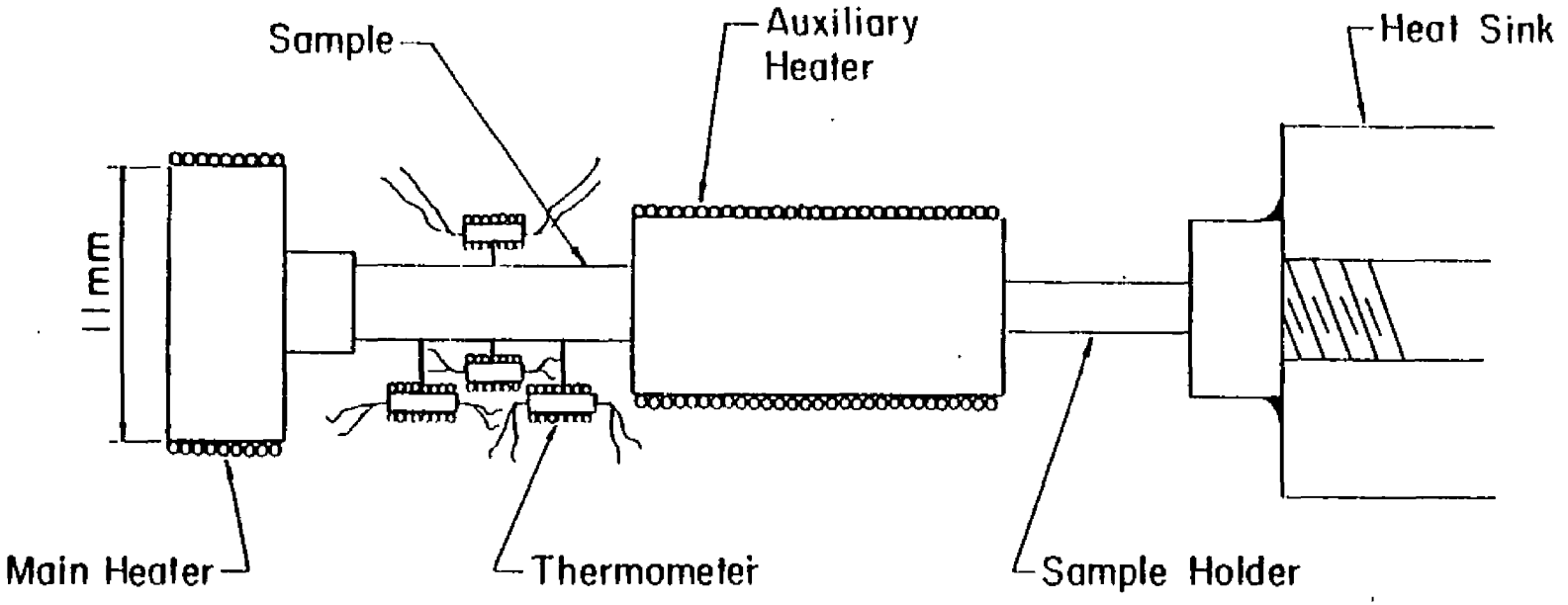
Sample
Auxiliary Heater
Heat Sink
11mm
Main Heater
Thermometer
Sample Holder

Fig. 3

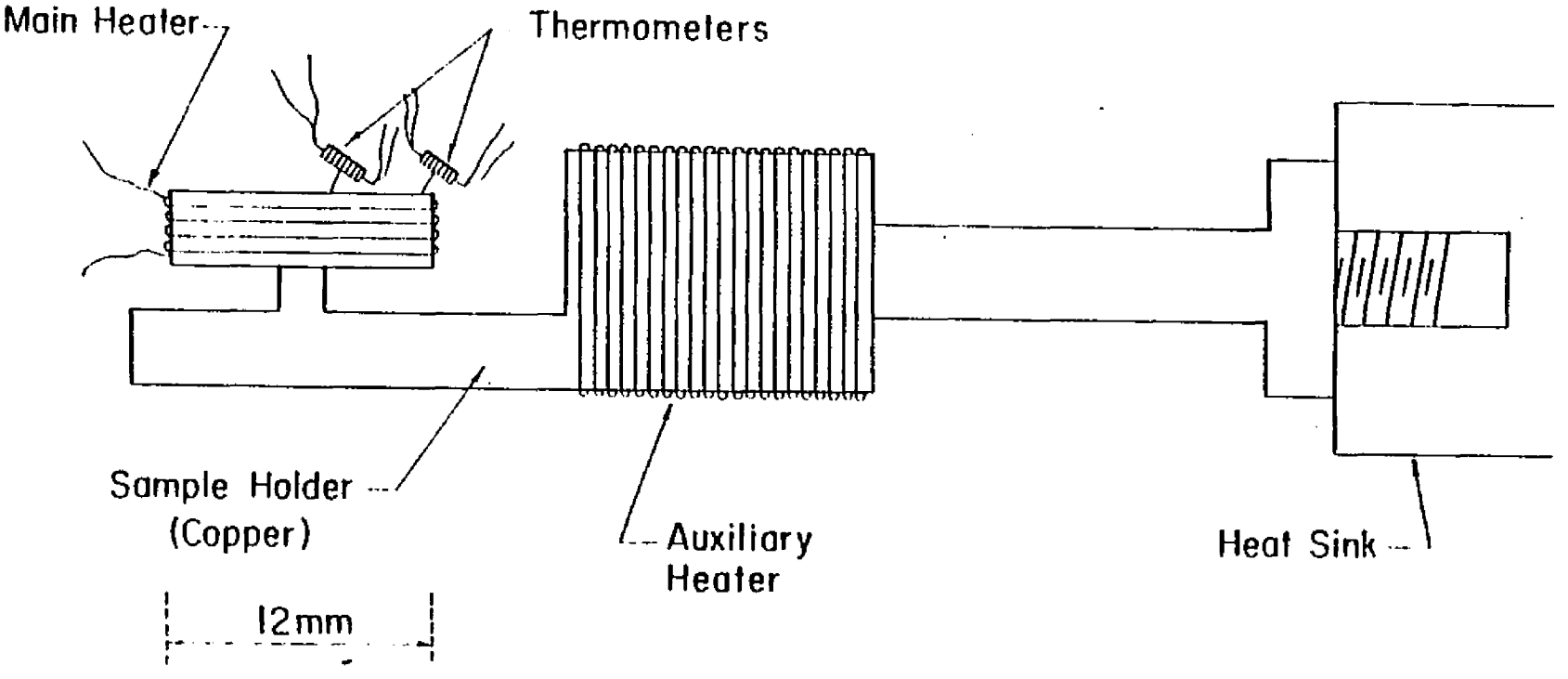
Main Heater
Thermometers
Sample Holder
(Copper)
12mm
Auxiliary
Heater
Heat Sink

Fig. 4

$$a = \begin{bmatrix} a_{11} & a_{12} & 0 \\ -a_{12} & a_{11} & 0 \\ 0 & 0 & a_{33} \end{bmatrix} \tag{37a}$$

and to have the following symmetries relative to the magnetic field

$$a_{12}(H) = a_{21}(-H) = -a_{21}(H),\ a_{11}(H) = a_{11}(-H). \tag{37b}$$

Further simplifications at very high field are expected: ε'_{11} is negligible with respect to ε'_{21} and this is also true in the tensors $\hat{\varepsilon}$, $\hat{\varepsilon}''$, $\hat{\pi}$, $\hat{\pi}'$, and $\hat{\pi}''$. ρ_{21} is negligible relative to ρ_{11} so that for most practical matters, the tensor is diagonal and also this is the case for the tensors $\hat{\sigma}$, $\hat{\rho}^a$, $\hat{\lambda}$, $\hat{\lambda}''$, and $\hat{\gamma}$. It may be pointed out that electrical and thermal conduction along the field, z direction, remains at nearly their zero-field value, while decreasing several orders of magnitude along the x and y direction, perpendicular to the field, with $\sigma_{33} >> \sigma_{11}$ as $\sigma_{11} \propto H^{-2}$ and $\lambda_{33} >> \lambda_{11}$ as $\lambda_{11} \to \lambda_g$, the lattice conduction. Corresponding relations will apply to the respective coefficients in $\hat{\lambda}''$, $\hat{\rho}$, $\hat{\rho}''$ and γ. At 20 KG, $\sigma_{11} \simeq 10^{-5}\sigma_{33}$ and at T = 2°K, $\lambda_g < 10^{-2}\lambda_{33}$.

Using the symmetry which is involved and simplification brought about by deletion of negligible terms, one can derive interesting relations between the coefficients. Some of the relations of interest are:

$$\sigma_{11} = (\rho^{-1})_{11} \simeq \rho_{11}^{-1} \qquad \lambda_{11} = \lambda_g = (\gamma^{-1})_{11} \simeq \gamma_{11}^{-1} \tag{38a}$$

$$\varepsilon'_{21} \simeq \rho_{22}\varepsilon''_{21}\gamma_{11} \qquad \pi'_{21} \simeq \gamma_{22}\pi''_{21}\rho_{11} \tag{38b}$$

and

$$\lambda''_{11} = \lambda_{11} - \frac{\varepsilon_{12}\pi_{12}}{\rho_{11}} \tag{38c}$$

$$\rho_{11} - \rho^{a}_{11} = -(\hat{\varepsilon}\hat{\pi}')_{11} = -(\hat{\varepsilon}'\hat{\lambda}\hat{\pi}')_{11} \simeq -\varepsilon'_{12}\lambda_{22}\pi'_{21} \simeq \varepsilon'_{21}\lambda_{g}\pi'_{21}. \tag{39}$$

Bridgmann's relation,[18] $\pi_{21}(-H) = T\varepsilon_{12}(H)$, yields

$$\pi'_{21} = T\varepsilon'_{21}. \tag{40}$$

By using the second form of the transport equation, one can write

$$E_x = \rho_{11}J_x + \rho_{12}J_y - \varepsilon_{11}\nabla_x T - \varepsilon_{12}\nabla_y T \tag{41}$$

$$E_y = -\rho_{12}J_x + \rho_{11}J_y + \varepsilon_{12}\nabla_x T - \varepsilon_{11}\nabla_y T \tag{42}$$

and

$$W_x = -\pi_{11}J_x - \pi_{12}J_y - \lambda_{11}\nabla_x T - \lambda_{12}\nabla_y T \tag{43}$$

$$W_y = \pi_{12}J_x - \pi_{11}J_y + \lambda_{12}\nabla_x T - \lambda_{11}\nabla_y T. \tag{44}$$

Considering E_r, E_θ and W_r, W_θ as the electrostatic potential and heat current components in cylindrical coordinates, one can write

$$\begin{aligned} E_r &= E_x\cos\theta + E_y\sin\theta \\ E_\theta &= -E_x\sin\theta + E_y\cos\theta \end{aligned} \tag{45}$$

and similar equations for W_r and W_θ, where θ is the angle between E_r and x-axis. Substituting Eqs.(41) and (42) in Eq. (45), we obtain

$$E_r = \rho_{11}J_r + \rho_{12}J_\theta - \varepsilon_{11}\nabla_r T - \varepsilon_{12}\nabla_\theta T \tag{46}$$

$$E_\theta = -\rho_{12}J_r + \rho_{11}J_\theta + \varepsilon_{12}\nabla_r T - \varepsilon_{11}\nabla_\theta T, \tag{47}$$

similarly

$$W_r = -\pi_{11}J_r - \pi_{12}J_\theta - \lambda_{11}\nabla_r T - \lambda_{12}\nabla_\theta T \tag{48}$$

$$W_\theta = \pi_{12}J_r - \pi_{11}J_\theta + \lambda_{12}\nabla_r T - \lambda_{11}\nabla_\theta T, \tag{49}$$

where similar definitions for J_r and J_θ have been considered. The circular symmetry in Corbino geometry implies that

$$\nabla_\theta T = E_\theta = 0.$$

Applying these conditions in Eqs. (46) and (47), we obtain

$$0 = -\rho_{12}J_r + \rho_{11}J_\theta + \varepsilon_{12}\nabla_r T \tag{50}$$

$$E_r = \rho_{11}J_r + \rho_{12}J_\theta - \varepsilon_{11}\nabla_r T \tag{51}$$

which yields

$$E_r = (\rho_{11} + \frac{\rho_{12}^2}{\rho_{11}})J_r - (\varepsilon_{11} + \frac{\rho_{12}}{\rho_{11}}\varepsilon_{12})\nabla_r T. \tag{52}$$

Since $\rho_{12} << \rho_{11}$ and $\nabla_r T$, which is the temperature gradient due to the self heating, is also small (Appendix B) with a good approximation, one can write

$$E_r \simeq \rho_{11}J_r \qquad\qquad \rho_{disk} = \frac{E_r}{J_r} \simeq \rho_{11}. \tag{53}$$

Therefore, for the sample in vacuum or submerged in liquid helium, magnetoresistance measurement in Corbino geometry always gives the isothermal magnetoresistance,

Having $\nabla_\theta T = 0$ in Eq. (48), we obtain

$$W_r = -\pi_{11}J_r - \pi_{12}J_\theta - \lambda_{11}\nabla_r T. \tag{54}$$

Using Eq. (50), one can write

$$J_\theta = \frac{\rho_{12} J_r - \varepsilon_{12} \nabla_r T}{\rho_{11}} .$$

In thermal conductivity measurement where $J_r = 0$, Eqs. (54) and (50) will lead us to

$$W_r = -(-\frac{\pi_{12}\varepsilon_{12}}{\rho_{11}} + \lambda_{11})\nabla_r T \tag{51}$$

or

$$\lambda_{disk} = \lambda_{11} - \frac{\pi_{12}\varepsilon_{12}}{\rho_{11}} \tag{52}$$

where $\lambda_{disk} = -\frac{W_r}{\nabla_r T}$ is the lattice thermal conductivity measured in Corbino geometry.

Comparing Eq. (52) with (38c), we obtain

$$\lambda_{disk} = \lambda''_{11}. \tag{53}$$

Similarly, by using the first form of the transport equation, one obtains

$$\rho_{disk} = (\sigma_{11})^{-1} \quad (\nabla_r T = 0) \tag{54}$$

and

$$\lambda_{disk} = \lambda''_{11} - \frac{\pi''_{11}\varepsilon''_{11}}{\sigma_{11}} . \tag{55}$$

D - Effect of Surface Layer on the Bulk Transport Coefficients

Transport coefficients of antimony at low temperature is known to be affected by the condition of the surface. In order to study this effect, Tsai, et al., introduced two different models for different conditions of the surface.

In the first model, "layer model", a rod sample with damaged surface layers which has the following properties has been considered.

a) The layer transport properties are identical with those of the bulk, except for larger scattering frequencies in the layers.

b) The thickness of the layer, δ, is large enough so that uniform transport tensors can be defined for the layer with the same symmetries as in Eq. (37a) and (37b), but small enough relative to d, the sample cross-section size, to allow the model to be limited to the first order in δ/d.

c) The scattering frequency in the layer is much larger than that in the bulk, but small enough so that the asymptotic high-field condition is satisfied also.

d) The length of the sample in the x direction is large so that the end surfaces may be disregarded. Under the above assumptions the relations between the effective and bulk coefficients have been obtained (Eq. (4) in Chapter I). The parameters, P_1 and P_2, which have been introduced in these equations depend on the thickness and conductivity of the surface layer, and they have been given by

$$P_1 \simeq 1 + \frac{2\delta_y}{d} \frac{\sigma_{11sy}}{\sigma_{11}} + \frac{2\delta_2}{d} \frac{\sigma_{11sz}}{\sigma_{11}} \tag{56a}$$

$$P_2 \simeq 1 + \frac{2\delta_z}{d} \frac{\sigma_{11sz}}{\sigma_{11}} \quad , \tag{56b}$$

where δ_y and δ_z are the thicknesses of layers normal to the

y and z axes, respectively, while σ_{11sy} and σ_{11sz} are the conductivities of these layers.

It is interesting to note that this model preserves the Bridgmann relation since

$$\frac{\langle \pi'_{21} \rangle}{T\langle \varepsilon'_{12} \rangle} = \frac{\pi'_{21}}{T\varepsilon'_{12}} . \tag{57a}$$

But the tensor symmetry is broken since

$$\frac{\langle \varepsilon'_{12} \rangle}{\varepsilon'_{21}} \simeq \frac{\langle \pi'_{21} \rangle}{\pi'_{12}} \simeq \frac{\langle \rho_{22} \rangle}{\rho_{11}} = \frac{P_1}{P_2} . \tag{57b}$$

For the difference between isothermal and adiabatic resistivities one obtains

$$\langle \rho_{11} \rangle - \langle \rho^a_{11} \rangle \simeq \langle \varepsilon'_{21} \rangle \lambda_g \langle \pi'_{21} \rangle \frac{P_2}{P_1} . \tag{58}$$

In Corbino geometry, where the diffusion layer is negligible, and the transport properties are mainly affected by the presence of a damaged layer on the surface, the layer model will be suited for describing the relation between the bulk and measured transport properties of the sample. Considering damaged layer model for the sample under consideration, one obtains (Appendix B)

$$\frac{\rho_{11}}{\langle \rho_{disk} \rangle} \simeq 1 + \frac{2\delta_z}{t} \frac{\sigma_{11sz}}{\sigma_{11}} \tag{59}$$

where t is the thickness of the disk and $\langle \rho_{disk} \rangle$ is the magnetoresistance measured in this geometry.

In the second model, "skin model", a rod sample without damaged surface layers has been considered. With this

condition only currents arising from diffusion of the carriers within an effective thickness might discernibly alter the measured transport coefficients from their bulk values. Although this model could be achieved by setting $P_2 = 1$ in the formulas derived in the layer model, it is doubtful that the layer model could describe a diffusion layer condition. Since our experimental results, especially in Corbino geometry, fall into the first category, the theoretical derivation for the skin model will not be presented here.

E - Experimental Procedure

The experiment was performed in the helium temperature range (1.1°K to 4.2°K) and magnetic field up to 20 KG. The magnetic field was always applied in the trigonal, z, direction.

The techniques of the measurement are similar to those used in preceding work. Electrical noise was reduced reasonably by electromagnetic shielding of the wires from the cryostat to the potentiometer.

In order to have uniform current distribution through the disk, a hole was made at the center of the disk and a copper wire was passed through the hole and soldered to the sample. One of the current leads was soldered to this wire and the other was soldered to another copper wire which had already been wound around and soldered to the periphery of the sample.

The electrical currents sufficient to give a measured radial potential difference of $\sim 200\mu$ were usually 20 to 50 mA depending on the magnetic field and the thickness of the sample.

In most of the measurements the sample was in contact with the liquid He bath. The measurements in vacuum were performed when the sample had been set up for thermal measurements.

F - Results and Discussion

The first set of experiments on Corbino geometry was to investigate the effect of circular symmetry of the sample on the magnetoresistance measurement. Therefore, the temperature dependence of the magnetoresistance of the sample was measured at 8 KG in two different cases, in contact with a liquid He bath and in a vacuum. This experiment was repeated at 20 KG. The experimental results are shown in Figs. 5 and 6. As it was expected, the results showed neither a jump at λ point nor a difference in the magnetoresistance measurement in either case, i.e., in contact with the liquid bath or in a vacuum chamber, which is in complete agreement with the theoretical result, Eq. (53). It is also interesting to note that the isothermal magnetoresistance smoothly increases as temperature decreases and becomes practically constant below 2°K, and certainly does not show any decrease below this temperature. This is the

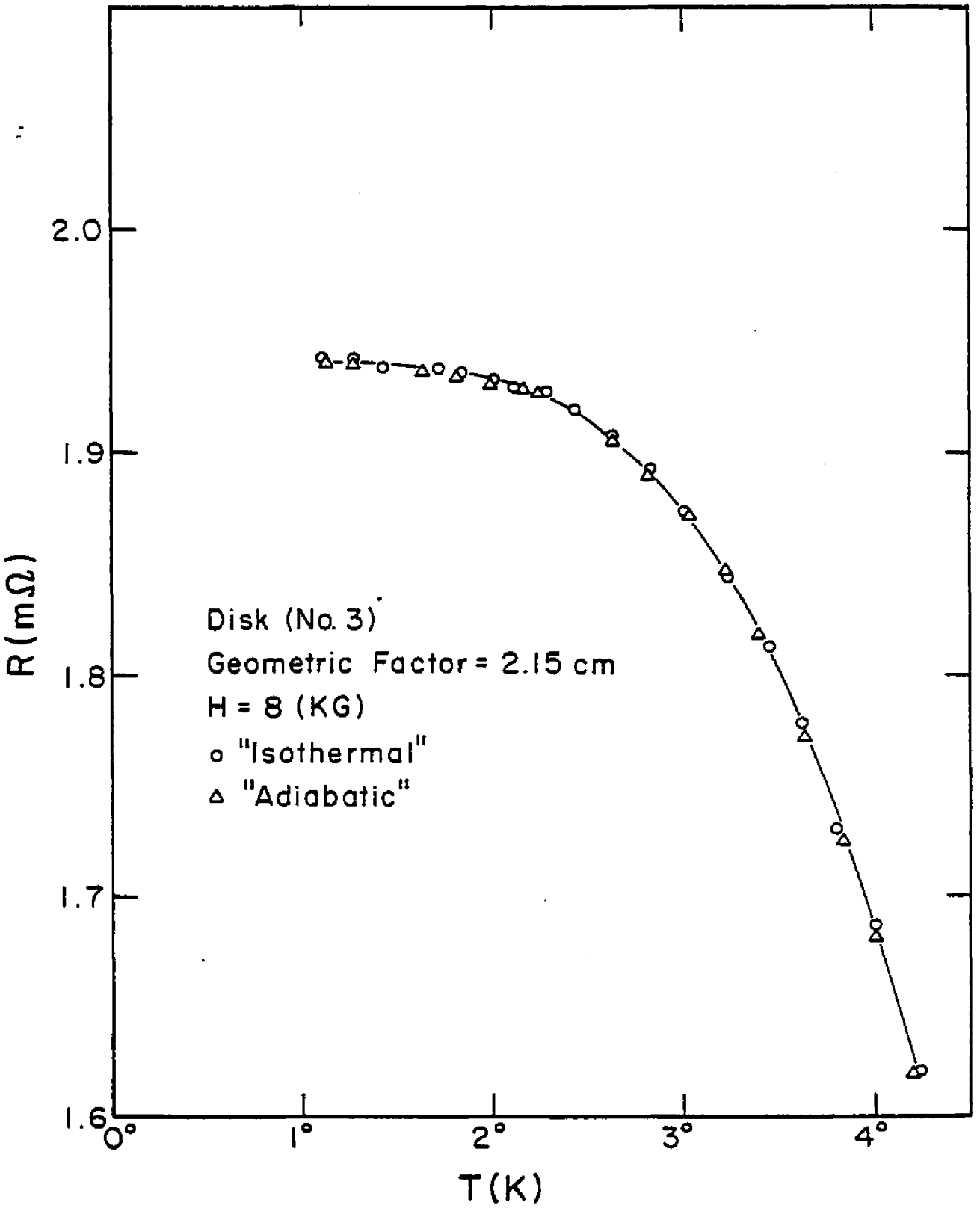
2.0
1.9
1.8
1.7
1.6
R(mΩ)
Disk (No. 3)
Geometric Factor = 2.15 cm
H = 8 (KG)
o "Isothermal"
Δ "Adiabatic"
0°
1°
2°
3°
4°
T(K)

Fig. 5

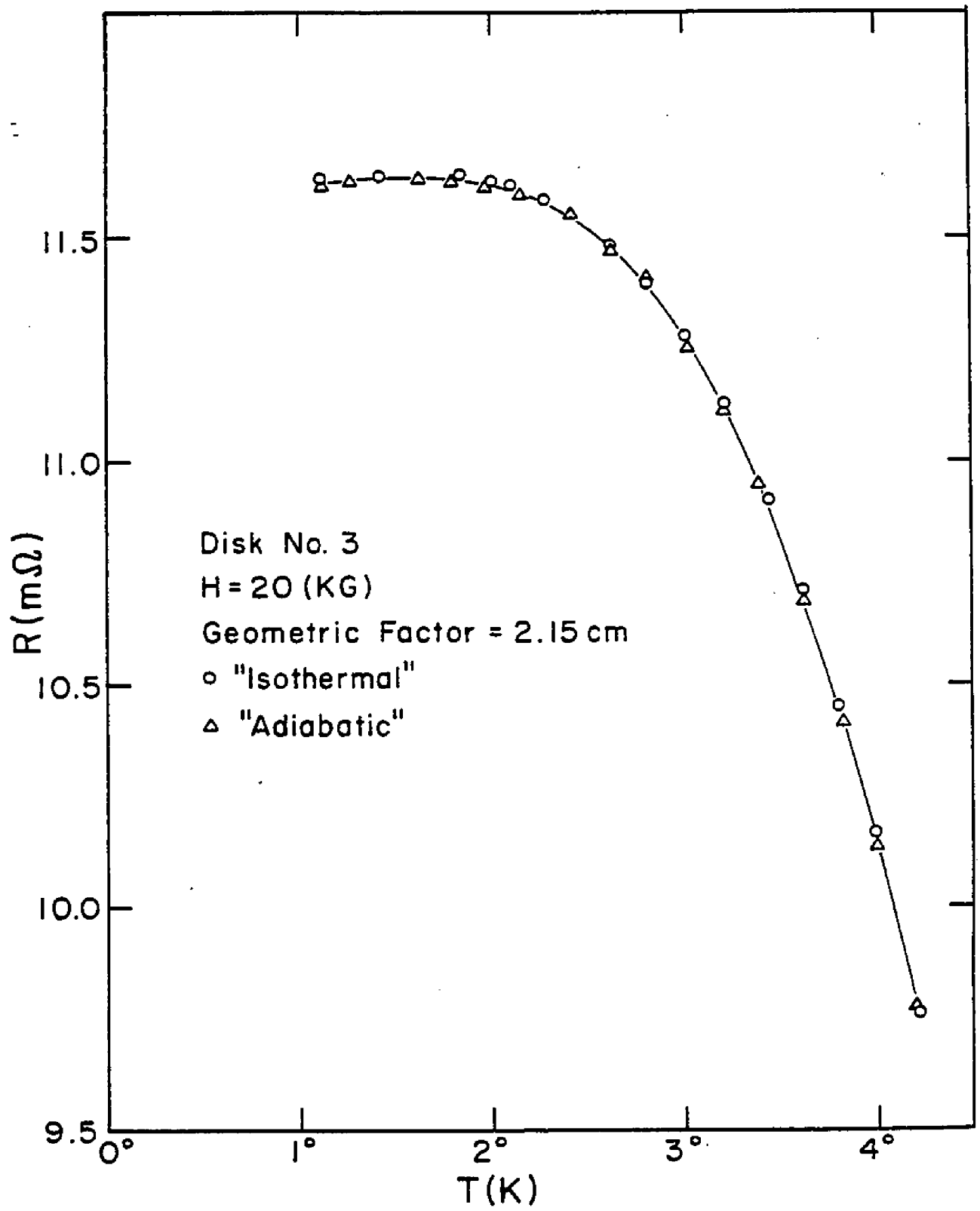
11.5
11.0
10.5
10.0
9.5
R(mΩ)
Disk No. 3
H = 20 (KG)
Geometric Factor = 2.15 cm
o "Isothermal"
Δ "Adiabatic"
0°
1°
2°
3°
4°
T(K)

Fig. 6

direct verification of the assumption made by Tsai in the isothermal magnetoresistance investigation.

A similar experiment in a rod geometry was performed. The result, shown in Fig. 14, is consistent with the work done by Tsai, et al.

In the next set of experiments the effect of surface current in the magnetoresistance in this geometry was studied. In agreement with the results of other investigators in a rod geometry, we found that magnetoresistance in the range of 2 to 20 KG can be described as $\rho \sim H^{\alpha}$ where $\alpha<2$. The exponent, α, has its lowest value for the most damaged surfaces and approaches to 1.97 for the electropolished surface.

The average values of α and ρ for samples with different surface treatments are given in Table I. The average values have been obtained by magnetoresistance measurement of the sample using two pairs of potential probes at both sides of the sample. The experimental results in the temperature and magnetic field dependence of the sample with different surface treatments are shown in Figs. 7 and 8.

Before discussing our next results, there is one important point about the accuracy of magnetoresistivity measurement which should be considered. In the magnetoresistivity measurements, the electric current and potential difference in the sample can be measured with a reasonably high accuracy. However, owing to a relatively large uncertainty in the geometric factor measurement in Corbino

Table I

(H = 20 KG)

Thickness $\bar{t}_{mm}$	Surface Treatment	Average Magneto-resistance ρ_o (mΩ-cm)	Average Exponent $\bar{\alpha}$	$\frac{\rho_{T=4.2} - \rho_o}{\rho_o} \times 100$
7.84	lapped	5.3	1.57	%5
8.10	cleaved	14.5	1.83	%8
7.47	etched	17.5	1.92	%18
7.40	electro-polished	21.4	1.96	%20

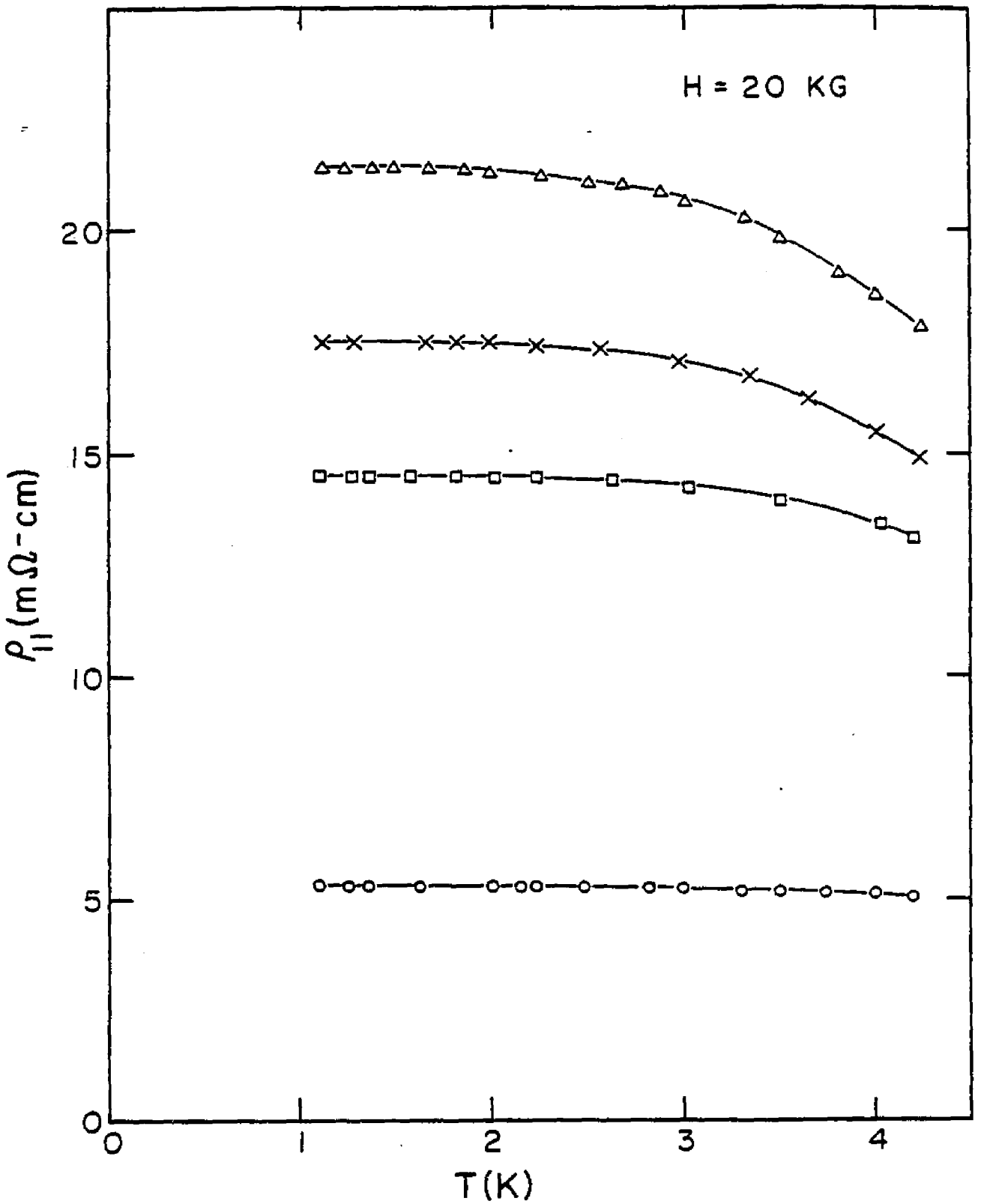

Fig. 7

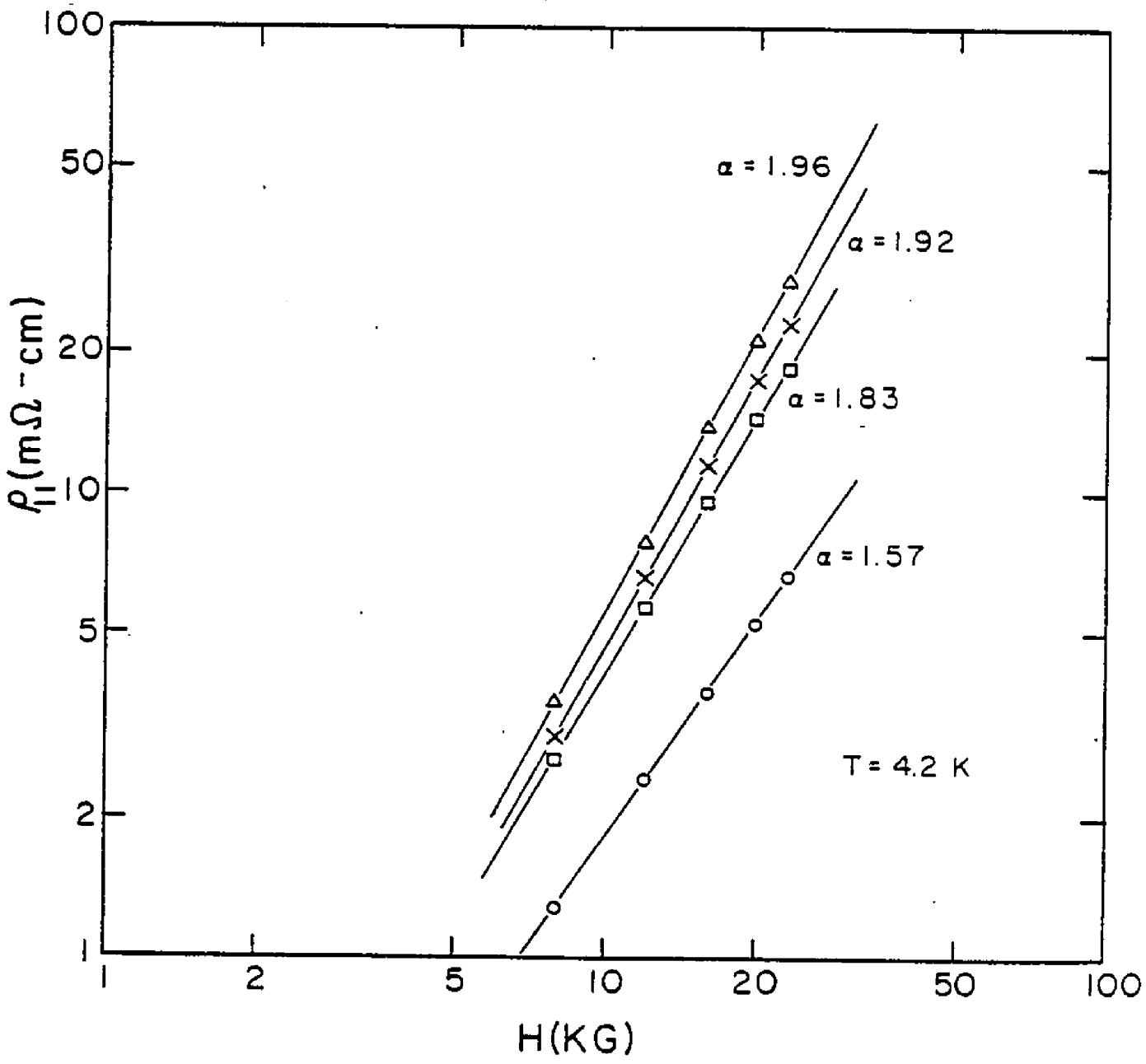
100
50
20
10
5
2
1
ρ_{11}(mΩ-cm)
1
2
5
10
20
50
100
H(KG)
α = 1.96
α = 1.92
α = 1.83
α = 1.57
T = 4.2 K

Fig. 8

geometry, the magnetoresistivity of the sample cannot be obtained as accurately as it is done in the rod geometry. In the Corbino geometry, the geometric factor can be written as

$$G = \frac{2\pi t}{\ell n(\frac{r_1}{r_2})} ,$$

where t is the thickness and r_1 and r_2 are distances of the potential probes from the center of the disk. One can show that an uncertainty of 0.2 mm in determining the center of the disk would yield 10 to 15% error in r_1; consequently, in the geometric factor measurements.

In Fig. 9 the conductivity of the electropolished samples are plotted as a function of 1/t. In order to obtain the bulk conductivity, extrapolation to $1/t = 0$ (i.e. $t \to \infty$) can be made. Even though a large uncertainty is involved in this measurement, some quantitative results can still be extracted from these measurements. a) It is apparent from the results that the concept of surface layer conductance is consistent with the observed size dependence of the magneto-conductivity. b) Size effect in this geometry is smaller than that in a rod geometry. c) The ingot from which our samples were cut has larger magnetoresistance than the one used by Tsai, et al.

In addition to the fundamental investigation mentioned earlier, a set of subsidiary experiments for qualitative study of certain properties was performed. These

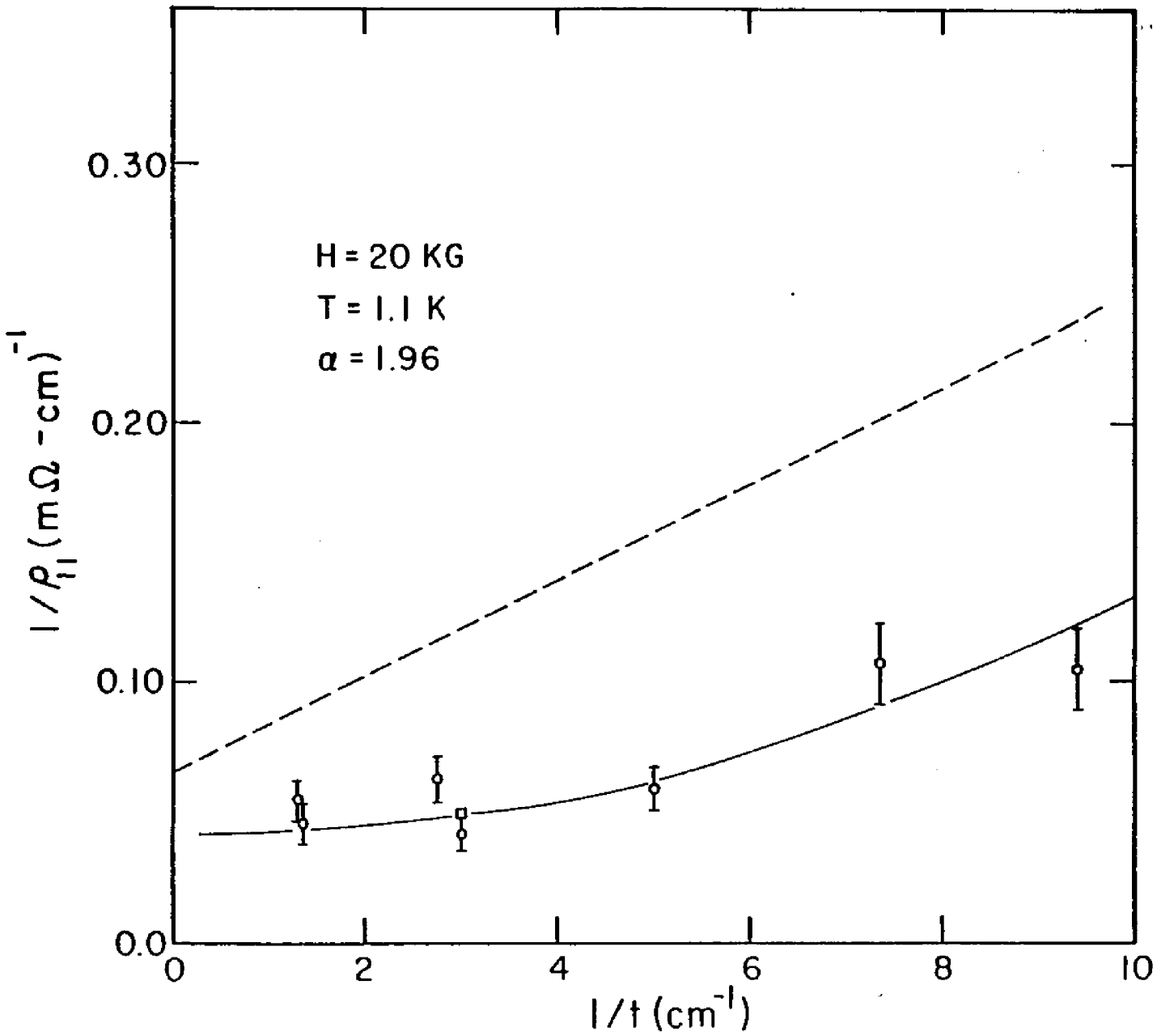

Fig. 9

experiments, which were performed in both disk and rod geometries, will be reported below.

a) As it was mentioned before, the existence of circular symmetry in the Corbino geometry, which yields to zero azimuthal temperature gradient in the sample, makes the isothermal magnetoresistance measurement possible. Therefore, by breaking the symmetry in the sample one expects to observe a similar behavior as one does in a rod geometry where the sample is in contact with the liquid helium, i.e., a jump at λ point where the liquid helium becomes superfluid. In order to break the symmetry and observe this effect a radial slot was cut through the sample. The temperature and magnetic field dependence of the magnetoresistance of the sample are shown in Figs. 10 and 11.

b) Since antimony can be easily cleaved along the basal plane, there is a possibility for the existence of a relatively deep cleavage parallel to this plane adjacent to the surface of the sample. This effect, which may have been caused by the stress on the sample during spark cutting, causes the surface of the sample to appear as separate small layers or flakes on top of each other. Such possibility has been mentioned also by Herrod, Gage and Goodrich[19] in the study of the Fermi surface of antimony. One way to reduce this effect (the peeling effect) is to cut the sample such that the surfaces make some small angle with the basal plane. In order to study the effect, Tsai's rod sample No. 5 was

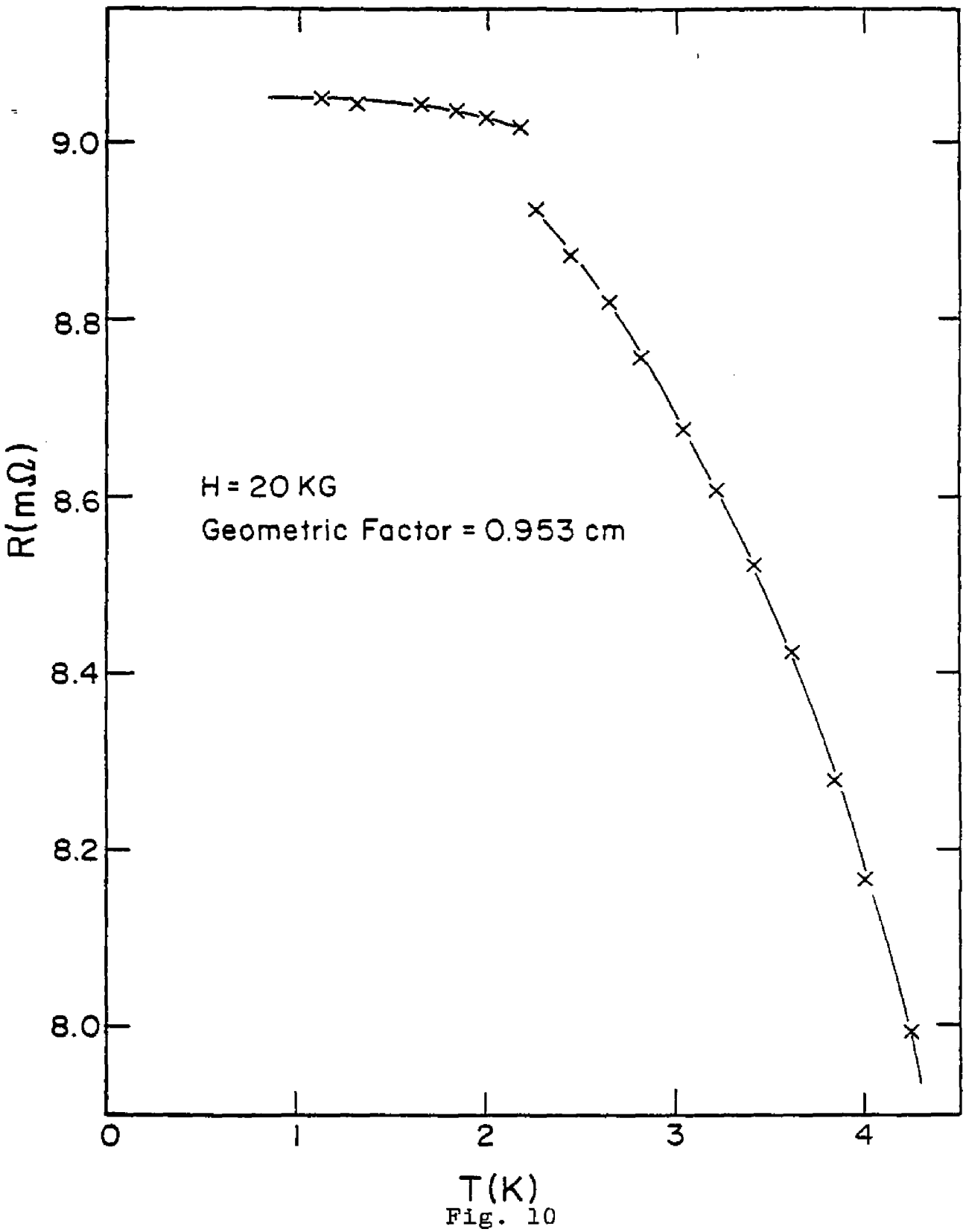

Fig. 10

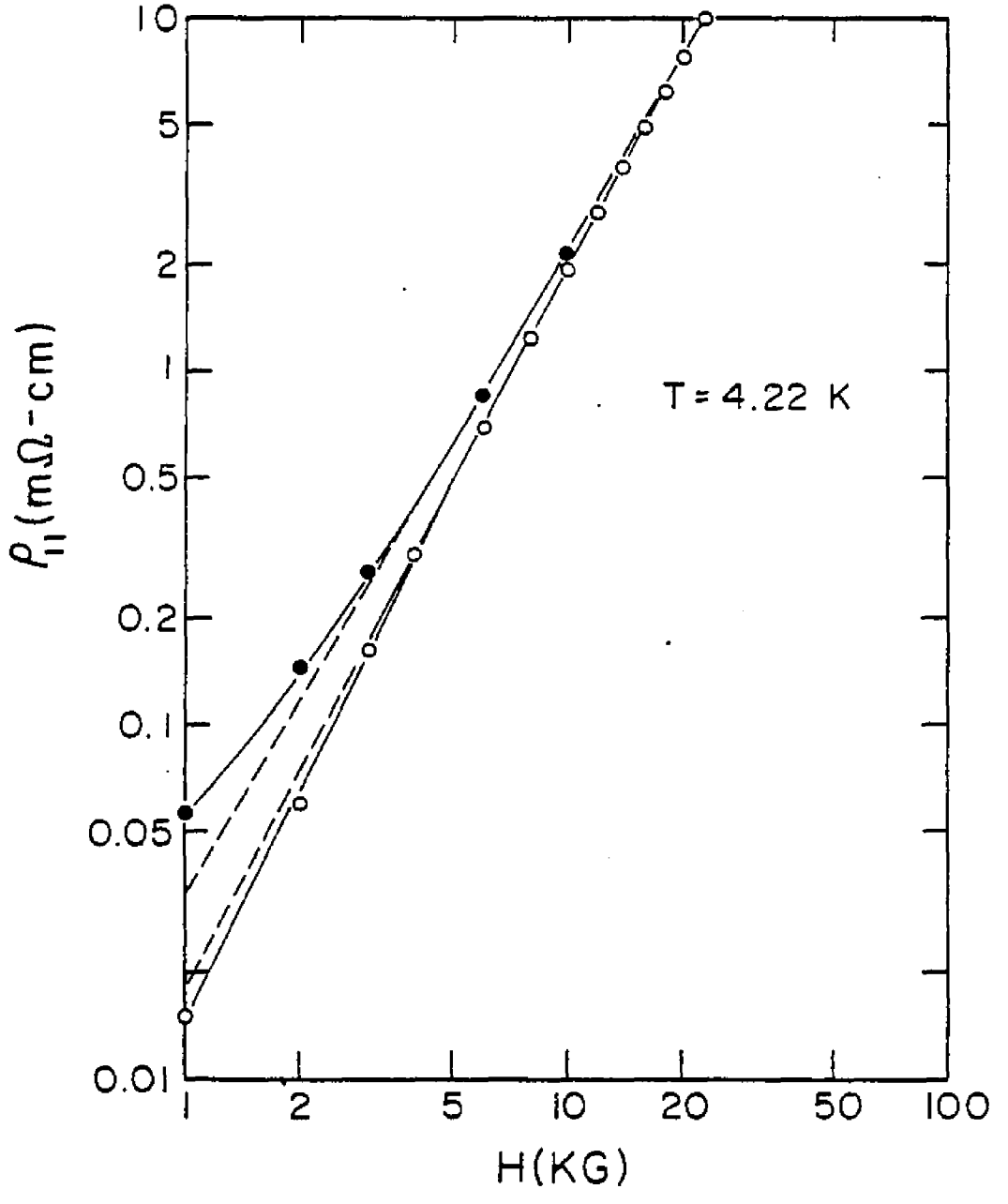

Fig. 11

cut about 7° off from the basal plane. After the cutting, it was etched and electropolished. The experimental results in the temperature and magnetic field dependence of the sample are shown in Figs. 12 and 13. Although a value very close to 2 was obtained for the exponent, α, in the study of the field dependence, but when the magnitude of the magnetoresistivity of the sample was compared to the value which had been obtained by Tsai previously, no noticeable change was observed. This is a pursuing result as it shows "peeling" has some effect on the field dependence and apparently a negligible effect on the surface current

c) One of the problems with magnetoresistance measurement in the Corbino geometry is the possibility of inhomogeneous feeding of the current from the current lead to the disk, which would lead to a noncircular equipotential distribution in the sample and to some uncertainty in the geometric factor measurement. In order to solve this problem, sample No. 6 was cut with a boss at the center of the disk. Although the sample was etched and electropolished after cutting, a relatively small value (1.65) for the exponent, α, and about 4% for the ratio $\frac{\rho(T=0)-\rho(T=4.2)}{\rho(T=0)}$ were obtained. This may have been due to the poor quality of the sample, stress on the sample because of the small thickness and method of preparation, or the "shadow effect" which will be discussed later.

In order to compare the experimental results in Corbino geometry with the rod, magnetoresistance,

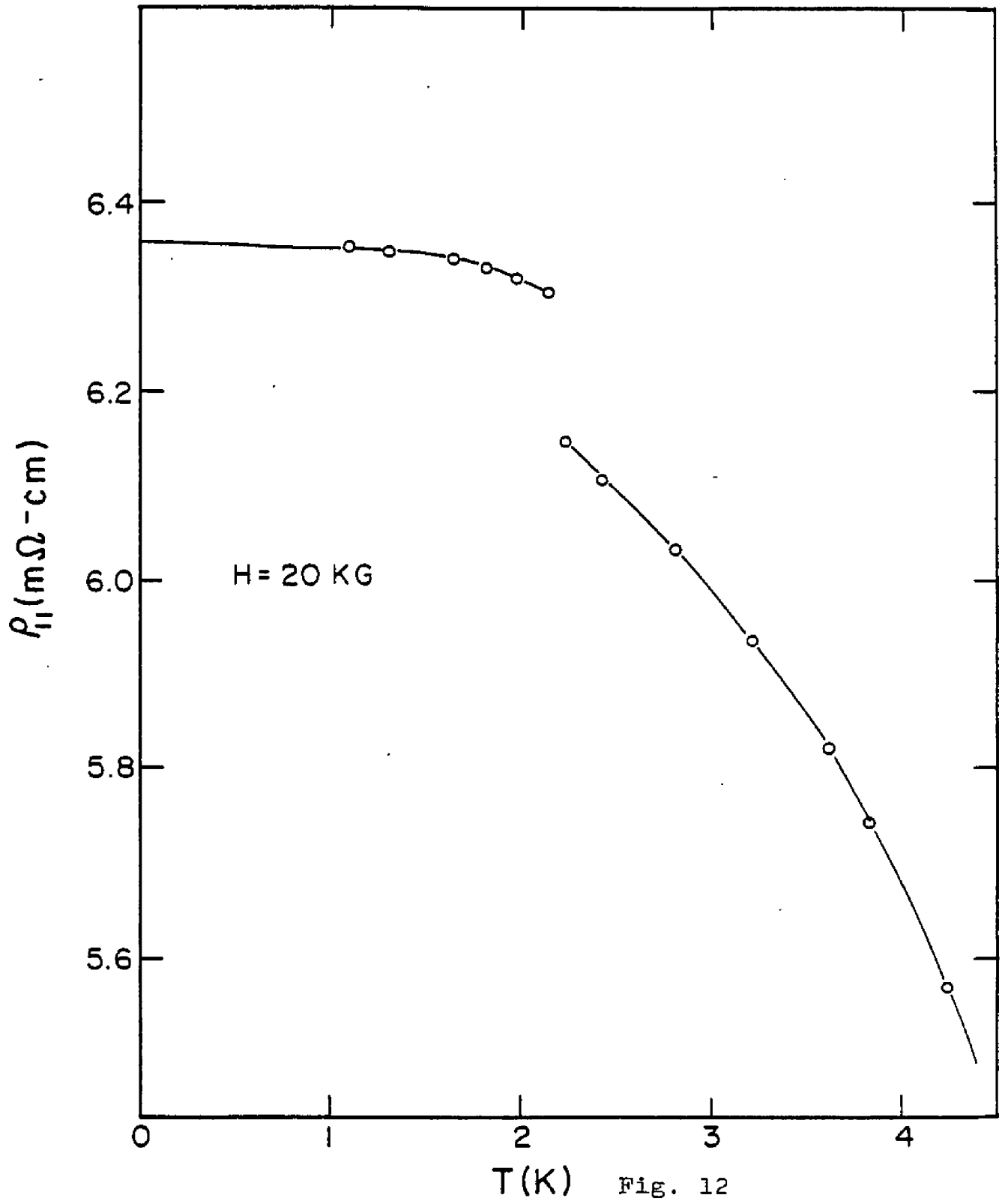

Fig. 12

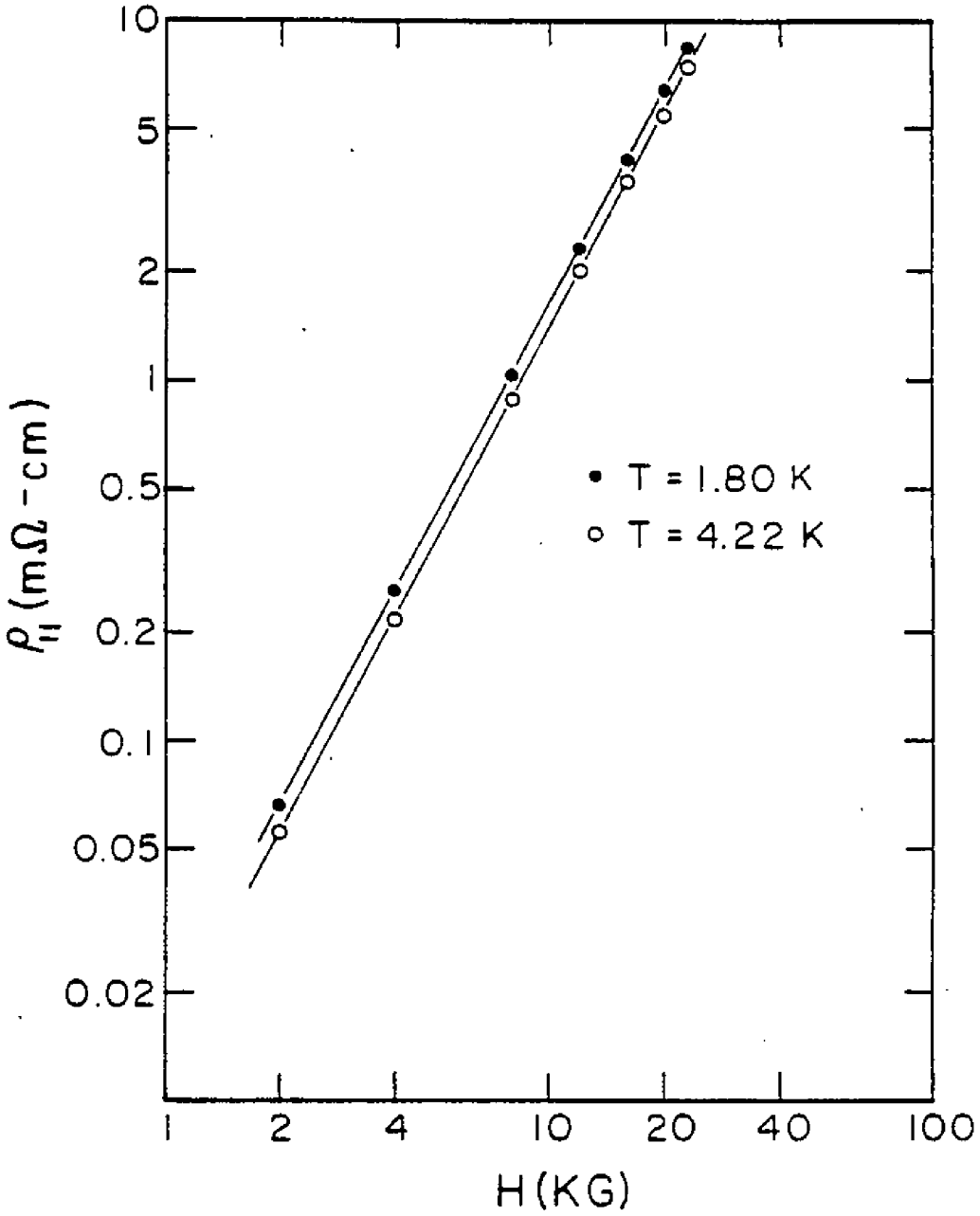
10
5
2
1
0.5
0.2
0.1
0.05
0.02
ρ_{11} (mΩ-cm)
• T = 1.80 K
○ T = 4.22 K
1
2
4
10
20
40
100
H(KG)

Fig. 13

Ettingshausen, Nernst-Ettingshausen and lattice thermal conductivity in the rod sample (sample D), cut from the same ingot, were measured. The temperature dependence of the magnetoresistance at H = 20 KG is shown in Fig. 14 and the experimental results in E-coefficient, N-E coefficients, and the lattice thermal conductivity are shown in Figs. 15, 16, and 17. Although a complete surface treatment had been done on the sample, a relatively small value (1.92) was obtained for the exponent, α. To improve the surface of the sample, it was removed from the sample holder, etched and electropolished for a relatively long time. During the mounting of the sample, it was dropped and a small chip broke off from the edge. The experimental results in the sample with its new dimensions, 2.65 x 2.75 x 13 mm, are given in Figs. 18, 19, and 20. Even though in this experiment a larger value (1.96) was obtained for the exponent, α, the magnetoresistance decreased by about 50%. Similarly, a very large change also was observed in the E and N-E coefficients, but when the result in the lattice thermal conductivity was compared with the results of the other investigators, no noticeable change was observed.

It should be pointed out that in the study of the effective density of states (Z_{eff}) in Chapter I, magnetoresistance and E-coefficient from the first set of measurements and the lattice thermal conductivity from the last experiment have been used.

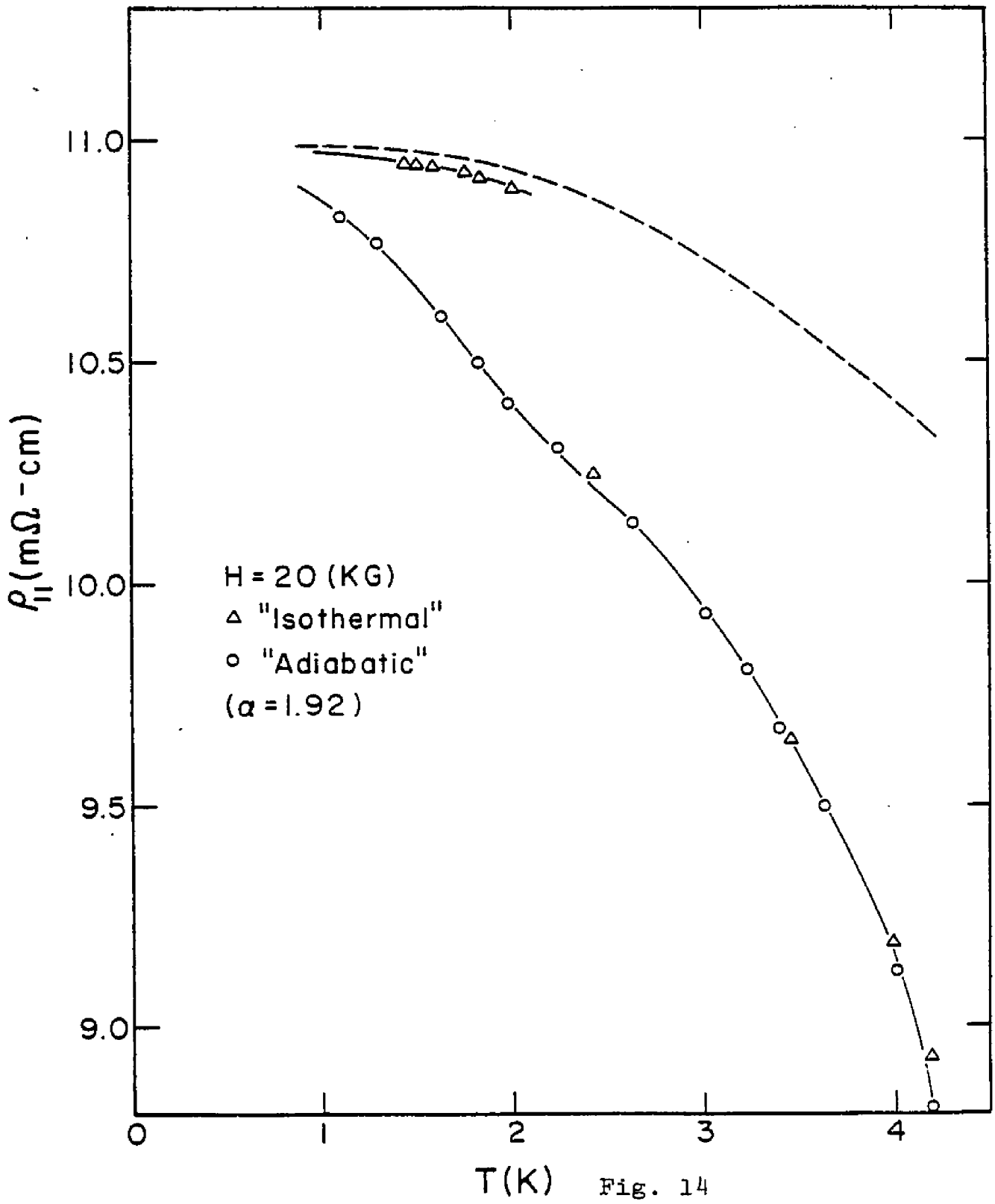
11.0
10.5
10.0
9.5
9.0
ρ_{11} (mΩ - cm)
H = 20 (KG)
△ "Isothermal"
○ "Adiabatic"
(α = 1.92)
0
1
2
3
4
T(K)

Fig. 14

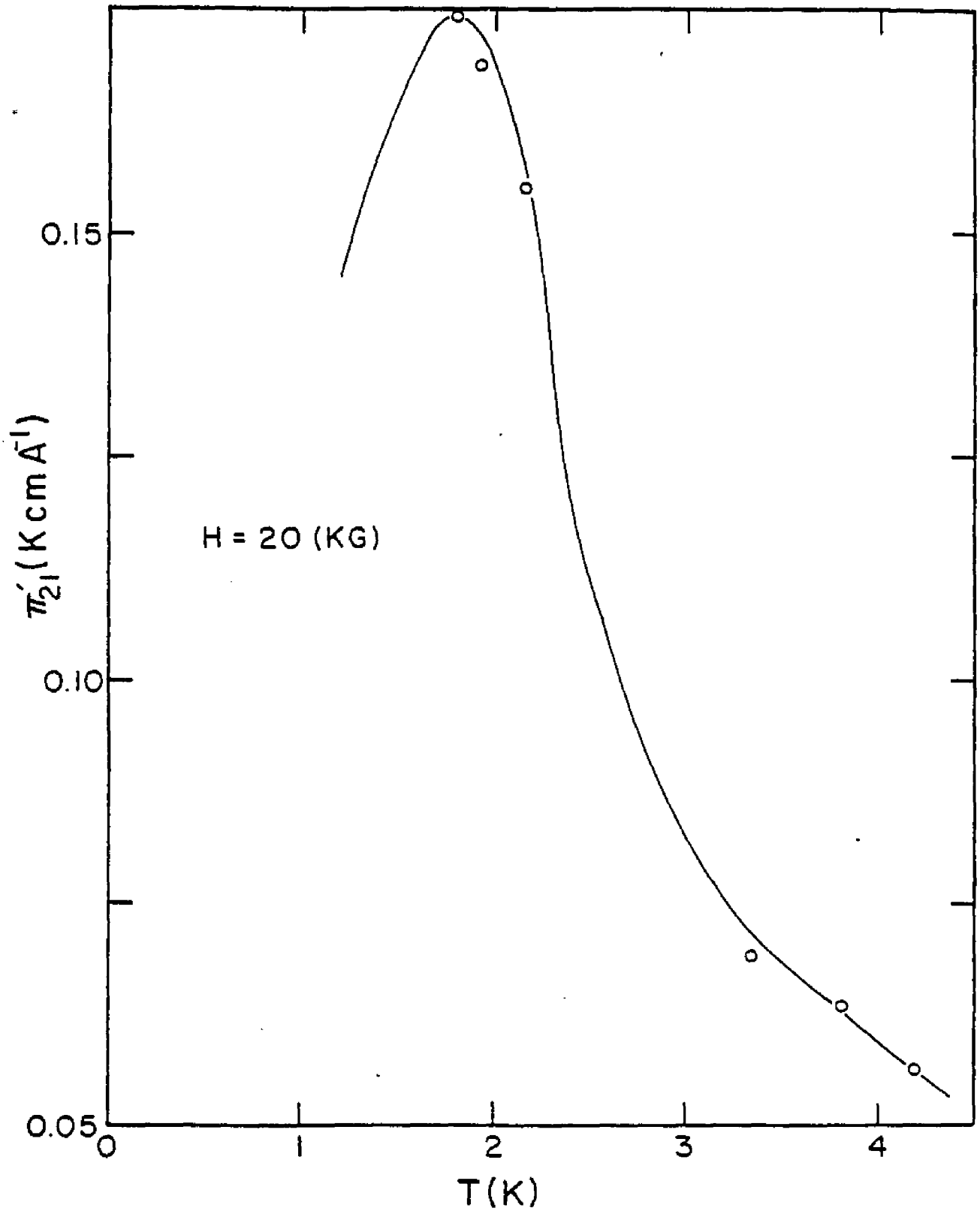

Fig. 15

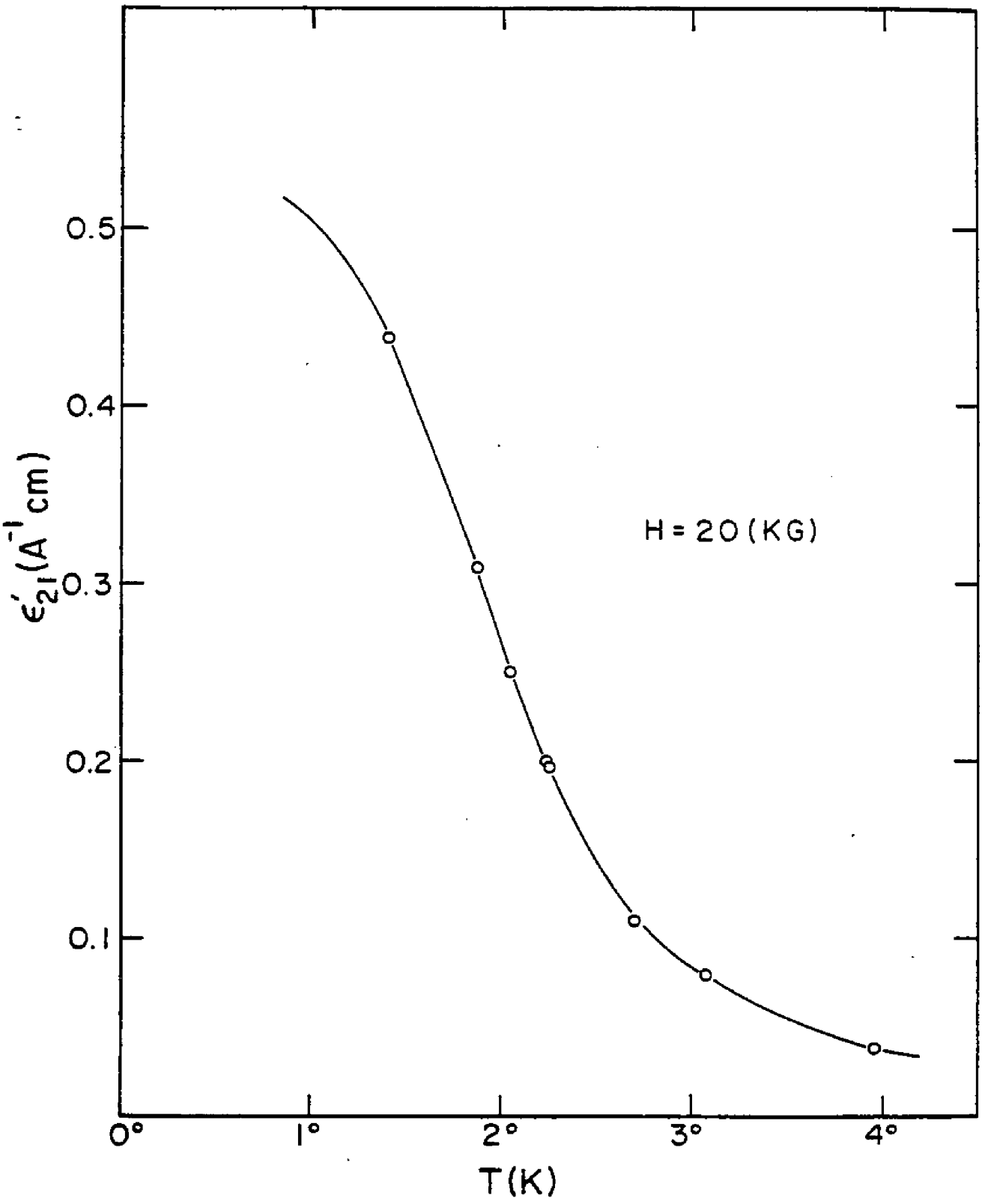

Fig. 16

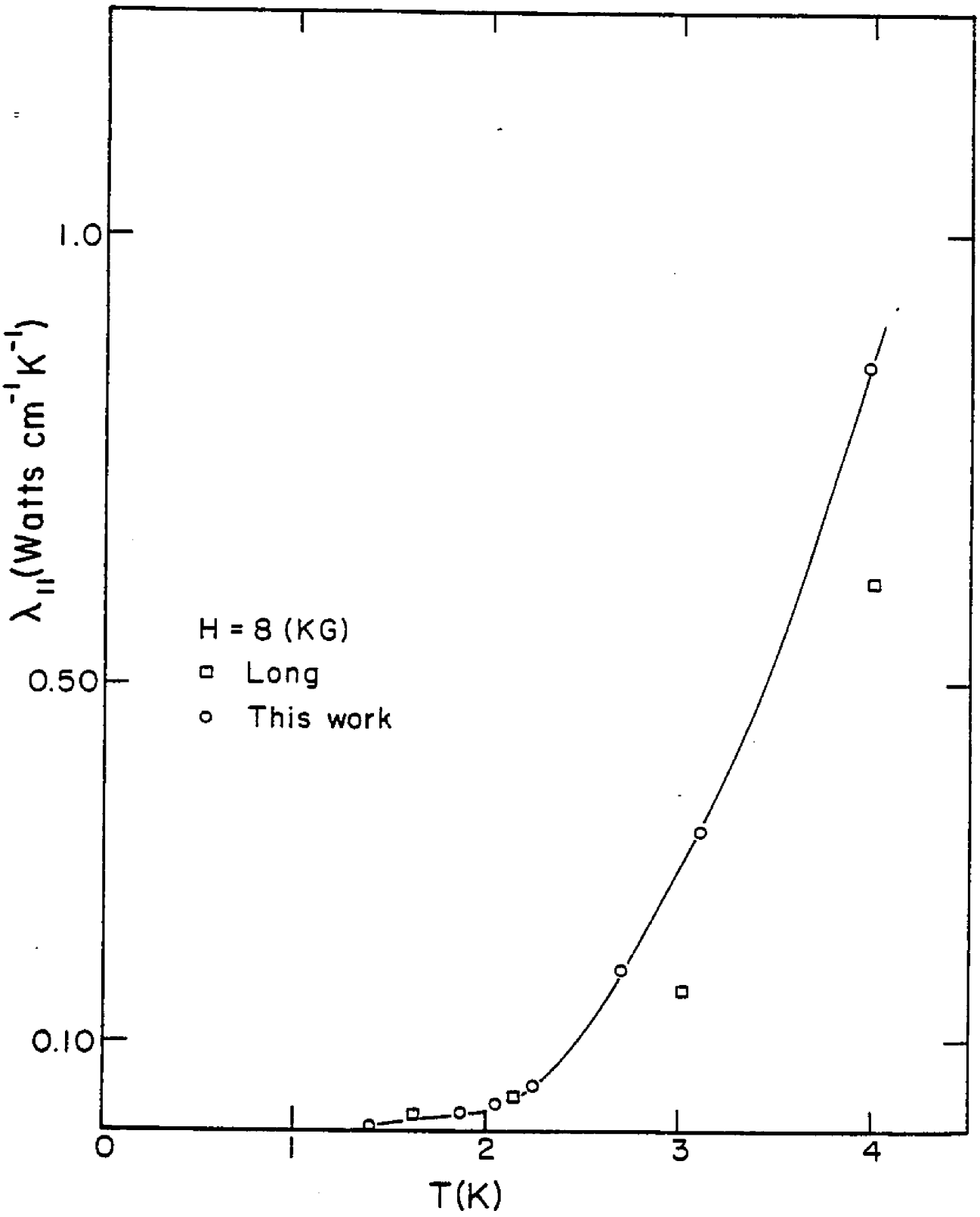

Fig. 17

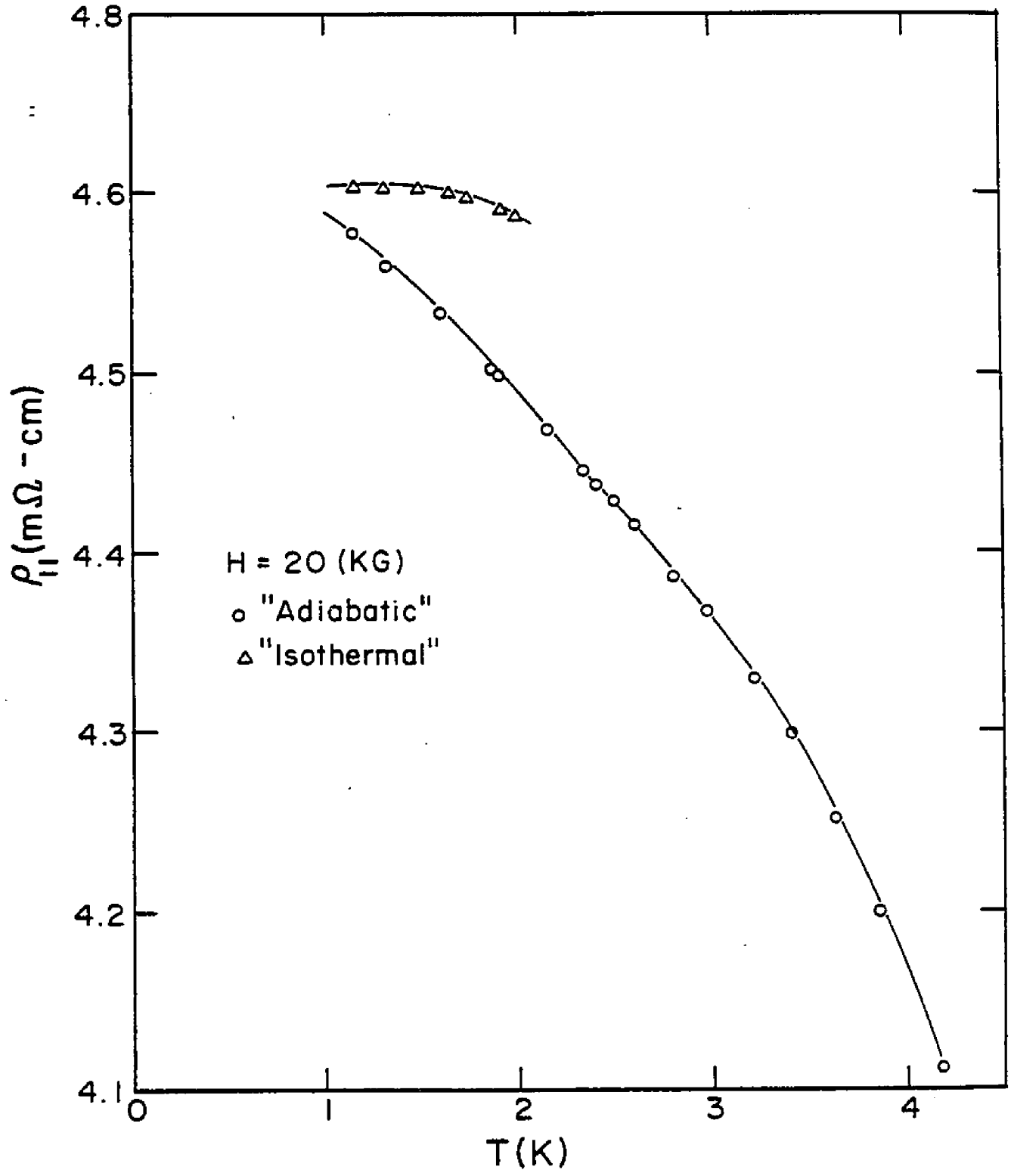
4.8
4.6
4.5
4.4
4.3
4.2
4.1
ρ_{11} (mΩ - cm)
H = 20 (KG)
o "Adiabatic"
Δ "Isothermal"
0
1
2
3
4
T(K)

Fig. 18

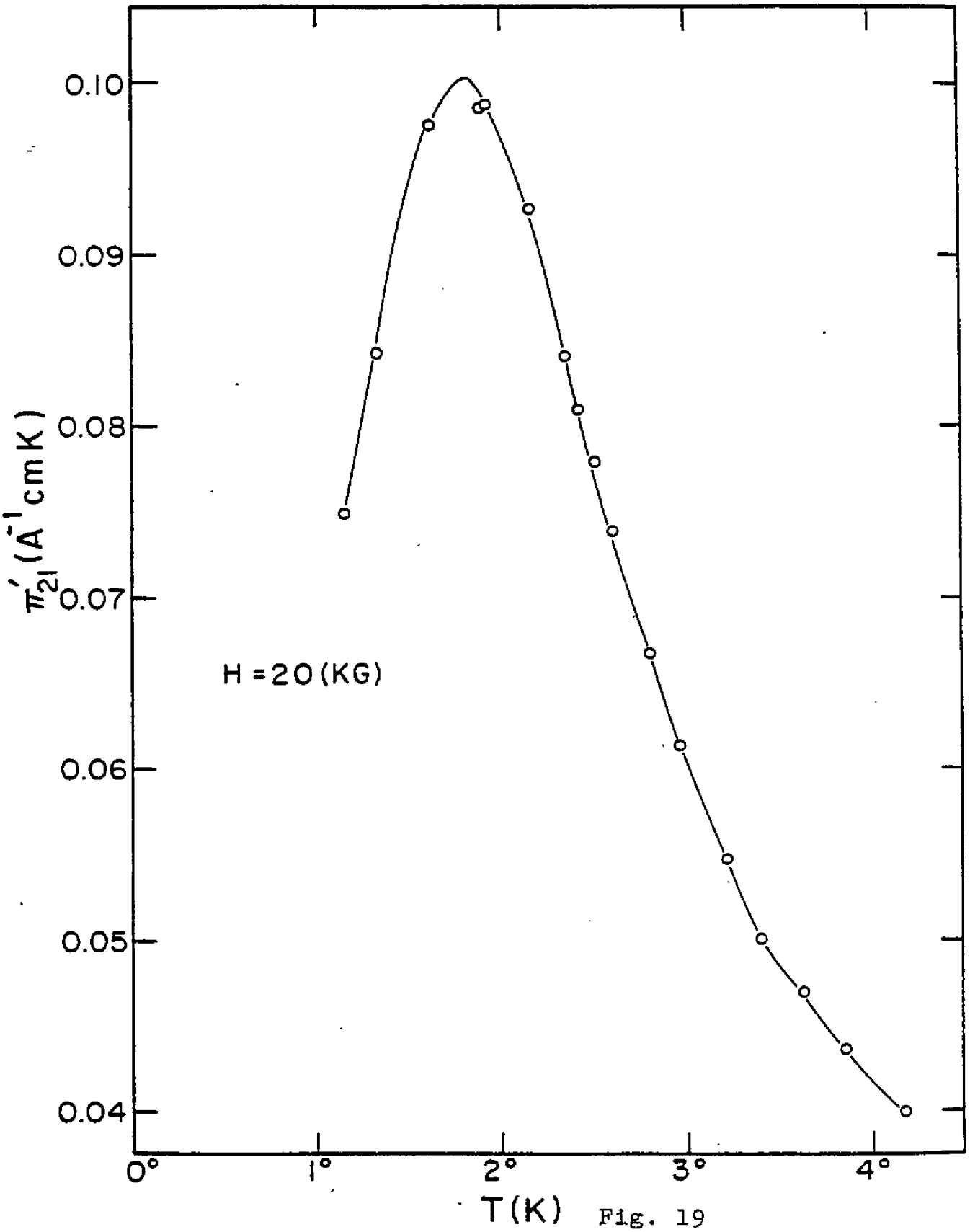

Fig. 19

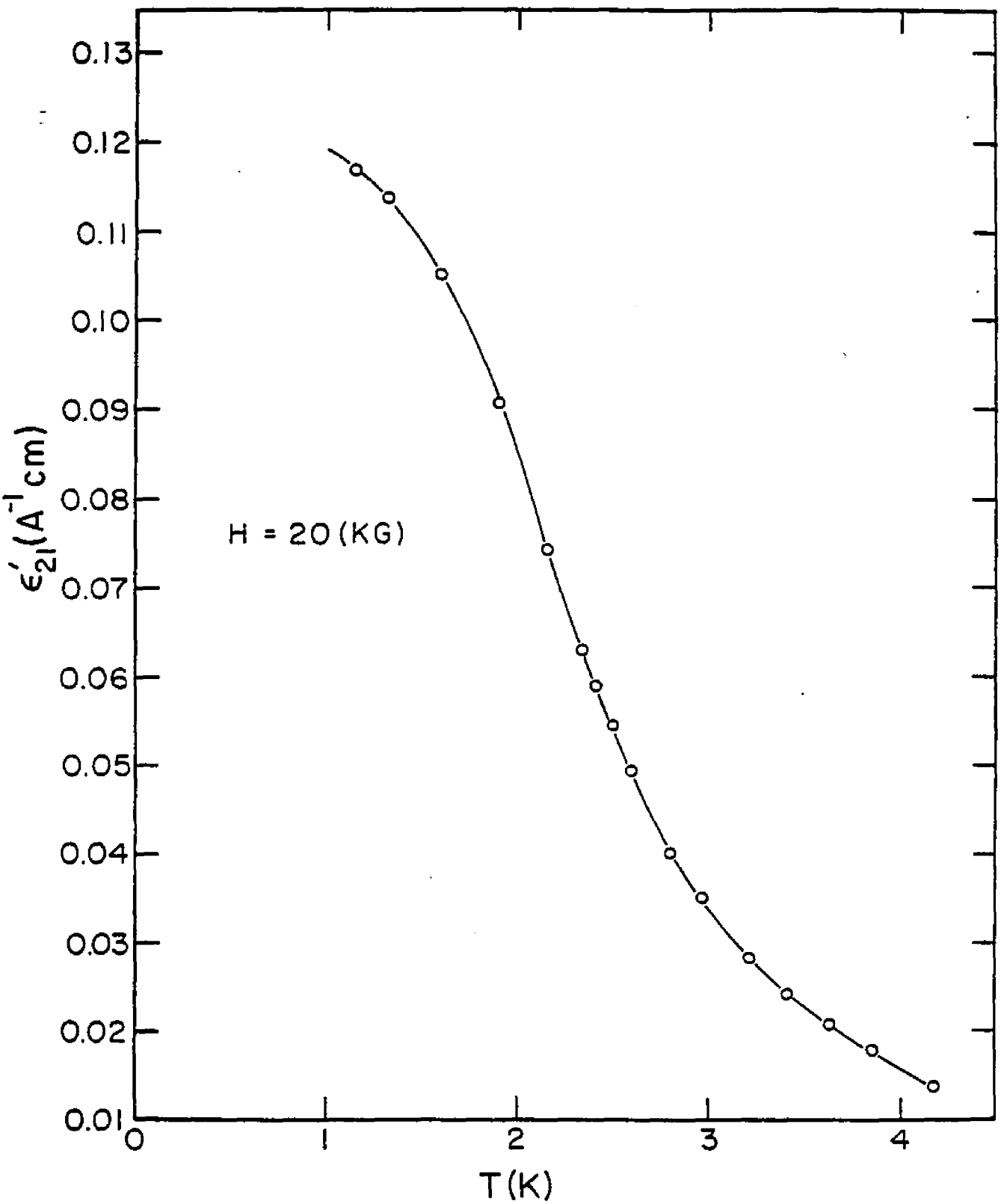
0.13
0.12
0.11
0.10
0.09
0.08
0.07
0.06
0.05
0.04
0.03
0.02
0.01
$\epsilon'_{21}(A^{-1}cm)$
H = 20 (KG)
0
1
2
3
4
T(K)

Fig. 20

G - Conclusions

Study of the magnetoresistance in the Corbino geometry showed that this geometry is perfect for the isothermal magnetoresistance investigation. In the experiments which were performed under two different conditions (the sample in a vacuum and in contact with the liquid helium), no significant change in the magnetoresistance was observed. In order to show that the circular symmetry of the geometry is the responsible factor for the isothermal measurement, a radial slot was cut through the sample. In the study of the magnetoresistance of this sample in contact with liquid helium, a jump at λ point was observed which is similar to what one observes in a rod geometry where the liquid helium becomes superfluid.

In the study of the effect of surface current on the magnetoresistance in the Corbino geometry, our results are consistent with what had been observed by Tsai, et al., in the rod geometry, i.e., by electropolishing the sample, the largest value for the magnetoresistance and the exponent, α, was measured.

Because of the absence of the diffusion layer in the Corbino geometry, one almost expects to observe the bulk properties of the sample in an electropolished sample, especially with a relatively large thickness where the ratio of δ/t becomes very small. But, instead, a value ($\alpha \simeq 1.97$) was measured which was close to what had been obtained

earlier for the rod geometry. Therefore, one expects to see some other unlikely effects coming from the geometry of the sample. Comparing the two geometries, we could see that any kind of inhomogeneity in the sample, such as crystal dislocation, defect, imperfections or having a multicrystal, has a much larger effect in the Corbino geometry than it has in the rod geometry. Actually, in the experiment in a rod geometry one needs to have a high quality sample only between the potential probes, whereas in a disk geometry, the whole sample has to be perfect and homogeneous. Nonuniform current distribution in the sample also has effect in the magnetoresistance measurement. This situation, which is not expected to happen in a rod geometry, would be observed in the Corbino geometry if the current is not injected exactly at the center of the disk.

In the magnetoresistance measurement in Corbino geometry, where two pairs of potential probes were soldered to both sides of the sample, almost always two different values for the exponent, α, and $\frac{\Delta\rho}{\rho_o}$x100, the percentage change in the magnetoresistance from 4 to zero degrees Kelvin, were obtained. For instance, in the experiment on the sample with the thickness t = 7.5 mm, values $\alpha_1 = 1.92$, $(\frac{\Delta\rho}{\rho_o})_1$x100 = 15.3% from one side and $\alpha_2 = 1.97$, $(\frac{\Delta\rho}{\rho_o})_2$x100 = 16.6% from the other side, were measured. It should be noticed that even existence of different damaged layers on each side of the sample is not expected to lead to such a difference. In fact, presence of any damaged layer in one side of the sample

should manifest itself in both measurements. Since no attempt was made to solder both potential probes in the same plane, a small deviation of the magnetic field from the symmetry axis of the disk would lead to small but different contribution of the component ρ_{33} in the magnetoresistance measurement using two different probes. This effect is called the "shadow effect". A similar effect in the lattice thermal conductivity measurement also is expected. A schematic diagram of the shadow for two different types of feeding the current to the sample is shown in Fig. 21.

Because of the large uncertainty in the geometric factor measurement, the experimental result in the study of the thickness effect in the magnetoresistivity in the Corbino geometry is not accurate enough to extract any quantitative result. However, qualitative investigation of this effect shows that the thickness effect in this geometry is smaller than in the rod geometry. For a sample with the thickness larger than 3 mm, the measured magnetoresistivity is almost independent of the thickness.

Study of the peeling effect on the rod sample (Tsai's rod sample No. 5) showed a very interesting result. In this experiment a value very close to 2 was obtained for the exponent, α. But, when the magnetoresistance of the sample was compared with the value obtained by Tsai for an electro-polished sample with the same average size, d (Tsai I, Fig. 4), no significant change was observed. However, it should

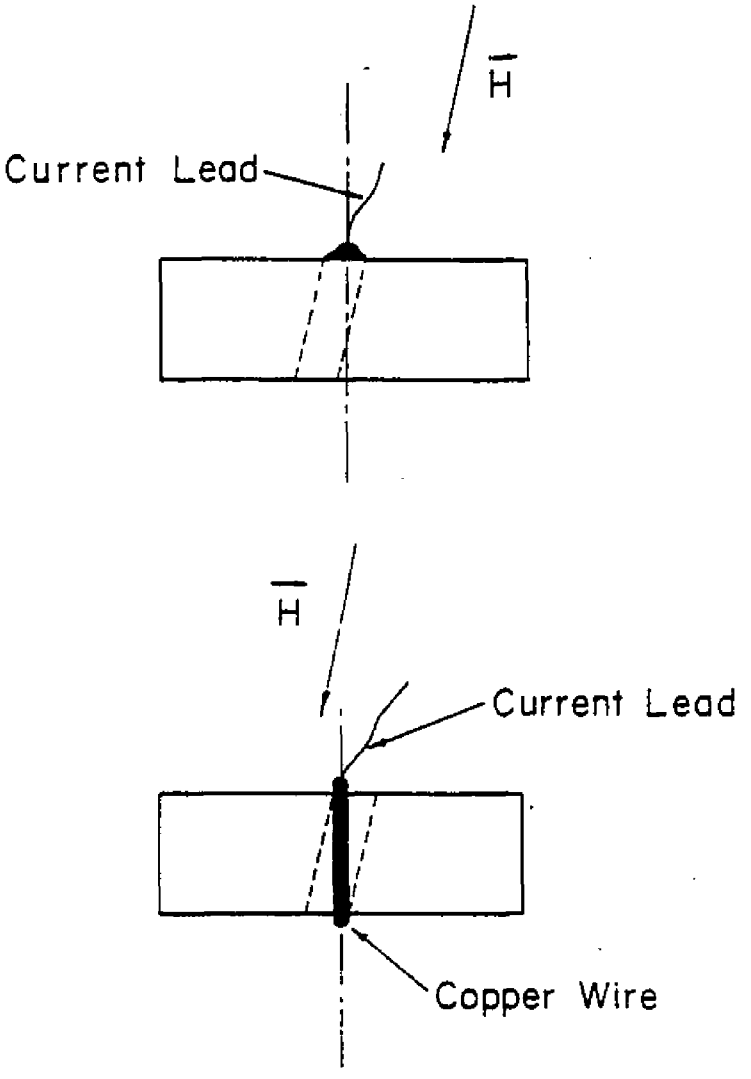

Fig. 21

be noticed that in the study of the size effect on a sample with a nearly close square cross section, it is reasonable to define an average size d = 4A/p (where A is the area and p the perimeter of the cross section). In the case of our sample with the dimensions 1.5 x 3.5 mm, such a definition would not represent the size effect on the sample. In other words, to compare magnetoresistance of the sample with another sample which has different surface treatment, exactly the same cross sections for both samples are required.

CHAPTER III

LATTICE THERMAL CONDUCTIVITY OF ANTIMONY IN A ROD AND CORBINO GEOMETRIES

A - Introduction

Thermal conductivity in general can be expressed as the sum of the lattice and electronic contribution,

$$\lambda = \lambda_e + \lambda_g \ . \qquad (60)$$

In metals, because of the high electron density, the contribution of the lattice in thermal conductivity is very small, and almost negligible, $\lambda_e >> \lambda_g$. In semimetals where electronic density is smaller than in metals, the conductivities become comparable. Their relative contribution in the thermal conductivity depends on the semimetal under investigation. For example, in bismuth with a small charge density, the lattice conduction is the main part of the whole thermal conductivity; on the other hand, in antimony, the situation is reversed and only a small amount of heat is carried by the lattice. In the presence of a magnetic field, the electronic part, λ_e, which is proportional to H^{-2} approaches zero, and one can study quite easily pure lattice conductivity of antimony by applying a moderate magnetic field (H > 5 KG).

The lattice thermal conductivity of antimony in a rod geometry has been studied by G. K. White and S. B. Woods,[20] J. R. Long, et al.,[21] R. S. Blewer, et al.,[22] and C. L. Tsai,

et al. When the experimental results in the lattice thermal conductivity in the rod geometry are compared with the results in the Corbino geometry, considering the fact that different boundary conditions exist in the two geometries, one expects to observe a difference between these two measurements.

Using the transport equations (4) and applying transformation from Cartesian coordinate to cylindrical coordinate with appropriate boundary conditions, one obtains (Eq. 52),

$$\lambda_{disk} = \lambda''_{11} = \frac{\lambda_{11}}{1 + \frac{\varepsilon'_{21}\pi'_{21}\lambda_{11}}{\rho^a_{11}}} \tag{61a}$$

or

$$\frac{\lambda''_{11} - \lambda_{11}}{\lambda_{11}} = -\left(\frac{\rho_{11} - \rho^a_{11}}{\rho_{11}}\right), \tag{61b}$$

where λ_{disk} and λ_{11} are the lattice thermal conductivities in the Corbino and rod geometries, and λ''_{11} is the isopotential lattice thermal conductivity introduced in the first set of transport equations. From Eq. (61) $\lambda_{disk} < \lambda_{11}$ is expected. By measuring ε'_{21}, π'_{21}, λ_{11}, and ρ^a_{11}, the difference $\Delta\lambda = \lambda_{disk} - \lambda_{11}$ can be calculated: at T = 4°K, $\frac{\Delta\lambda}{\lambda} \simeq -0.12$ and at T = 1°K, $\Delta\lambda \simeq 0$. In spite of expectations from Eq. (61), a value larger than λ_{11} for λ_{disk} was experimentally obtained (at T = 4°K, $\frac{\Delta\lambda}{\lambda} = 0.08$). The apparent disagreement between experimental data and theoretical result will be discussed in Section C.

B - Experimental Detail

The monocrystalline rod sample with a rectangular cross section was cut by a spark cutter from the same ingot which the circular disk had been cut. The sample was lapped with emery paper No. 600 and chemically etched with aquaregia and electropolished in a basic solution KOH. Similar surface treatment also was used in the disk sample preparation. The long dimension of the rod sample, that is, the current direction, was cut parallel to the bisectrix axis (x-axis) and the lateral faces perpendicular to the binary axis (y-axis) and the trigonal axis (z-axis). In both geometries, the magnetic field (H = 8 KG) was kept along the trigonal axis. The radius and thickness of the disk after surface treatment were 6 mm and 3 mm, respectively. Dimensions of the rod sample after the surface treatment were 2.99 x 3.42 x 18.5 mm. The sample mounting and experimental technique was such that one could make both electrical and thermal measurements simultaneously.

In the first set of measurements on the rod sample, because of some technical problems, the result obtained in the thermal conductivity measurement was not consistent with the results obtained by the other investigators. Therefore the experiment was repeated. Detail in preparation of the sample for the second set of measurements are noted in Chapter II. The dimensions of the sample in the second experiment were 2.68 x 2.75 x 12 mm.

The temperature gradient measurement was made with Allen-Bradley carbon resistors (50 Ω and 1/10 μw). All solder connections to the samples were made with 60-40 Bi-Cd eutectic. The sample holder was screwed tight and soldered with indium to the heat sink. High vacuum (10×10^{-6} mm Hg) was attained by using a diffusion pump, and it also was connected to a leak detector during the experiment. Magnetic and cryogenic equipment were identical to those used by Tsai, et al. Potential difference in magnetoresistance and Nernst-Ettingshausen coefficient measurements were made with a Rubican potentiometer, using a 147 Keithley nanovoltmeter as the null detector. The electric current in the sample and through the thermometers and also the voltage across the thermometers were measured by a type K-3 universal potentiometer.

Thermometers were calibrated in the presence of helium exchange gas in the vacuum chamber. Recalibration of the thermometers was made any time that the sample was brought to room temperature.

Four different methods were employed for temperature gradient measurement in both geometries. Details are given in Appendix A.

Schematic diagrams of the sample and heaters arrangement for both rod and disk are shown in Figs. 3 and 4.

C - Theory

Phenomenological theory for lattice conductivity in which the relaxation effect from the three-phonon normal process is taken into account has been given by Callaway.[23] Calling τ_N^{-1} the relaxation frequency due to the three-phonon normal scattering and τ^{-1} the combined resistive scattering frequency of phonons by other processes, one can write λ_g as

$$\lambda_g = \frac{k}{2\pi^2 s_g}\left(\frac{kT}{\hbar}\right)^3 \left(A_1 + \frac{A_2^2}{A_3}\right) \tag{62}$$

where

$$A_1 = \int_0^{\theta_D/T} \frac{1}{\tau^{-1}+\tau_N^{-1}} \frac{x^4 e^x}{(e^x-1)^2}\, dx \tag{63a}$$

$$A_2 = \int_0^{\theta_D/T} \frac{\tau_N^{-1}}{\tau^{-1}+\tau_N^{-1}} \frac{x^4 e^x}{(e^x-1)^2}\, dx \tag{63b}$$

$$A_3 = \int_0^{\theta_D/T} \frac{\tau_N^{-1}\tau^{-1}}{\tau^{-1}+\tau_N^{-1}} \frac{e^x x^4}{(e^x-1)^2}\, dx. \tag{63c}$$

Isotropy and absence of dispersion in the crystal vibration spectrum are assumed and no distinction is made between longitudinal and transverse phonons. As implied by these three assumptions, s_g, is the velocity of sound. The parameter $x = \frac{\hbar\omega}{kT} = \frac{\hbar q s_g}{kT}$ where ω and q are the phonon frequency and wave vector, respectively. $x_D = \frac{\theta_D}{T}$ corresponds to $\omega = \omega_D$ or $q = q_D$ with θ_D, ω_D and q_D the Debye temperature, Debye cutoff frequency and the radius of the Debye sphere, respectively.

Equation (62) takes a simplified form depending on the relative strength of τ_N^{-1} and τ^{-1}. For $\tau_N^{-1} < \tau^{-1}$, λ_g can be written as

$$\lambda_g = \frac{k}{2\pi^2 s_g}\left(\frac{kT}{\hbar}\right)^3 \int_o^{\theta_D/T} (\tau^{-1}+\tau_N^{-1})^{-1} \frac{x^4 e^x}{(e^x-1)^2}\, dx \qquad (62a)$$

and eventually for $\tau_N^{-1} << \tau^{-1}$,

$$\lambda_g = \frac{k}{2\pi^2 s_g}\left(\frac{kT}{\hbar}\right)^3 \int_o^{\theta_D/T} \tau \frac{x^4 e^x}{(e^x-1)^2}\, dx. \qquad (62b)$$

The condition $\tau_N^{-1} < \tau^{-1}$ is characteristic of a poor phonon mixing.

Under opposite condition of strong phonon N-process ($\tau_N^{-1} > \tau^{-1}$), the conductivity takes the form as obtained by Ziman[24] and by Makinson[25]

$$\lambda_g = \frac{k}{2\pi^2 s_g}\left(\frac{kT}{\hbar}\right)^3 \mathcal{J}_4^2(\theta_D/T) \int_o^{\theta_D/T} \tau^{-1} \frac{x^4 e^x}{(e^x-1)^2}\, dx \qquad (62c)$$

where $\mathcal{J}_4(\frac{\theta_D}{T})$ is Debye function of order 4. The different forms of Eqs. (62a), (62b), and (62c) could be employed depending on the knowledge of the different scattering strength at any particular temperature region. For example, in the case of antimony, in the most range of liquid helium temperature form (62a), at temperature around $T \approx 4°K$ form (62b), and at higher temperature (above 15°K), form (62c) should be used. At the temperature range between $T \approx 6°K$ and $T \approx 15°K$, where the strength of τ^{-1} and τ_N^{-1} become comparable, Eq. (62) must be employed.

Assuming additivity of the resistive scattering, one can write

$$\tau^{-1} = \tau_b^{-1} + \tau_c^{-1} + \tau_u^{-1} \tag{64}$$

where τ_b^{-1}, τ_c^{-1}, τ_{iso}^{-1} and τ_u^{-1} are the frequency of scattering of phonons by boundaries, carriers, isotopes and phonons (Umklapp process), respectively.

The scattering relaxation frequency by crystal boundaries and surface dislocations can be written as

$$\tau_b^{-1} = b = \frac{s_g}{\Lambda} \tag{65}$$

where Λ, the Casimir[26] length, is of the order of the crystal size. For a rectangular cross section $\Lambda = 1.12\ell$ with ℓ the mean width of the section.

The relaxation frequency associated with isotope scattering[27,28] is given in the nondispersive case by

$$\tau_{iso}^{-1} = Dq^4 = dx^4T^4 \tag{66}$$

where $D = s_g \Sigma N_i \langle \delta M_i \rangle^2 / 4\pi\rho^2$ and $d = \frac{Dk}{s_g}$. N_i is the number of a given kind of isotope atoms (per cm^3), $\langle \delta M_i \rangle^2 = (M_i - \bar{M})^2$, with M_i the isotope mass and $\bar{M}$ the average atomic mass. In the case of natural antimony $D \simeq 4 \times 10^{-23}\ cm^{-4}sec^{-1}$ and $d \simeq 3.07°K^4sec^{-1}$.

The normal three-phonon relaxation frequency as used by Callaway[23] is given by Herring[29] as

$$\tau_N^{-1} \propto x^p T^5 \qquad \text{or} \qquad \tau_N^{-1} \propto q^p T^{5-p} \tag{67}$$

with p = 2 in cubic symmetry and p = 3 in an isotropic structure for the nondispersive longitudinal phonons.

The Umklapp process[29] leads to scattering of the form

$$\tau_u^{-1} = f(T,q)e^{-\theta_D/\alpha T} \quad \text{with } 1<\alpha<2.$$

The form of f(T,q) is still a matter of much conjecture. Thus, f(T,q) could be taken proportional to qT^{-1};[30] q^2T^3[23] or q^2T.[31] More complex forms of τ_u^{-1} also could be used. The form given by Klemens,[30]

$$\tau_u^{-1} \simeq 8\Gamma^2\left(\frac{\theta_D}{Ms_g}\right) bxe^{-\theta_D/\alpha T} \tag{68}$$

where Γ is the Gruneisen constant and b the reciprocal lattice vector which in the cubic case can be approximated by $2\pi(V_a)^{-1/3}$ where V_a is the atomic volume.

Because of the existence of the six-hole pockets and three-electron pockets, the relaxation frequency of the phonon by the carriers can be written as

$$\tau_c^{-1} = 6\tau_h^{-1} + 3\tau_e^{-1} \tag{69}$$

where τ_h^{-1} is the scattering relaxation frequency due to the hole carriers contained in one of the hole Fermi pockets and τ_c^{-1} corresponds to that of an electron pocket. The τ_h^{-1} and τ_e^{-1} can be approximately formulated if besides the phonon-isotropy assumption, the carrier pockets are supposed to be isotropic (spherical) and to obey a quadratic energy law; then[32]

$$\tau_h^{-1}(q) \simeq \frac{m_h^2\ \epsilon_{def}^2}{2\pi\rho h^3}\ q \quad \text{for } q \leqslant 2k_h \tag{70}$$

and

$$\tau_h^{-1}(q) = 0 \qquad \text{for } q > 2k_h \tag{71}$$

with a similar equation for τ_c^{-1}. The terms m_e and m_h are the effective masses of the carriers, ε_{def} deformation potential (is assumed to be the same for both bands), ρ is the mass density and k_e, k_h are the Fermi pockets radii (k_F). Under isotropic and quadratic assumption for Fermi pockets, masses and radii can be approximated[33-36] with $k_e = 8.1 \times 10^6$ cm^{-1}, $k_h = 6.4 \times 10^6$ cm^{-1}, $m_e = 0.28\ m_o$, and $m_h = 0.14\ m_o$.

The effect of the selective scattering, described earlier, would correspond to breaking the range of integration in the conductivity integrals into three ranges. The first range of integration accounts for the phonons scattered by both holes and electrons ($0 < q < 2k_h$). In the second range the phonons are still scattered by electrons ($2k_h < q < 2k_e$), whereas the third region accounts for the phonons which are scattered by neither of the carriers ($2k_e < q < q_D$). Those phonons which are outside of the sphere of diameter $2k_e$ will be referred to as the "peripheral" phonons. The effective Debye temperature θ_h^*, θ_e^* associated with the scattering are given by $\theta_h^* = (\frac{2k_h}{q_o})\theta$ or $K\theta_h^* = \hbar s_g(2k_h)$ with the same expression for θ_e^*. (72)

We point out that the 4-region scheme with the effective temperatures θ_1^*, θ_2^* and θ_3^* as introduced in the first chapter, also would lead to the same result when the isotropic Fermi pocket assumption for the carriers is made.

The relation between these effective temperatures and the theoretical values for θ_e^* and θ_h^* under isotropic assumption are given in Chapter I.

It is clear that the anisotropy in $k_{h,e}$ and s_g would lead Eq. (72) to determine a whole spectrum of θ^* values. This effect probably would be more important than the effect brought about by the distinction between holes and electrons. With this assumption, the experimental results could be analyzed by considering a single empirical averaged θ^*, or more correctly a $\theta^*(T)$, adjustable function, and increasing with the temperature as expected. This assumption will be used in the final fitting.

As it was mentioned before, the general form of Eq. (62) could be investigated for three different limits: i) $\tau_N^{-1} < \tau^{-1}$, ii) $\tau_N^{-1} << \tau^{-1}$ and iii) $\tau_N^{-1} > \tau^{-1}$. Experimental results in lattice thermal conductivity of antimony at helium temperature as shown by Blewer, et al.,[22] strongly suggests the condition of weak phonon mixing Eq. (62b) where $\tau_N^{-1} << \tau^{-1}$.

The argument made about empirical θ^* would allow the range of integration in Eq. (62b) to be broken into two ranges.

$$\text{a)} \quad x < \frac{\theta^*}{T} \text{ with } \tau^{-1} = \tau'^{-1} + \tau_c^{-1} = \tau^{-1} + cxT \qquad (73)$$

$$\text{b)} \quad x > \frac{\theta^*}{T} \text{ with } \tau^{-1} = \tau'^{-1} \qquad (74)$$

where c is a constant and τ'^{-1} represents the scattering other than the carriers' scattering, i.e.

$$\tau'^{-1} = b + dx^4T^4 + uxe^{-\theta_D/\alpha T} \quad . \tag{75}$$

Now Eq. (62b) can be written as

$$\lambda_g = \frac{k}{2\pi^2 s_g}\left(\frac{kT}{\hbar}\right)^3 \int_o^{\theta^*/T}(\tau^{-1} + cxT)\frac{x^4e^x}{(e^x-1)^2}dx + \int_{\theta^*/T}^{\theta_D/T}\tau'\frac{x^4e^x}{(e^x-1)^2}dx. \tag{76}$$

Below 1.4°K the near T^2 dependence of λ_g, Fig. 23 strongly suggests that in the first term in Eq. (76) the carrier scattering is preponderant and the second term in Eq. (76) is negligible, so that λ_g can be approximated in this range (with $\theta^*/T \to \infty$) by

$$\lambda_g \simeq \frac{k}{2\pi^2 s_g}\left(\frac{kT}{\hbar}\right)^3 \int_o^{\infty} \frac{1}{b+cxT}\frac{x^4e^x dx}{(e^x-1)^2} \quad . \tag{77}$$

This term at higher temperature would tend toward

$$\frac{k}{2\pi^2 s_g}\left(\frac{kT}{\hbar}\right)^3 \frac{1}{cT}\,\mathcal{J}_3\left(\frac{\theta^*}{T}\right) \tag{78}$$

as the effect of b is becoming negligible, and the isotope effect is still negligible. Above 1.4°K where the sharp increase in conductivity will be associated with the second term in Eq. (76) which represents the contribution of the peripheral phonon, λ_g can be written as

$$\lambda_g \simeq \frac{k}{2\pi^2 s_g}\left(\frac{kT}{\hbar}\right)^3 \left[\frac{1}{cT}\,\mathcal{J}_3\left(\frac{\theta^*}{T}\right) + \int_{\theta^*/T}^{\infty}\frac{1}{b+dT^4x^4}\frac{e^x x^4}{(e^x-1)^2}\,dx\right] \tag{79}$$

as θ_D/T is taken to ∞.

The parameters c, b, d and θ^* can be determined experimentally and compared with the estimated values obtained from the theoretical formula.

Finally, Eq. (62), introduced at the beginning of this section, has been derived under complete equilibrium condition of the carriers, i.e., zero electric current. This is exactly the same condition required for λ_{11}, defined in the second form of the transport equations ($\lambda_{11} = -\frac{W_x}{\nabla_x T}$, $J = 0$). Therefore, the result for λ_g which has been derived here can be employed for the theoretical investigation of the lattice thermal conductivity, λ_{11}, measured in the rod geometry.

D - Results and Discussions

Lattice thermal conductivity, λ''_{11}, was measured on disk sample No. 3 with a thickness of 3.38 mm at high field (H = 8 KG). The experimental result is shown in Fig. 22 where λ''_{11}/T^2 vs T is plotted. The geometric factor for this measurement was obtained by matching λ''_{11} with λ_{11}, thermal conductivity of the rod sample, at $T \simeq 1°K$. The fact that $\Delta\lambda = \lambda''_{11} - \lambda_{11}$ approaches zero at low temperature can be seen in Eq. (61). When the geometric factor was measured directly and compared with the calculated value obtained by matching, 18% discrepancy was observed. This value is close to the estimated error calculated in Chapter II.

The linear dependence of ε'_{21} and π'_{21}, and quadratic dependence of ρ_{11} in magnetic field suggest that the term $\frac{\varepsilon'_{21}\pi'_{21}}{\rho_{11}}\lambda^2_{11}$, which is the difference between λ''_{11} and λ_{11}, is field independent. However, the effect of surface current in these transport coefficients would cause this term to slightly vary with the magnetic field. Due to the presence of this term in Eq. (61a), one expects to see the same field dependence in λ''_{11}, also. But experimental study in λ''_{11} at H = 8 KG and H = 20 KG did not show any significant change in these measurements. (Because of the magnetoresistance of the thermometers, different calibrations at different fields were performed.)

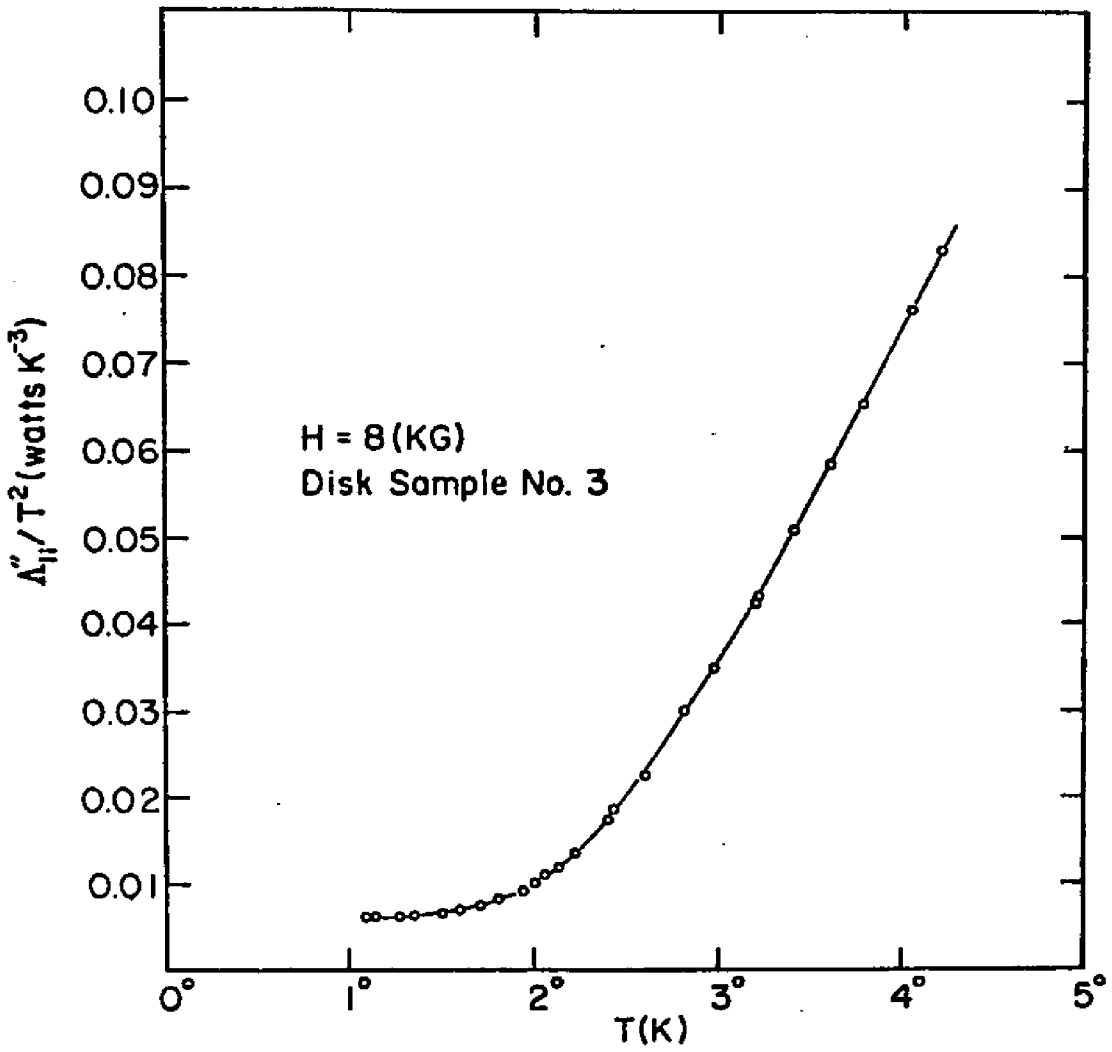
0.10
0.09
0.08
0.07
0.06
0.05
0.04
0.03
0.02
0.01
Λ''_{11}/T^2(watts K^{-3})
H = 8(KG)
Disk Sample No. 3
0°
1°
2°
3°
4°
5°
T(K)

Fig. 22

In the next experiment, ρ_{11}^{a}, ϵ_{21}', π_{21}' and lattice thermal conductivity, λ_{11}, were measured in the rod sample (D). Experimental results are shown in Figs. 14, 15, 16, and 17. When the result in the thermal conductivity measurement was compared with those of the other investigators, a large discrepancy was observed. Although the samples had been cut from different ingots and different surface treatments may have been used, these should not lead to such a large disagreement. In the second experiment, performed on this sample, some unexpected behaviors, probably due to the damage in the sample, were observed in ϵ_{21}', π_{21}', and ρ_{11}. For example, while the magnetoresistance of the sample decreased by about 50% from the last measurement, the exponent, α, increased from 1.92 to 1.96. However, the experimental result in the thermal conductivity measured in this sample was consistent with the results obtained by the other investigators. Experimental data on ρ_{11}^{a}, ϵ_{21}', π_{21}' and λ_{11}/T^2 are shown in Figs. 18, 19, 20, and 23, respectively.

In order to compare the lattice thermal conductivity in the rod and disk geometries, both experimental results, plotted on the same graph (Fig. 24), matched at low temperature ($T \approx 1°K$) where the difference, $\Delta\lambda$, approaches zero. Using Eq. (61a) or (61b), one can calculate λ_{11} from λ_{11}'' to compare with the measured value from the rod sample. The calculated value, λ_{cal}, obtained by using Eq. (61b) and the

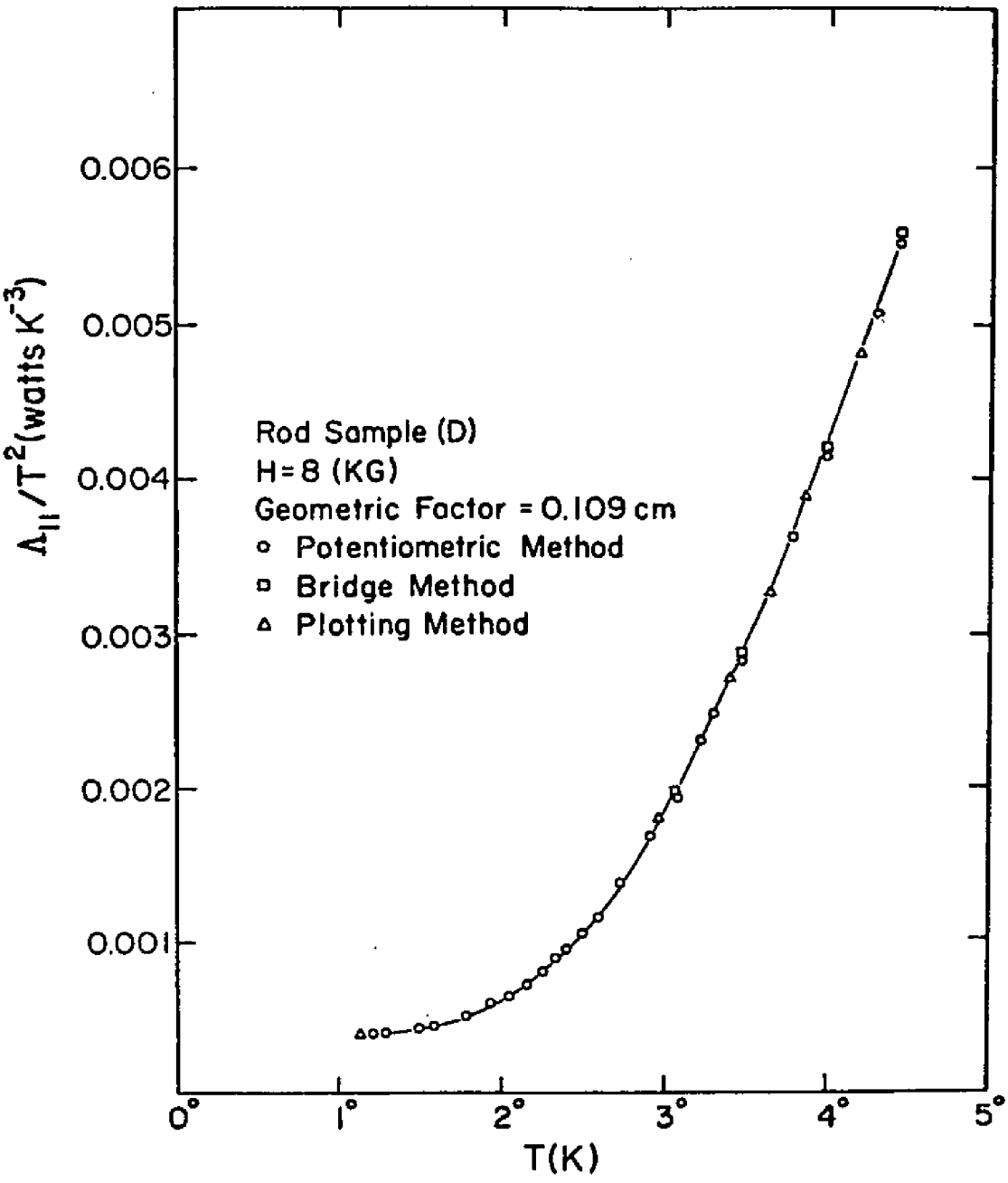
0.006
0.005
0.004
0.003
0.002
0.001
Λ_{11}/T^2(watts K^{-3})
Rod Sample (D)
H=8 (KG)
Geometric Factor = 0.109 cm
Potentiometric Method
Bridge Method
Plotting Method
0°
1°
2°
3°
4°
5°
T(K)

Fig. 23

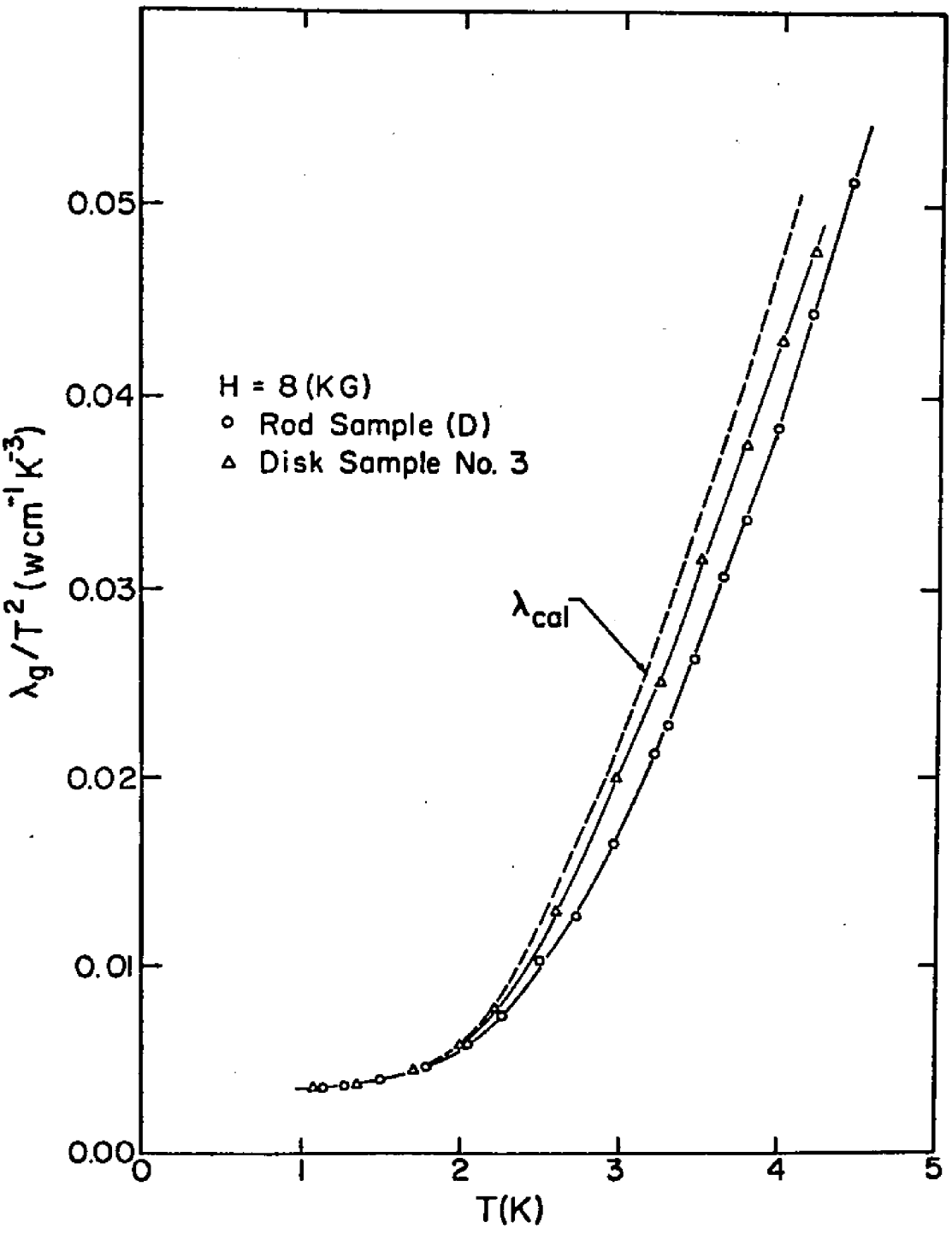
H = 8 (KG)
o Rod Sample (D)
Δ Disk Sample No. 3
λ_{cal}
λ_g/T^2 (w cm^{-1} K^{-3})
0.05
0.04
0.03
0.02
0.01
0.00
0
1
2
3
4
5
T(K)

Fig. 24

result shown in Fig. 14 , is represented by dashed lines in Fig. 24 .

To investigate the cause of such a relatively large difference between λ_{cal} and λ_{11}, which may not be very obvious at first glance, can be explained by considering Eq. (79) where the effect of the four parameters c, e, θ^* and b on the thermal conductivity could be observed. Since both samples had been cut from the same ingot, the first three parameters, which depend on the intrinsic properties and do not depend on the shape and geometry of the sample, cannot be responsible for such a discrepancy. The only parameter which depends on the geometry is b, the boundary scattering relaxation frequency. Therefore the difference between λ_{cal} and λ_{11} suggests two different scatterings in these two geometries.

Theoretical study of the boundary scattering in a rod geometry with a finite and infinite length has been given by Casimir[26] and Berman,[37] respectively. In this investigation it was assumed that each element of the surface after entirely absorbing the radiated phonons, re-emit phonons with an intensity depending on the temperature of the surface element, as in the theory of black-body radiation. Because of the simple form of the geometry, especially in a long sample, the calculation becomes straight forward and can easily be performed. But in the disk geometry, the problem is more difficult and complicated integrals are involved.

In order to determine boundary scattering in the Corbino geometry, one can find all four parameters, b (rod), c, d and θ^* by fitting the experimental result in the rod sample to Eq. (79). The values of c, d and θ^* which do not depend on the geometry can be used in the second fitting where λ_{cal} is fitted to Eq. (79). In this case there is only one adjustable parameter, b(disk), which can be determined.

Since θ^* slightly depends on temperature, it would be more accurate if a small range of temperatures is used for the above investigation. This range could be selected at high temperature where $\Delta\lambda/\lambda_{11}$ has its largest value.

In the first step the whole temperature range of the experimental data on the rod sample was fitted to the theoretical formula, Eq. (79). The best fit was attained by varying θ^* from 21.5 to 25.3°K (close to $\theta_h^* \approx 22.5$°K which was obtained by using the experimental result in the thermoelectric power given in Chapter I, and in magneto-conductivity investigation given in Tsai II), and with $c = 12.5 \times 10^6$ $(°K\ sec)^{-1}$, and $d = 3.07°K^{-4}sec^{-1}$ which are in agreement with Blewer's result in a similar investigation, and b(rod) = 8.2×10^5 sec^{-1}, which is almost the same as the calculated value b(rod) = 8.22×10^5 sec^{-1} from the Casimir formula.

Using the above values for c, d, and θ^*, and fitting λ_{cal} to the theoretical formula, we obtained a value of

$b(\text{disk}) = 2.2 \times 10^5\ \text{sec}^{-1}$, which is about 1/4 of the boundary scattering in the rod sample. Because of the relatively large uncertainty in the isothermal magnetoresistance used in Eq. (61b), the value obtained for b(disk) is not expected to be as accurate as the value of the boundary scattering in the rod sample. However, it is expected, due to the shape and size, that the boundary scattering in the Corbino geometry be much smaller than in the rod geometry. One can show that an upper limit for b(disk) is attained when one neglects the difference between λ_{11} and λ''_{11} given by Eqs. (61a) or (61b). Even though this approach is obviously wrong, the upper limit value for b(disk) obtained under such a condition would be $b(\text{disk}) = 4.5 \times 10^5\ \text{sec}^{-1}$ which is still about 50% smaller than the value obtained for the boundary scattering in the rod sample.

In conclusion, several interesting points can be made from the thermal conductivity investigations.

1) The effect of damaged layers on the measured lattice thermal conductivity is practically zero. This result, which is in agreement with the assumption made by Tsai in the study of the effect of damaged layers on the transport coefficients, was inferred when a relatively large effect was measured in the magnetoresistance of the sample; but, when the measured lattice thermal conductivity in this sample was compared with those of the other investigators, no significant change was observed.

2) The value obtained for the boundary scattering relaxation frequency, b, in the rod sample is quite close to the theoretical value derived from the Casimir formula.

3) The value of the effective Debye temperature, θ^*, is consistent with the values obtained in Chapter I, in thermoelectric power and density of state investigations, and the overall diverse cut off effective temperature obtained in the preceding work (Tsai II and III).

4) Corbino geometry is a desired geometry for study of λ''_{11}, the isopotential thermal conductivity.

5) To see the difference between λ_{11} (measured in the rod geometry) and λ''_{11} (measured in the Corbino geometry), which has been given by Eqs. (61a) and (61b), exactly the same boundary scattering is required in both geometries. This parameter which is actually hidden in these equations has a very important role in this investigation; and depending on the relative strength of this parameter in the two geometries, there is a possibility for obtaining $\lambda''_{11} > \lambda_{11}$ which is apparently in the opposite direction than what one expects from Eqs. (61a) and (61b).

6) The boundary scattering in the Corbino geometry is much smaller than in the rod geometry. In the experiments in the disk sample with the radius 6 mm and thickness about 3 mm, the boundary scattering was about 1/4 of the boundary scattering in the rod sample with dimensions 2.68 x 2.75 x 12 mm.

CHAPTER IV

PHONON FAN EFFECT

A - Introduction

A comprehensive study of the behavior of both carrier and phonon subsystems at high magnetic field under strong drag effect was presented in Chapter I. It was shown that under such conditions both carriers not only drift with the same velocity, cE/H (Hall velocity), but they also drag the phonons with almost the same drift velocity, $(1-\bar{\gamma})$ cE/H. This effect would become more interesting in the Corbino geometry where the geometry allows the phonons to circulate around the symmetry axis. We refer to this circulation of the phonon as the phonon fan effect.

By treating the phonons as quasi particles, one can show how the requirement of a centripetal force for such a motion would yield in a radial temperature gradient in the sample.

B - Theory

Considering phonons as quasi particles, one can associate the "inertial mass density" (ϱ) with the phonons and be defined as

$$\varrho = \frac{P}{UV} \tag{80}$$

where U, V and P are the drift velocity, volume and total

momentum of the phonons, respectively. P is given by

$$P = \sum_{q} \hbar q \langle N(q) \rangle \tag{81}$$

where q and N(q) are the phonon wave vector and distribution function, respectively. With $2\pi rtdr$ as an element of volume (t is the thickness of the disk and r is the radius of the element), the inertial mass associated with this volume is

$$dm = 2\pi rt \varrho \, dr. \tag{82}$$

The centripetal force acting on this element is given by

$$dF = \frac{\partial \mathcal{P}}{\partial r} (2\pi rtdr) \equiv (2\pi rt \varrho \, dr) \frac{U^2}{r} \tag{83}$$

or

$$\frac{\partial \mathcal{P}}{\partial T} \times \frac{dT}{dr} = \varrho \frac{U^2}{r} \tag{84}$$

where $\mathcal{P}$ is the phonon pressure and can be written as[38]

$$\mathcal{P} = \frac{kT}{V} \ln Z = \frac{4\pi^5 k^4}{45 h^3} \frac{T^4}{s_g^5} \tag{85}$$

for $U << s_g$, where Z and s_g are the grand partition function and velocity of sound, respectively. Using Eq. (81), one obtains

$$P = V \frac{16\pi^5}{45h^3} (kT)^4 \frac{U}{s_g^5}. \tag{86}$$

By substituting Eqs. (80), (85) and (86) in Eq. (84), one obtains

$$\frac{dT}{T} = \left(\frac{U}{s_g}\right)^2 \frac{dr}{r} . \tag{87}$$

At high magnetic field and under strong drag condition, phonon drift velocity is given by

$$U = (1- \bar{\gamma}) \frac{cE}{H} . \tag{88}$$

In Corbino geometry the electric field can be written as

$$E = \frac{\rho}{2\pi rt} I. \tag{89}$$

Therefore,

$$U = \frac{(1-\bar{\gamma})c}{2\pi t} \rho I(\frac{1}{r}). \tag{90}$$

By substituting Eq. (90) in (87), one obtains

$$\frac{dT}{T} = \frac{(1-\gamma)^2 c^2 \rho^2 I^2}{s_g^2 (2\pi t)^2} (\frac{1}{r})^2 \frac{dr}{r} \tag{91}$$

or

$$\frac{\Delta T}{T} \simeq \frac{1}{2}(\frac{U_1^2 - U_2^2}{s_g^2}) \simeq \frac{1}{2} \frac{U_1^2}{s_g^2} \tag{92}$$

where U_1 and U_2 are the drift velocities at points r_1 and r_2.

C - Results and Discussions

Equation (92) shows that the radial temperature gradient depends on $(\frac{U}{s_g})^2$. The fact that $U << s_g$ makes the experimental investigation of the effect difficult and in some cases even impossible. To estimate the magnitude of the effect, the temperature gradient in the sample under investigation is calculated. For example, at H = 20 KG and T = 2°K, magnetoresistance of the sample is about

$\rho \simeq 10^{-4}$ Ω-meter. Considering r_1 = 2 mm and t = 3 mm, one obtains

$$U_1(\text{meter/sec}) = 0.6\ I(\text{amp}).$$

In antimony where $s_g = 2.5 \times 10^3$ meter/sec, one can show that an electric current of several amperes would yield a temperature change smaller than one milikelvin.

In bismuth the situation is somehow different. In this semimetal one can easily achieve the condition where the drift velocity of the carriers becomes comparable and even equal to the sound velocity. (This effect, "kink effect", has been investigated by Esaki[39] in the study of current dependence of magnetoresistance in bismuth, where a sudden increase for certain amount of current was observed.) However, because of the small number of carriers in bismuth, phonon drag is very small, and consequently the phonon fan effect is expected to be negligible.

In addition to the problem mentioned, the quadratic dependence of the self heating of the sample on electric current, which is exactly similar to the phonon fan effect, makes this investigation more difficult.

To complete the discussion, experimental investigation of the effect was performed on sample No. 3 at two temperatures, T = 2.06°K and T = 1.58°K. Experimental results are shown in Fig. 25. The temperature difference, ΔT, in the sample due to the self heating can be calculated from Eq. (20B). Since in this experiment the potential probes

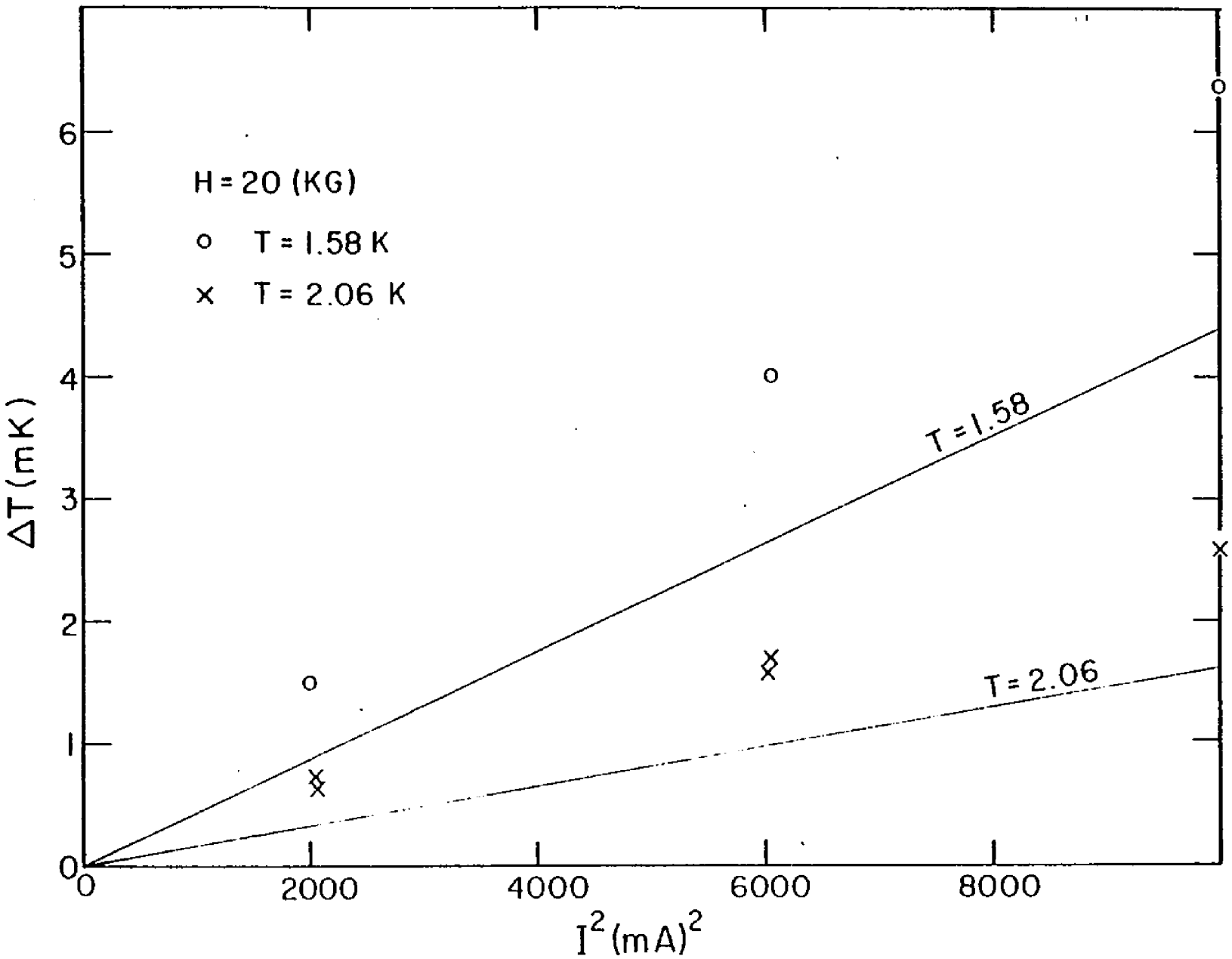
H = 20 (KG)
o T = 1.58 K
× T = 2.06 K
T = 1.58
T = 2.06
ΔT (mK)
I² (mA)²
0
1
2
3
4
5
6
0
2000
4000
6000
8000

Fig. 25

for magnetoresistance measurement and thermometers for thermal conductivity measurement were soldered exactly at the same point to the sample, the geometric factors for both measurements are the same. Thus, Eq. (20B) can be written as

$$\Delta T = \frac{RI^2}{2\Lambda} \frac{\ell n(r_o^2/ab)}{\ell n(b/a)} \tag{93}$$

wher R and Λ are the magnetoresistance and the thermal conduction of the sample, respectively, and are given as

$$R = \rho \frac{\ell n(b/a)}{2\pi t} \quad \text{and} \quad \Lambda = \lambda \frac{2\pi t}{\ell n(b/a)} \ . \tag{94}$$

For $r_o = b$, Eq. (93) becomes

$$\Delta T = \frac{RI^2}{2\Lambda} \ . \tag{95}$$

The ratio $\frac{\ell n(b/a)}{2\pi t}$ can be measured directly or can be determined by matching the thermal conductivity in the rod sample and the disk. Using the average values of a and b, we obtained a value of 1.33 for the ratio $\ell n(ab/r_o^2)/\ell n(b/a)$. The experiment was performed at H = 20 KG. At T = 1.58, R = 11.62 mΩ and Λ = 0.0175 w/°K, and at T = 2.06°K, there is no significant change in R, but Λ = 0.0467 w/°K. By substituting these values in Eq. (93), we obtain

$$\Delta T(m°K) = 4.4 \times 10^{-4} \ I^2(mA)^2 \text{ at } T = 1.57°K \tag{96}$$

$$\Delta T(m°K) = 1.6 \times 10^{-4} \ I^2(mA)^2 \text{ at } T = 2.06°K. \tag{97}$$

Equations (96) and (97) are shown on the same graph in Fig. 25 . The large difference between the experimental result and theoretical calculation may be caused by the

contact resistance between the current leads and the sample. The contribution of the phonon fan effect, noted previously, for electric current in the order of milliamperes is very small and should not be seen in this experiment.

It is interesting to note that for electric current smaller than 40 mA, the temperature change in the sample is smaller than one millikelvin which is the same order of magnitude as the uncertainty in the temperature measurements.

REFERENCES

1. C. L. Tsai, D. Waldorf, K. Tanaka and C. G. Grenier, Phys. Rev. B 15, 4968 (1977).
2. C. L. Tsai, D. Waldorf, K. Tanaka and C. G. Grenier, Phys. Rev. 17, 618 (1978).
3. C. L. Tsai, D. Waldorf, K. Tanaka and C. G. Grenier, Phys. Rev. 19, 2950 (1979).
4. J. P. Jan, Solid State Physics, ed. F. Seitz and D. Turnbull (Academic Press, New York 1957), Vol. 5, p. 4. See also C. G. Grenier, J. M. Reynolds, and J. R. Sybert, Phys. Rev. 132, 58 (1963).
5. A limited reference list is given, for example, in R. P. Huebener, Solid State Phys. Vol. 27, ed. F. Seitz and D. Turnbull, Academic Press, New York (1972) for drag effect references pertaining to thermoelectricity, and a limited list is given, for example, in Tsai's (refs. 2 and 3) in reference to mutual drag in the electrical conductivity and galvanomagnetic effects.
6. L. E. Gurevitch and I. Y. Koremblit, Sov. Phys. Solid State 9, 932 (1967)
7. For full drag $A^{\pm} = \frac{\ell^{\pm}}{\ell_r^{\pm}} - B^{\pm}$ and $B^{\pm} = -\Gamma^{\mp} \frac{\ell^{\pm}}{\ell_f^{\pm}} \frac{\mathcal{J}_5(\theta_1^*/T)}{\mathcal{J}_5(\theta_{\pm}^*/T)}$;

$$\frac{\rho}{\Delta(0)} = \rho_r \frac{\ell_r^+ \ell_r^-}{\ell^+ \ell^-};\ V_F^{\pm} = E \frac{\rho_r}{\rho} \frac{\ell_r^+ \ell_r^-}{\ell^+ \ell^-} \Big\{ \mu^{\pm} \Big(\frac{\ell^{\mp}}{\ell_r^{\mp}} + \Gamma^{\pm} \frac{\ell^{\mp}}{\ell_f^{\mp}} \frac{\mathcal{J}_5(\theta_1^*/T)}{\mathcal{J}_5(\theta_{\mp}^*/T)} \Big) +$$

$$+ \mu^{\mp} \Gamma^{\mp} \frac{\ell^{\pm}}{\ell_f^{\pm}} \frac{\mathcal{J}_5(\theta_1^*/T)}{\mathcal{J}_5(\theta_{\pm}^*/T)} \Big\};\ \text{also } V_F^{\pm} = E \frac{\rho_r}{\rho} \Big\{ \mu_r^{\pm} \Big(1 + \frac{\ell_r^{\mp}}{\ell_f^{\mp}} \Gamma^{\pm} x$$

$$\times \frac{\mathcal{J}_5(\theta_1^*/T)}{\mathcal{J}_5(\theta_{\mp}^*/T)}) + \mu_r^{\mp} \frac{\ell_r^{\pm}}{\ell_f^{\pm}} \Gamma^{\mp} \frac{\mathcal{J}_5(\theta_1^*/T)}{\mathcal{J}_5(\theta_{\pm}^*/T)} \Big\} .$$

8. The leading term in the quantity

$$\left.\frac{\partial v^+}{\partial \varepsilon}\right|_{\zeta+} + \left.\frac{\partial v^-}{\partial \varepsilon}\right|_{\zeta-} \simeq - \frac{eE}{3n\pi^2\hbar^3} (\nu^+ m_+^* \ell^+ - \nu^- m_-^* \ell^-)$$

contribute a term in ε is about 2×10^{-3} T(μv/°K). This quantity is negligible compared to the experimental data for ε_{11}.

9. See for example: C. G. Grenier, J. M. Reynolds, and J. R. Sybert of ref. 4.

10. Expression (27) can readily be obtained when the expression of the mean free paths $p_f^{\pm}$ and $L^{\pm}$ (Eqs. (9) and (10) of Tsai III) are taken into consideration, as well as the effect of anisotropy (see ref. 9).

11. In the experimental data fitting, parameter's values have been taken from different sources. From Tsai III we have $\rho_{id}/\rho_r = 4.04 \times 10^{-4}\ T^5 \mathcal{J}_5(\frac{14.2}{T})$. From Blewer, et al. (ref. 22), we have $n = 5.45 \times 10^{19}$ cm^{-3}, $Z^+ = 0.45 \times 10^{33}$ erg^{-1}cm^{-3}, $Z^- = 0.58 \times 10^{33}$ erg^{-1}cm^{-3}. $R = \frac{1}{4.2} = 0.24$ and from ref. 15 of Tsai III, $a^+ = 1.5$ and $a^- = 2.4$ and $N = 3.28 \times 10^{22}$ atoms/cm^3.

12. Yu. A. Bogod and V. B. Krasovitskii, Zh. Eksp, Teor. Fiz. 63, 1036 (1972) [Sov. Phys. - JETP 36, 544 (1973)].

13. M. S. Bresler and N. A. Red'ko, Zh. Eksp. Teor, Fiz. 61, 287 (1971) [Sov. Phys. - JETP 34, 149 (1972)].

14. Yu. A. Bogod, B. I. Verkin, and V. B. Krasovitskii, Zh. Eksp. Teor. Fiz. 61, 275 (1971) [Sov. Phys.-JETP 34, 142 (1972)].

15. V. Ya. Kravchenko and E. I. Rashba, Zh. Eksp. Teor. Fiz. 56, 1713 (1969) [Sov. Phys.-JETP 29, 918 (1969)].

16. B. N. Aleksandrov, V. V. Dukin, L. A. Maslova and S. V. Tsivinskii, Zh. Eksp. Teor. Fiz. 61, 243 (1971) [Sov. Phys.-JETP 34, 125 (1972)].

17. T. Hattori, J. Phys. Soc. Jpn 23, 19 (1967).

18. See, for example, Herbert B. Callen [Phys. Rev. 73, 1349 (1948); ibid. 85, 16 (1952).

19. R. A. Herrod, C. A. Gage, and R. G. Goodrich, Phys. Rev. B 4, 1033 (1971).

20. G. K. White and S. B. Woods, Phil. Mag. 3, 342 (1958).

21. J. R. Long, C. G. Grenier and J. M. Reynolds, Phys. Rev. 140, A187 (1965); Phys. Letters 16, 214 (1965).

22. R. S. Blewer, N. H. Zebouni and C. G. Grenier, Phys. Rev. 174, 700 (1968).

23. Joseph Callaway, Phys. Rev. 113, 1046 (1959); 122, 787 (1961).

24. J. M. Ziman, Electrons and Phonons (Oxford University Press, London, 1960), pp. 319-322.

25. R. E. B. Makinson, Proc. Cambridge Phil. Soc. 34, 474 (1938).

26. H. B. G. Casimir, Physica 5, 495 (1938).

27. Peter Carruthers; Rev. Mod. Phys. 33, 92 (1961).

28. P. G. Klemens, Proc. Phys. Soc. (London) A68, 1113 (1955).

29. Conyers Herring, Phys. Rev. 95, 954 (1954).

30. P. G. Klemens, in Solid State Physics, edited by F. Seitz and D. Turnbull (Academic Press, Inc., New York,

1958), Vol. 7, p. 87.

31. Philip D. Thacher, Phys. Rev. 156, 975 (1967).

32. A. Summerfeld and H. Bethe, in Hanbuch der Physik edited by H Geiger and K. Scheel (Julius Springer, Berlin, 1933), Vol. 24/2, p. 333.

33. Under isotropic- and quadratic-energy distribution, the Fermi pockets of holes and electrons are spheres of radius k_e and k_h given by $k_e = (3\pi^2 \frac{2}{3} n)^{1/3}$ and $k_h = (3\pi^2 \frac{2}{6} n)^{1/3}$. The isotropic effective mass is given by $m_e = \hbar^2 k_e^2 / 2\zeta_e$, the density of states by $Z_e = 3n/2\zeta_e$, the scattering effective Debye temperature by $\theta_e = \hbar s_g 2k_e/K$, and similar expressions for the holes. In agreement with Windmiller and Brandt, et al., the number of carriers per band is taken equal to $n = 5.45 \times 10^{19}$ cm^{-3}. The chemical potential under the assumption of a parabolic distribution is taken as $\zeta_e = 14.1 \times 10^{-14}$ erg and $\zeta_h = 18.2 \times 10^{-14}$ erg. With these values and with $s_g = 2.5 \times 10^5$ cm/sec, the different electronic parameters are $k_h = 6.4 \times 10^6$ cm^{-1}, $k_e = 8.1 \times 10^6$ cm^{-1}; $m_h \simeq 0.13\ m_o$, $m_e \simeq 0.28\ m_o$; $\theta_h^* \simeq 24.4°K$, $\theta_e^* \simeq 30.8°K$, $Z_h = 0.45 \times 10^{33}$ erg^{-1} cm^{-3}, $Z_e = 0.58 \times 10^{33}$ erg^{-1} cm^{-3}.

34. L. R. Windmiller, Phys. Rev. 149, 472 (1966).

35. N. B. Brandt, N. Ya. Minina, and Chu Chen-Kang, Zh. Eksperim. i Teor. Fiz. 51, 108 (1966) [English transl.: Sov. Phys.-JETP 24, 73 (1967)].

36. G. N. Rao, N. H. Zebouni, C. G. Grenier, and J. M. Reynolds, Phys. Rev. 133, A141 (1964).

37. R. Berman, F. E. Simon, and J. M. Ziman, Proc. Roy. Soc. (London) A220, 171 (1953).

38. For example, see R. K. Pathria, Statistical Mechanics Pergamon Press (1972).

39. L. Esaki, Phys. Rev. Letters 8, 4 (1962).

APPENDIX A

THERMAL CONDUCTIVITY MEASUREMENTS

Four different methods are employed to measure temperature gradient in both geometries. They are designated as direct method, potentiometric method, bridge method, and so called plotting method.

i) "Direct method", which follows the definition of thermal conductivity: Temperature gradient across the sample is measured directly by resistance measurement of both the thermometers. This method may be less reliable because it involves the uncertainty of the two calibrations.

ii) Potentiometric method: After passing heat current, $\dot{Q}$, through the sample and measuring resistance of both the thermometers, $R_1(T_1)$, $R_2(T_2)$, the main heater is turned off. Then, the auxiliary heater is turned on and adjusted such that $R_1(T_1)$ is reproduced, $(R_1\langle T_1\rangle)$, and $R_2\langle T_1\rangle$ is measured. Note: Since the resistance of the whole circuit is much larger than the resistance of the thermometers in the above process, the electric current remains constant, and the electric potential of the thermometers is actually reproduced. From $R_2(T_2)$ and $R_2(\langle T_1\rangle)$ measurements, and using calibration curve of the second thermometer, R_2, the temperature difference across the sample is determined: (See Fig. A1)

$$\Delta T = T_2 - \langle T_1\rangle \ .$$

This method has one advantage over (i) in that only one calibration curve $R_2(T)$ is used. In general, $T_1 \neq \langle T_1\rangle$,

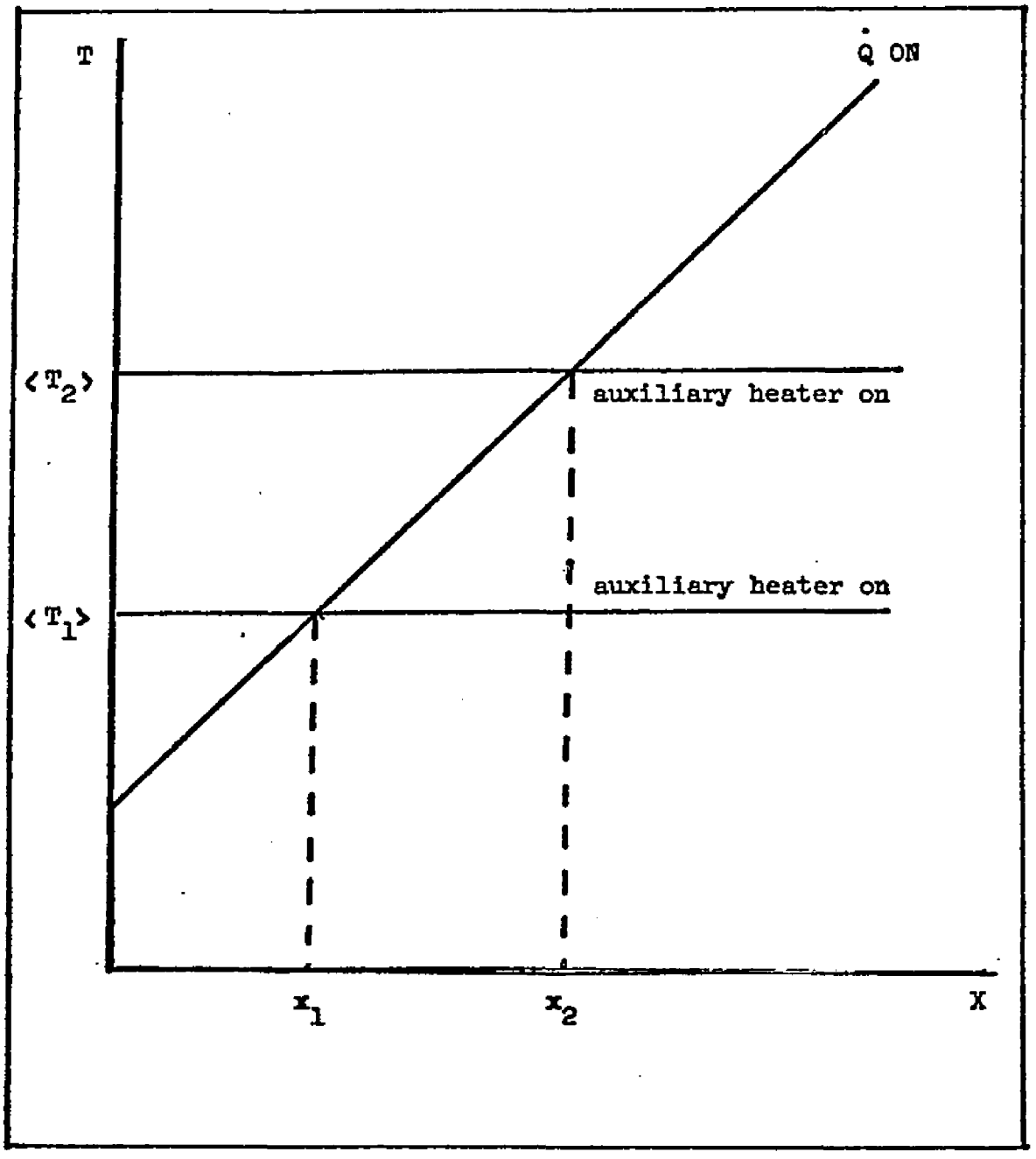
T
$\dot{Q}$ ON
$\langle T_2 \rangle$
auxiliary heater on
auxiliary heater on
$\langle T_1 \rangle$
x_1
x_2
X

Fig. A1

the difference between them is usually not more than a few tenths of a m°k and the correction to the value of ΔT is made with $R_1(T)$ calibration curve. The same procedure is employed for ΔT measurement from the calibration curve of the first thermometer. The average of these two values is used for determining the thermal conductivity. The difference of (ΔT) from these determinations is less than 0.1 m°K, which is less than 0.5% of the temperature difference, ΔT.

iii) Bridge method: In this method thermometers, R_1 and R_2, and adjustable resistors, R_1' and R_2', are the four elements of a Wheatstone bridge, Fig. A2 . One of the adjustable resistors, R_1', is adjusted such that by turning the auxiliary heater on and off, no change in the voltage across the bridge is detected. This means that the bridge is not sensitive in raising and lowering the temperature of the whole sample. (The auxiliary heater is adjusted such that the temperature of the sample raises to $\bar{T} \simeq (T_1 + T_2)/2$, where T_1 and T_2 are temperatures measured by the thermometers, R_1 and R_2, respectively, when the main heater is on.) After turning the auxiliary heater off, the main heater is turned on and the change in the voltage across the bridge is measured. For empirical purposes where the second order terms are negligible, it can be shown that

$$\delta(V_2-V_1) \simeq A*\delta(T_2-T_1) + B*\delta\langle T\rangle \qquad (1A)$$

where $\delta(V_2 - V_1)$ is the variation of $V_2 - V_1$ with respect

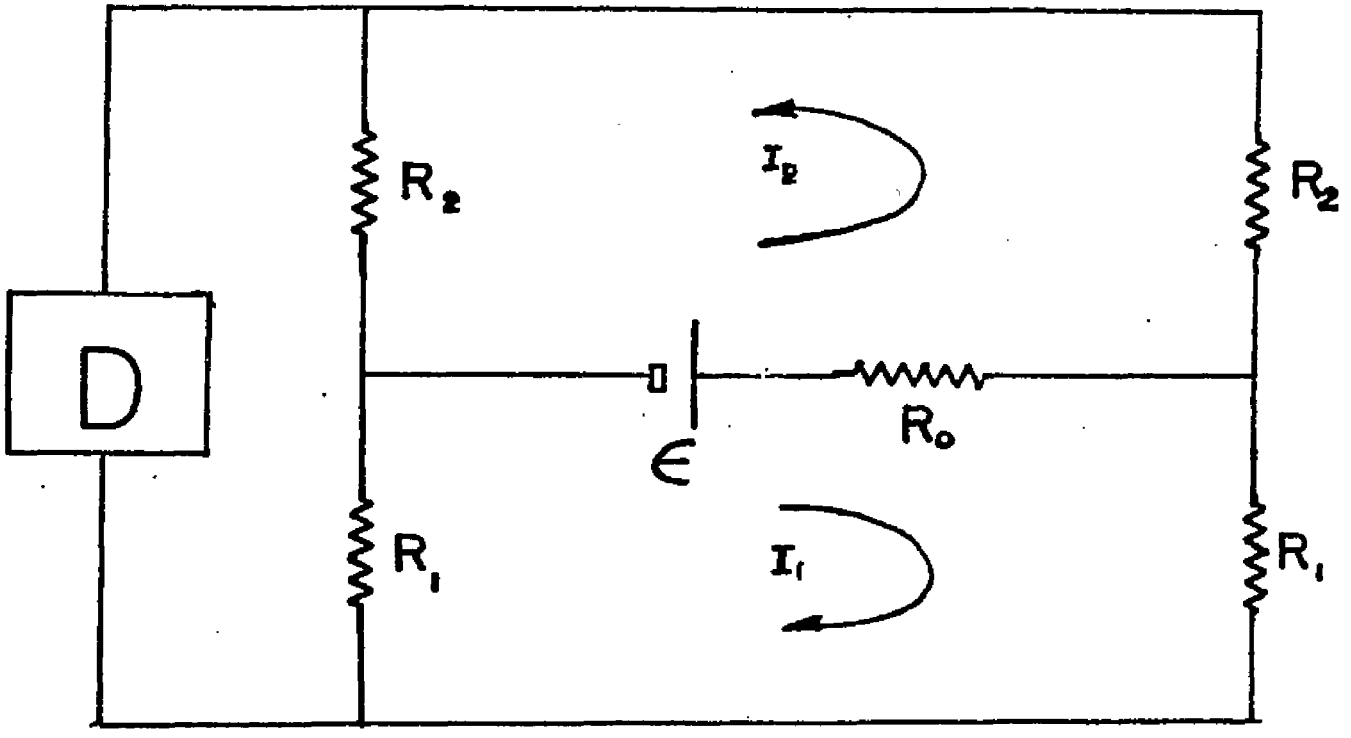

Fig. A2

to temperature variation, $\delta(T_2 - T_1)$, across the sample, and

$$\delta\langle T\rangle = \frac{\delta T_1 + \delta T_2}{2} \tag{2A}$$

where δT_1 and δT_2 are the temperature change of the thermometers 1 and 2 when the main heater is on, with respect to $\bar{T}$ the temperature of the sample when the auxiliary heater is on. And

$$A^* = \frac{1}{2}\left[\lambda_2\left(\frac{\partial R_2}{\partial T}\right)_{\langle T_2\rangle} + \lambda\left(\frac{\partial R_1}{\partial T}\right)_{\langle T_1\rangle}\right] \tag{3A}$$

$$B^* = \frac{1}{2}\left[\lambda_2\left(\frac{\partial R_2}{\partial T}\right)_{\langle T_2\rangle} - \lambda\left(\frac{\partial R_1}{\partial T}\right)_{\langle T_1\rangle}\right] \tag{4A}$$

where

$$\lambda_1 = I_1\alpha_1 + \frac{V_2 - V_1}{R_1+R_1'+R_2+R_2'} \qquad \alpha_1 = \frac{R_2'}{R_2'+R_2} \tag{5A}$$

and

$$\lambda_2 = I_2\alpha_2 - \frac{V_2 - V_1}{R_1+R_1'+R_2+R_2'} \qquad \alpha_2 = \frac{R_1'}{R_1'+R_1}\ . \tag{6A}$$

iv) Plotting method: This method is most useful for samples with high conductivities, such as samples with Corbino geometry, especially above λ point. In this situation, other methods are less reliable because ΔT is very small and the mean temperature $\langle T\rangle$ rises markedly above the bath temperature, T_o. In the first part, one has to adjust

the Wheatstone bridge such that the difference of the voltages across the bridge remains constant for a small step change of specimen temperature raised by the auxiliary heater. Then, after turning the auxiliary heater off, several small heat currents, $\delta\dot{Q}$, are applied to the sample and the changes of the bridge voltage noted. Since $B^*\delta \langle T \rangle \simeq 0$ in this case, Eq. (1A) can be written as

$$\delta(V_2-V_1) \simeq A^*\delta(T_2-T_1) \tag{7A}$$

or

$$\delta(V_2-V_1) \simeq A^* \frac{\dot{Q}}{\Lambda} \tag{8A}$$

where

$$\Lambda = \frac{\dot{Q}}{\delta(T_2-T_1)} \cdot \tag{9A}$$

Equations (8A) shows a linear relation between $\delta(V_2 - V_1)$ and Q. Now if we consider the second order terms, which were neglected before, we can show that

$$\delta(V_2-V_1) = a_1\dot{Q} + a_2\dot{Q}^2 \tag{10A}$$

where $a_1 = A^*/\Lambda$. Therefore, measurements of $\delta (V_2 - V_1)$ vs $\dot{Q}$ display a discernible deviation from linearity. The parameter, a_1, can be obtained from the data by means of a quadratic least square fit. This method involves temperature derivatives of both R_1 and R_2 and thereby the errors of both calibrations.

APPENDIX B

SOME ASPECTS OF CORBINO GEOMETRY

i) Geometric factor calculation: Considering an isotropic disk with constant resistivity, ρ, electric field E_r can be written as

$$E_r = \rho J_r. \tag{1B}$$

J_r, the current density at point r, is given by

$$J_r = \frac{I}{2\pi rt} \tag{2B}$$

where I is the current, and t is the thickness of the disk. Substituting Eq. (2B) in (1B), we obtain

$$E_r = \frac{\rho I}{2\pi t}\left(\frac{1}{r}\right). \tag{3B}$$

Potential difference between two points at distance r_1 and r_2 from the center is given by

$$V = IR = \int_{r_2}^{r_1} E_r dr = \frac{\rho I}{2\pi t}\int_{r_2}^{r_1}\frac{dr}{r} = \frac{\rho I}{2\pi t}\,\ell n\left(\frac{r_1}{r_2}\right) \tag{4B}$$

so

$$R = \frac{\rho}{2\pi t}\,\ell n\left(\frac{r_1}{r_2}\right). \tag{5B}$$

Therefore, the geometric factor, G, can be written as

$$G = \frac{2\pi t}{\ell n(r_1/r_2)}\ . \tag{6B}$$

A similar result can be derived for the thermal conductivity, λ, in terms of thermal conduction Λ

$$\Lambda = \lambda\,\frac{2\pi t}{\ell n(r_1/r_2)}. \tag{7B}$$

ii) Temperature gradient due to the self heating:

Thermal conductivity, λ, is defined as

$$-\lambda\vec{\nabla}\vec{T} = \vec{Q} \tag{8B}$$

or

$$-\lambda\nabla^2 T = \vec{\nabla}\cdot\vec{Q} \ . \tag{9B}$$

In the case of self heating one can write

$$\vec{\nabla}\cdot\vec{Q} = \vec{E}\cdot\vec{J} = E_r J_r \tag{10B}$$

where E_r, the electric field, and J_r, the current density, in the Corbino geometry have been given by

$$E_r(r) = \frac{\rho I}{(2\pi t)r} \qquad \text{and} \qquad J_r(r) = \frac{I}{(2\pi t)r}. \tag{11B}$$

Therefore,

$$E_r(r)\cdot J_r(r) = \frac{\rho I^2}{(2\pi t)^2}\cdot\frac{1}{r^2} = \frac{\beta\lambda}{r^2} \ , \tag{12B}$$

where

$$\beta = \frac{\rho I^2}{(2\pi t)^2\lambda} \tag{13B}$$

and ρ, I, and t are resistivity, electric current, and thickness of the sample, respectively.

By substituting Eq. (12B) in (9B) one obtains

$$-\nabla^2 T = \frac{\beta}{r^2} \tag{14B}$$

or

$$\frac{1}{r}\frac{\partial}{\partial r}\left[r\frac{\partial T}{\partial r}\right] + \frac{\beta}{r^2} = 0, \tag{15B}$$

hence

$$\frac{\partial T}{\partial r} + \frac{\beta}{r}\,\ell n(r) - \frac{c}{r} = 0 \tag{16B}$$

where c is the constant of integration. At $r = r_o$ (r_o the radius of the disk) $\left.\frac{\partial T}{\partial r}\right|_{r=r_o} = 0$, therefore,

$$\frac{\partial T}{\partial r} + \frac{\beta}{r} \ell n\left(\frac{r}{r_o}\right) = 0. \qquad (17B)$$

The temperature difference, $T_{(r=b)} - T_{(r=a)}$, can be obtained by integrating from Eq. (17B).

$$T_b - T_a = -\beta \int_a^b \frac{\ell n\left(\frac{r_o}{r}\right)}{r} dr. \qquad (18B)$$

The above integration can easily be performed, and it yields

$$T_b - T_a = -\frac{\beta}{2} \left\{ \left[\ell n\left(\frac{b}{r_o}\right)\right]^2 - \left[\ell n\left(\frac{a}{r_o}\right)\right] \right\}^2 \qquad (19B)$$

or

$$T_b - T_a = \frac{\rho I^2}{2(2\pi t)^2} \left\{ \left[\ell n\left(\frac{b}{r_o}\right)\right]^2 - \left[\ell n\left(\frac{a}{r_o}\right)\right] \right\}^2. \qquad (20B)$$

In the case that $b \approx r_o$, the above equation finds easier form,

$$T_b - T_a = \frac{\rho I^2}{2(2\pi t)^2 \lambda} \left[\ell n\left(\frac{b}{a}\right)\right]^2. \qquad (21B)$$

For I = 20 ma, t = 0.3 cm, b = 0.5 cm and a = 0.2 cm and at T = 1°K and H = 20 KG where $\rho \simeq 1.5 \times 10^{-2}$ Ω-cm and $\lambda = 0.0038$ ω/°K cm, $\Delta T \simeq 0.2$ m°K is obtained.

iii) Effect of damaged layer in magnetoresistance: The presence of surface layer conductance will alter the measured magnetoconductivity, $\langle\sigma\rangle$, from its bulk value, σ. By employing the damaged layer model, which was introduced in Chapter II, the relationship between the effective and bulk magnetoconductivity can be derived.

Considering a disk with thickness t and damaged layer δ in each side, one can write

$$J_r = \sigma_{rb} E_r \qquad (22B)$$

$$J_{rs} = \sigma_{rs} E_r \tag{23B}$$

where J_{rb} and J_{rs} are the radial current density in the bulk and surface layer, respectively. E_r is the electric field, $\sigma_{rb} = \sigma_{11b}$ and $\sigma_{rs} = \sigma_{11s}$ are the bulk and surface layer magnetoconductivity, respectively. The total current I can be written as

$$\begin{aligned} I = 2\pi rt \langle J_r \rangle &= 2I_s + I_b \\ &= 2(2\pi r)\delta J_{rs} + 2\pi r(t-2\delta)J_{rb}. \end{aligned} \tag{24E}$$

Therefore,

$$\langle J_r \rangle = J_{rb}(1 - \frac{2\delta}{t}) + \frac{2\delta}{t} J_{rs}, \tag{25B}$$

where $\langle J_r \rangle$ is effective current density and is defined

$$\langle J_r \rangle = \langle \sigma \rangle E_r. \tag{26B}$$

By substituting Eqs. (22B) and (23B) in Eq. (26B), one obtains

$$\frac{\langle \sigma \rangle}{\sigma_{11b}} = 1 - \frac{2\delta}{t} + \frac{2\delta}{t} \frac{\sigma_{11s}}{\sigma_{11b}} \tag{27B}$$

since $\frac{2\delta}{t} << 1$, therefore

$$\frac{\langle \sigma \rangle}{\sigma_{11b}} \simeq 1 + \frac{2\delta}{t} \frac{\sigma_{11s}}{\sigma_{11b}} . \tag{28B}$$

iv) Motion of a charge particle in a cylindrical electric field and uniform magnetic field: In an electric field $\vec{E}$ and magnetic field $\vec{H}$, force $\vec{F}$ exerted on a charge particle (e) moving with velocity $\vec{v}$ is given as (Loranz Force)

$$\vec{F} = e\vec{v} \times \vec{H} + e\vec{E}. \tag{29B}$$

In a Corbino geometry where the electric field can be written as

$$\vec{E} = \vec{E}_r = \frac{\lambda}{2\pi\varepsilon_o r}\,\vec{r} \tag{30B}$$

where λ is the charge density, ε_o the permittivity of free space and r the radial distance from the symmetry axis (z-axis) with uniform magnetic field along the z axis, exerted torque on the charge particle can be written as

$$\begin{aligned}\vec{\tau} &= \vec{r} \times \vec{F} = \vec{r} \times (e\vec{v} \times \vec{H}) \\ &= (\vec{r}\cdot\vec{H})e\vec{v} - (\vec{r}\cdot\vec{v})e\vec{H}\end{aligned} \tag{31B}$$

or

$$\tau_z = -r\dot{r}eH. \tag{32B}$$

Angular momentum (L) of the particle is defined as

$$\vec{L} = m\vec{r} \times \vec{v} \tag{33B}$$

where m is the mass of the particle. Now

$$\frac{\overrightarrow{dL}}{dt} = m\vec{v} \times \vec{v} + \overrightarrow{mr} \times \frac{\overrightarrow{dv}}{dt} = m\vec{r} \times \frac{\overrightarrow{dv}}{dt}\ . \tag{34B}$$

In cylindrical coordinate (r,θ,z), $\frac{\overrightarrow{dL}}{dt}$ can be written as

$$\frac{dL}{dt} = mr\dot{r}\dot{\theta} + mr\,\frac{dr\dot{\theta}}{dt} = m\,\frac{d(r^2\dot{\theta})}{dt}\ . \tag{35B}$$

By equating Eq. (24B) with (27B) one obtains

$$m\,\frac{d(r^2\dot{\theta}\ )}{dt} = -\ r\dot{r}eH \tag{36B}$$

or

$$\frac{d}{dt}\,(r^2\dot{\theta} + \frac{eH}{2m}\,r^2) = 0 \tag{37B}$$

or

$$r^2(\dot{\theta} + \frac{\omega_c}{2}) = \ell \tag{38B}$$

where $\omega_c = \frac{eH}{m}$ and ℓ is the constant of the integration and

can be written as $\ell = r_o^2 \frac{\omega_c}{2}$. Therefore,

$$r^2\dot{\theta} = \frac{\omega_c}{2}(r_o^2 - r^2) \tag{39B}$$

or

$$\dot{\theta} = \frac{\omega_c}{2}\left(\frac{r_o^2}{r^2} - 1\right). \tag{40B}$$

The total energy of the particle (u) is given by

$$u = \frac{1}{2} mv^2 + eV, \tag{41B}$$

where V is the electric potential and can be written as

$$V = -\int \vec{E}\cdot\vec{dr} = -\int \frac{\lambda dr}{2\pi\varepsilon_o r} = -\frac{\lambda}{2\pi\varepsilon_o} \ell nr + \text{constant}. \tag{42B}$$

Therefore,

$$u' = u + \text{constant} = \frac{1}{2}mv^2 - \frac{e\lambda}{2\pi\varepsilon_o} \ell nr \tag{43B}$$

or

$$u' = \frac{1}{2}m(\dot{r}^2 + r^2\dot{\theta}^2) - \frac{e\lambda}{2\pi\varepsilon_o} \ell nr \tag{44B}$$

or

$$u_o = \dot{r}^2 + r^2\dot{\theta}^2 - \frac{e\lambda}{\pi m\varepsilon_o}\ell nr \tag{45B}$$

where $u_o = \frac{2u'}{m}$. By substituting Eq. (40B) in (45B) one obtains

$$\dot{r}^2 + r^2 \frac{\omega_c^2}{4}\left(\frac{r_o^2 - r^2}{r^2}\right)^2 - \frac{e\lambda}{\pi m\varepsilon_o} \ell n \frac{r}{r_o} = U \tag{46B}$$

where $U = u_o + \frac{e\lambda}{\pi m\varepsilon_o} \ell n\, r_o$. Considering $x = r - r_o << r_o$, Eq. (46B) can be written as

$$\dot{x}^2 + \omega_c^2 x^2 - \frac{e\lambda}{m\pi\varepsilon_o}\frac{x}{r_o} = U \tag{47B}$$

or

$$2\dot{x}\ddot{x} + 2\omega_c^2 x\dot{x} - \frac{e\lambda}{m\pi\varepsilon_o}\frac{\dot{x}}{r_o} = 0 \tag{48B}$$

or

$$\ddot{x} + \omega_c^2(x - x_o) = 0 \tag{49B}$$

where $x_o = \frac{e\lambda}{2\pi m\varepsilon_o \omega_c^2 r_o}$. The solution for Eq. (49B) is

$$x = a \sin \omega_c t + x_o, \tag{50B}$$

where a is a constant.

Equation (39B) can be written as

$$(r_o + x)^2 \dot{\theta} = \frac{\omega_c}{2}(2r_o + x)(-x) \tag{51B}$$

or

$$r_o^2 \dot{\theta} + 2r_o x(\dot{\theta} + \frac{\omega_c}{2}) + x^2(\dot{\theta} + \frac{\omega_c}{2}) = 0 \tag{52B}$$

or

$$\dot{\theta} = - \frac{\omega_c(2r_o + x)x}{2(r_o^2 + 2r_o x + x^2)} - \frac{\omega_c x}{r_o}. \tag{53B}$$

Substituting Eq. (50B) in (53B), one obtains

$$\dot{\theta} = - \frac{\omega_c}{r_o} a \sin \omega_c t + \Omega, \tag{54B}$$

where Ω is the precession frequency and can be written as

$$\Omega = - \frac{\omega_c x_o}{r_o} = - \frac{\omega_c}{r_o} \cdot \frac{e\lambda}{2m\pi\varepsilon_o \omega_o^2 r_o}$$

$$= -e \frac{\lambda}{2\pi\varepsilon_o r_o} \cdot \frac{1}{m\omega_c r_o} \tag{55B}$$

$$= - \frac{e}{m\omega_c} \frac{E_o}{r_o} = - \frac{E_o}{H} \frac{1}{r_o}.$$

Therefore,

$$\text{drift velocity} = \Omega r_o = - \frac{E_o}{H} \tag{56B}$$

which is exactly the same as one obtains in a uniform cross electric and magnetic field.

VITA

Mahmood Baratikhajooie was born April 1, 1946, in Esfahan, Iran, and was raised and educated in the elementary school in that area. In 1963, after his graduation from Harati High School in Esfahan, he passed the entrance examination and entered Tehran University. In May 1966 he received his Bachelor Degree in Physics. In the same year he started his graduate work at Shiraz University where he received his Master Degree in December 1969. In 1970, he married Miss Farkhondeh Nazem. In 1971, his first son, Faramarz, was born and recently his second son, Farzad. After working at Shiraz University for six years as an instructor, in January 1975 he enetered the Graduate School of Louisiana State University in Baton Rouge. He is presently a candidate for the degree of Doctor of Philosophy in the Department of Physics and Astronomy of Louisiana State University.

EXAMINATION AND THESIS REPORT

Candidate: Mahmood Baratikhajooie

Major Field: Experimental Solid State Physics

Title of Thesis: "Transport Properties of Antimony in a Rod and Corbino Geometries at Low Temperatures"

Approved:

Major Professor and Chairman

Dean of the Graduate School

EXAMINING COMMITTEE:

Date of Examination:

April 16, 1980